High Energy Heavy Ion-Induced Structural Modifications in Binary Oxides

by

Alexander B. Cusick

A dissertation submitted in partial fulfilment
of the requirements for the degree of
Doctor of Philosophy
(Materials Science and Engineering)
in the University of Michigan
2015

Doctoral Committee:

Professor Emeritus Rodney C. Ewing, Chair
Professor Alex Bielajew
Assistant Professor Maik K. Lang, University of Tennessee, Knoxville
Professor Steven M. Yalisove

Table of Contents

List of Tables

List of Figures

of ion fluences.

Abstract

The objective of this work was to determine the relation between materials properties and their effect on the structural response of binary oxides to high energy heavy ion irradiation. The Group 14 oxides offered an ideal system of study due to the gradual change in materials properties from SiO_2 to PbO_2, while their electronic configurations remain consistent; this series facilitated the association of specific materials properties with their effect on radiation response. SnO_2 and PbO_2 were investigated experimentally in order to complete the body of data for this system. For comparative purposes, Ta_2O_5 was investigated under the same conditions due to the contrast in physical and chemical characteristics it offers, as well as its unusually large and complicated unit cell. SnO_2, PbO_2, and Ta_2O_5 were irradiated by 2.2 GeV ^{197}Au ions (11.1 MeV/u) at room temperature. Samples were analyzed with synchrotron X-ray diffraction, Raman spectroscopy, transmission electron microscopy, small-angle X-ray scattering, and X-ray photoelectron spectroscopy.

Irradiation of SnO_2 led to the formation of a crystalline SnO phase with trace quantities of metallic Sn, indicating the loss of oxygen and cation reduction during irradiation. Irradiation of PbO_2 resulted in the formation of seven distinct structures with compositions of Pb_2O_3, Pb_3O_4, PbO, and Pb. Gradual cation reduction was measured. Irradiation of Ta_2O_5 induced amorphous ion tracks with core-shell morphologies. Oxygen loss was evidenced, increasing with fluence to an estimated final stoichiometry of $Ta_2O_{4.2}$.

Using the Group 14 oxide system, the following relations were made: (i) increased susceptibility to amorphization has been attributed to high enthalpy of formation, bandgap, electrical resistivity, and cation electronegativity (relative to those resistant to amorphization), as well as relatively low bond ionicity and bond lengths; (ii) increased susceptibility to oxygen

loss during irradiation has been attributed to relatively low bond dissociation energy, bandgap, and electrical resistivity, as well as relatively large bond lengths; (iii) increased susceptibility to cation reduction has been attributed to relatively high bond ionicity as well as low enthalpy of formation, melting temperature, resistivity, and cation electronegativity. Materials property value thresholds are presented for all properties that show correlations to each radiation effect.

Chapter 1

Introduction

1.1 Scientific Issues

The focus of this research is on the effects of high energy heavy ion irradiation on the binary oxides of Group 14 elements: Si, Ge, Sn and Pb. These metal oxides have the same electronic configurations, providing an opportunity to understand how other chemical, physical, and structural properties affect the response of these materials to high-energy electronic excitation. The Group 14 elements have $ns^2n\text{p}^2$ configurations, with n increasing from 3 to 6 from Si to Pb. They therefore exhibit both 4+ and 2+ oxidation states, and similar bonding behavior. These elements also span a wide range of physical and chemical properties, and exhibit nonmetallic, semimetallic, and metallic behavior. They exhibit a range of atomic radii, ionic/covalent bonding character, electronegativities, band gap, and crystal structures in elemental and oxide form. As high energy (swift) heavy ion effects on SiO_2 and GeO_2 have been well characterized, SnO_2 and PbO_2 were investigated experimentally in order to complete the body of data for this system. For comparative purposes, another binary oxide with very different characteristics was investigated under the same conditions. Ta_2O_5 offers an interesting contrast to the Group 14 oxides due to its unusually large and complicated unit cell, as well as tantalum's very different electronegativity, electronic configuration ($5d^36s^2$ with a charge state of 5+), and bond-type in oxide form. Irradiation conditions were identical for all three oxides.

The materials selected for this study have important industrial applications. SnO_2 is widely used as a transparent conducting oxide in solar cells and flat panel displays, a solid state gas sensor due to its high surface sensitivity, and is used as an oxidation catalyst in industry [1,2]. The major application of PbO_2 is in lead-acid batteries [3], but it is also a strong oxidizing agent and is utilized in the production of pyrotechnics, matches, and dyes [4]. Ta_2O_5 is used in

transistors [5,6], microwave communication devices [5], and as charge capacitors in dynamic RAM devices [7]. All of these materials have a rich polymorphism, and because their properties depend strongly on their structure, modifications by swift heavy ions are of high technological interest.

Though there has been much interest in investigating the radiation resistance of oxides for nuclear and space applications, nano-scale material modifications have been very useful in materials engineering and the nano-sciences. Swift heavy ions (SHIs) have provided unique methods of creating and modifying nanostructures in a controlled manner. SHIs have been used to improve critical current density in high-T superconductors, modify the magnetic anisotropy and exchange bias in magnetic materials, improve friction and wear behavior in ceramics, and increase the lifetime of hip joint implants [8]. Swift heavy ions have been used to produce nano-pillars on the surface of gas sensing materials to improve efficiency [9], increase the crystallinity of materials [10], and has applications in the field of nanofabrication [11]. If materials modifications are to be utilized in the future, it is necessary to have a fundamental understanding of the ion-matter interactions in these materials and the parameters that control structural modifications.

Swift heavy ions are highly ionized heavy atoms accelerated to energies of over 1 MeV/nucleon (often in the GeV range), with velocities often over 15% of the speed of light. As ions impact a solid, their energy is deposited into the material's electronic subsystem, causing intense electronic excitation through ionization as the ions slow. This energy deposition per unit length in the material, dE/dx (in keV/nm), is concentrated in a very small cylindrical volume along the ion's trajectory, resulting in an extremely high energy density. The subsequent transfer of electronic energy to the atomic lattice creates a cylindrical damage zone, an "ion track". Tracks are typically on the order of several nanometers in diameter and many microns in length; this geometry is unique to swift heavy ion techniques.

Materials subjected to swift heavy ion irradiation undergo complex structural modifications; the extent of which depends on the material, as well as the ion species and energy. The effects on radiation-resistant materials consist of defect production and clustering, grain growth, fragmentation, swelling, and polygonization [12,13]. In materials with a higher susceptibility to

damage accumulation, crystalline-to-crystalline phase transformations (often into high temperature or high pressure phases) [14–17], amorphization [15,18–23], chemical effects (cation reduction, anion loss) [24–28] are observed. Although there have been many models proposed to describe structural modifications by swift heavy ion irradiation, there is no general consensus on the exact mechanism of damage formation. There are also no rigorous relations between materials properties and radiation effects. This study was designed to directly address this lack of understanding, by aiming to associate specific materials properties with their effect on the material's response to highly ionizing radiation.

1.2 Energy Transfer Processes

As a high energy heavy ion impacts a solid, large quantities of energy are transferred to both valence and core electrons along the ion's trajectory (with dE/dx in the range of 10 to 50 keV/nm). These primary excited electrons rapidly transfer their energy to other electrons as they are radially ejected from the track core, creating an ionization cascade. Within a few femtoseconds, the secondary ionizations are complete and core holes are converted to valence holes through Auger transitions [29]. This electron-hole plasma is highly polarized, as holes in the track core are separated from the surrounding electrons (displaced up to a few hundred nm away from the track core [29]). This charge separation results in high electric fields, and is the basis for the "Coulomb explosion" model of damage production [30]. These fields are short-lived and depolarize as spatial charge neutrality is recovered, taking less than 1 femtosecond in Si [31] and less for metals. Though spatial neutralization is obtained, electrons remain in their excited states and quickly reach an equilibrium-like state of thermalization. The electrons reach a "temperature" that is very high as compared with the lattice, estimated to occur on the order of a few hundred femtoseconds [32]. Because of the change in interatomic interactions due to the highly excited electron distributions, the lattice may "relax" [29], initiating atomic displacements.

Energy is "stored" in the electronic subsystem during these processes, but is eventually transferred to the atomic lattice. The mechanism of electron-lattice interaction is not fully

understood, but likely leads to a simultaneous cooling of electrons and heating of the lattice. This interaction, which is a function of the material's specific heat and electron-phonon coupling strength, usually occurs on the order of a few picoseconds [29]. The mean free path of this interaction depends on the material and its structure, and ranges between about 3 and 12 nm [33]. Quenching through heat conduction may take up to 100 picoseconds and is intuitively a function of the material's thermal conductivity [29].

Many interpretations of the damage induced by these processes have been proposed, the differences being mainly in the relative emphasis of different energy transfer processes. For example, the "thermal-spike" model focuses on the lattice heating process (causing melting or vaporization within the track) and subsequent thermal quenching. The "Coulomb explosion" model focuses on the charge distribution after electrons are excited, leading to high electric fields which cause atomic displacement. The self-trapping exciton model focuses on the relaxation of excited electrons, forming excitons in high concentrations, which decay through defect formation. Finally, the "bond weakening" model focuses on the disruption of the interatomic bonds due to excitation of these electrons. These models will be discussed in more depth in the next section.

1.3 Damage Production Models

1.3.1 Thermal-spike Model

The thermal-spike model has been used successfully to describe many observed structural effects in materials, and focuses on the thermal transient occurring after electronic energy is transferred to the atomic lattice. This "thermal spike" is the process that is thought to be responsible for defect production and phase transitions. The model considers the solid as a two component system, with the atomic and electronic sublattices being separate entities. This model has been developed by Toulemonde et al. [34], and begins the description at the point at which the excited electrons are in the thermalized state. Energy is then transferred to the lattice through electron-phonon coupling. This large deposition of energy causes a sharp spike

4

in temperature, centered about the track core. This model can be described with two coupled partial differential equations representing the heat transfer between the two systems:

$$C_e \frac{\partial T_e}{\partial t} = \frac{1}{r}\frac{\partial}{\partial r}\left(rK_e(T_e)\frac{\partial T_e}{\partial r}\right) - \frac{K_e}{\lambda^2}(T_e - T_a) + A(r,t) \qquad \text{(eq. 1)}$$

$$C_a \frac{\partial T_a}{\partial t} = \frac{1}{r}\frac{\partial}{\partial r}\left(rK_a(T_a)\frac{\partial T_a}{\partial r}\right) + \frac{K_e}{\lambda^2}(T_e - T_a) \qquad \text{(eq. 2)}$$

Parameters *C*, *K*, and *T* are the specific heat, thermal conductivity, and temperature of each system (subscripts *e* and *a* designate electronic and atomic systems), respectively. The electron-phonon mean free path, λ, represents the average radius over which the electrons will spread before coupling to the lattice. *A* is the energy deposited to the electrons from the ion, as a function of radial distance from the ion trajectory and time. These coupled equations require a numerical solution. This model predicts that if the lattice temperature (T_a) exceeds the melting temperature, a first-order phase transition will occur. This leads to amorphization and other structural modifications within the ion track, as the lattice is quickly quenched before atoms have sufficient time to recrystallize [35]. There is also an analytical approach to this model, assuming the temperature profile perpendicular to the ion trajectory follows a Gaussian curve that spreads as function of time [36]. A key point of the thermal-spike model is that the threshold stopping power (below which effects are not seen) corresponds to melting or vaporization of material within the track core. For amorphization or other phase transitions to occur, the cooling rate must be sufficiently rapid in order to hinder recrystallization of the initial phase.

This model has been very successful in describing observed transformations, but there are limitations. The energy transfer processes are very complex and occur on very short timescales, and therefore occur under highly non-equilibrium conditions. The thermal-spike model relies on assumptions of thermodynamic equilibrium, using equilibrium critical values for melting and vaporization to determine melt-thresholds and track diameters, while assigning free parameters to fit experimental data [29,36,37]. Also, Arrhenius-type equations are used to account for defect production by ions with sub-threshold energies, assuming the equilibrium

5

generation of thermal defects [38]. The model is unable to account for material dependent effects, such as differences in track morphology [39] and variations in threshold stopping powers [29]. Thus, the thermal-spike model may require an extension of the theory in order to fully capture ion-solid interactions.

1.3.2 Coulomb Explosion Model

The major difference between the Coulomb explosion and thermal-spike model is in the way energy is transferred to the lattice. In the case of Coulomb explosion, as excited electrons move outward from the track core and leave a highly positively-charged core behind, intense electrostatic repulsion between the lattice ions leads to their displacement. This model is described in detail by Fleischer et al. [30], which will form the basis for further discussion. This proposed mechanism relies on the electronic charge neutralization time being sufficiently long, and can only occur if the electrostatic repulsion forces overcame the lattice bonding forces. The local electrostatic forces must therefore overcome the bond strengths. The local electrostatic "stress" between atoms with charge state n and a separation of a_0 can be found using the charge e and dielectric constant ε, by dividing the local electrostatic force by the unit area a_0^2:

$$\sigma_e = \frac{n^2 e^2}{\varepsilon a_0^4} \qquad \text{(eq. 3)}$$

Using the approximation that the interatomic bonding force, or theoretical mechanical tensile strength, is related to the material's Young's modulus (by $Y/10$), the condition for the electrostatic stress exceeding the mechanical strength can be expressed as:

$$n^2 > R \equiv \frac{Y \varepsilon a_0^4}{10 e^2} \qquad \text{(eq. 4)}$$

Here, R is defined as the stress ratio and is considered to be a measure of the relative sensitivity of the material to track formation [30]. This shows that tracks should form most

easily in materials of low mechanical strength, close interatomic spacing, and low dielectric constant.

A problem with this Coulomb explosion description is that the $1/r^2$ dependence of the force between charged particles does not seem to account for observed atomic displacements. Also, neutralization is much faster than lattice relaxation because plasmon frequencies are much higher than phonon frequencies [29]. Therefore, electrons return to their vacant orbitals much faster than lattice atoms can move, resulting in neutralization before the supposed explosion occurs. This may result in a transfer of lower quantities of energy due to the Coulombic forces within the track than predicted, yet may still be important.

1.3.3 Self-trapping Exciton Model

Accounting for the decay of self-trapped excitons as a means of damage production has offered an advance in understanding of some observed radiation effects [39–41], though it is only relevant to materials in which self-trapping occurs. Electron-hole pairs are attracted through the Coulombic force and in some cases may form a bound state. The resulting quasiparticle therefore has an energy value less than that of the unbound electron and hole. In some materials an exciton may become self-trapped, in which the atomic structure surrounding the exciton becomes slightly distorted. This "traps" the exciton within the structure, further stabilizing it energetically, and prohibits diffusion of the quasiparticle. Self-trapped excitons localize energy, cause lattice instability, and decay through the production of Frenkel pairs; these form the basis for structural modifications in this model [41]. The primary role of self-trapped excitons in this context is to localize electronic energy close to the track core. Self-trapping renders excitons immobile and therefore unable to decrease the energy density through outward diffusion. These trapped excitons decay through both radiative and non-radiative mechanisms; the non-radiative type may transfer energy to phonons which induce lattice heating (much like electron-phonon coupling), but may also decay through the direct formation of Frenkel pairs. Lattice order will not be maintained if the exciton density approaches one per unit cell [29]. At these densities, clusters of self-trapped excitons cause the

7

loss of lattice stability and the atomic displacements needed to form a new structure. Exciton self-trapping has also been associated with a change in cation charge state [29], an effect observed in some irradiated oxides which has not yet been explained. This model has been successful in describing the radiation effects seen in highly ionic materials [28,42]. Exciton decay kinetics have also been added to the thermal-spike model in order to account for the superlinear relationship between stopping power and damage production [38].

1.3.4 Bond Weakening Model

Electronic excitation affects bonding electrons and therefore the interatomic forces that exist within an irradiated solid. The altered forces may therefore contribute to the structural modifications observed in swift heavy ion tracks, and may describe the decomposition of chemical bonds observed in some materials. This is plausible as the electronic structure strongly affects the material's crystal structure [43]. Calculations have shown that for Si, Ge, and GeAs, the excitation and loss of valence electrons by 15% induces instability in the lattice within 100 femtoseconds [44]; time-resolved XRD measurements following femtosecond laser pulses have recently verified this. Also, the excitation from bond-valence orbitals to conduction bands leads very quickly to structural rearrangements in materials such as Bi [45].

1.3.5 Impact Mechanisms

Some transformations have shown an initially linear relationship between the quantity of the modified phase and the ion fluence, leading to a sub-linear increase at saturation. This suggests that each ion impact contributes independently to the transition and therefore follows a *single-impact mechanism* of transformation [18]. This is often seen in the amorphization of complex oxides, as cylindrical amorphous tracks have been observed after single ion impacts [21,23]. There is also a sigmoidal relationship in some transformations, beginning as a slow increase in the quantity of the transformed phase, becoming an exponential increase until finally slowing to saturation [20]. This indicates that for these transformations to occur,

multiple impacts are required. The initial impacts play the role of introducing damage into the material (such as point defects), where further ion impacts may induce structural transformation as the accumulated damage reaches a critical level. These transformations follow a *multi-impact mechanism*. Other impact models exist [18] but are less relevant to this study and will not be discussed.

1.3.6 Summary

The relevance of each proposed damage model has been to some extent supported by experimental data. None of the models can be considered a full description of all transformation processes occurring in different materials. All of the mechanisms proposed by each model are likely to play some role in ion-induced phase transitions; the question is, which mechanisms control the process in each material. The thermal transient, if it is not itself responsible for the phase transition, certainly facilitates the process by providing the energy necessary for atomic rearrangements. Trapped electronic energy will keep the energy density high, which is an important requirement for inducing phase transitions and may be significant for materials that otherwise dissipate electronic energy efficiently. The charge separation after electrons are ejected from the track core likely plays a role in materials with long charge equalization times. In addition, the weakening of chemical bonds must be considered, as bonding electrons are displaced and the electronic environment changes significantly during the ionization and relaxation processes.

1.4 Radiation Responses

Binary oxides show a wide range of effects in response to swift heavy ion irradiation. Radiation-resistant materials show the production of defects but no significant structural changes. Some materials transition to high temperature/high pressure phases, and others become amorphous. A few materials have also been shown to undergo chemical changes, such

as decomposition. This section will briefly review the swift heavy ion effects observed in binary oxides.

1.4.1 Defect Accumulation and Aggregation

Binary oxides resistant to swift heavy ion-induced phase transformations are still, to some extent, susceptible to damage, despite the fact that they retain their overall crystal structures. For example, the irradiation of ThO_2 to high fluences with 2.2 GeV Au ions has been shown to induce point defects through a single impact mechanism, leading to swelling of the unit cell but no significant modification to its structure [12]. In UO_2, defect clustering was shown as defect rich tracks became unobservable at high fluences due to the precipitation of loops [13]. The track size as a function of energy loss was well modeled by thermal-spike calculations in this case. In yttria-stabilized cubic ZrO_2, the formation of micro-grains with small misalignments has been observed (polygonization) [46], which was also attributed to a single impact mechanism [47]. In other materials, grain growth and fragmentation are observed during ion irradiation, while retaining the initial crystalline structure [48,49]. These materials (among others) exhibit efficient defect recovery processes which make them resistant to higher levels of modification.

1.4.1 Crystalline-to-Crystalline Transformations

Monoclinic-to-tetragonal phase transitions have occurred in ZrO_2 and HfO_2 under swift heavy ion irradiation [14]. Both of these materials exhibit the monoclinic phase at ambient conditions and the tetragonal phase in high-temperature conditions, the latter being reached at ~1100°C in ZrO_2 and ~1700°C in HfO_2 [35]. These oxides share many physical and chemical properties due to the similarities in their outer shell electron configurations and ionic radii. Because their lattice parameters are almost equivalent, they have practically the same atomic density, but very different densities (~5.68 g/cm^3 for ZrO_2 and ~9.68 g/cm^3 for HfO_2) due to the grossly different atomic masses [35]. While these phase transformation readily occur in ZrO_2 (> 14 keV/nm) and HfO_2 (> 22 keV/nm), low energy ions within the nuclear stopping regime induce

the transformation only in ZrO_2 [50]. The transformation in both energy regimes are suspected to be driven by the oxygen vacancy concentration after reaching a critical value. The vacancy concentrations are comparatively lower in HfO_2 due to its higher O diffusivity [50]; reaching the critical O vacancy concentration is easily achieved in ZrO_2 with low energy irradiation, and is not in HfO_2, until sufficient energy is deposited to overcome the high diffusivity [50].

Swift heavy ions have been shown to induce a cubic-to-monoclinic phase transformation in Y_2O_3 powders [16], where the monoclinic form is a high pressure phase. A grain size effect was shown, in which the phase transition in nanograins was more efficient than larger-grained and sintered powders [51]. Track size was shown to increase with the energy deposition and was larger for the small grained samples, possibly attributed to the confinement of temperature and pressure within the small particles. Similarly, low-energy ion irradiations (300 keV Kr ions) at cryogenic temperatures have been shown to induce cubic-to-monoclinic transformations in Dy_2O_3 and Er_2O_3 [52]. A subsequent partial transformation from the monoclinic to hexagonal phase was reported for Dy_2O_3 at high fluences [53]. Both monoclinic and hexagonal phases are high temperature and/or pressure phases in Dy_2O_3. In addition, 200 MeV Au ions have been shown to transform TiO_2 thin films from the anatase to rutile phase (both tetragonal) [54]. This was explained by the thermal spike model, as the temperature spike led to the nucleation of the rutile phase well inside the anatase grains instead of at the grain boundaries alone, allowing full conversion.

1.4.3 Amorphization

Amorphization is commonly observed in the irradiation of complex oxides [21,23], but is also induced in materials such as SiO_2, ZrO_2, and Al_2O_3. Single crystal α-SiO_2 (quartz) was shown to amorphize under irradiation with Ni, Kr, and Pb ions with energies of several MeV/amu [55]. Amorphous regions were determined to be approximately 4% denser than the relaxed SiO_2 phase. The morphology of amorphous material was considered to be the same as samples amorphized through neutron and low energy ion irradiation, leading to the proposal that the amorphization mechanism is the same in all cases [55]. That is, they all occur through the

structural relaxation of a highly defective matrix after exceeding a critical O vacancy concentration. Amorphous cylindrical ion tracks have also been seen in irradiated quartz with a threshold of around 7 keV/nm [56]. ZrO_2 was considered to be non-amorphizable until nano-grained samples were irradiated [57]. High energy ions (1.33 GeV U and 1.69 GeV Au, with 52 keV/nm and 40 keV/nm, respectively) both induced amorphization in a 400 nm thick film with average grain sizes of 40-50 nm. This was attributed to the increased surface energy associated with the small grain size, as well as the associated decrease in thermal conductivity with confined phonon modes. Although computational thermal-spike model analysis suggested that the thermal spike could lead to melting inside the track, the amorphization process was still attributed to track overlap at high fluences, suggesting a multi-impact mechanism. Similar results have been shown in Al_2O_3, as tracks were observed after C-60 cluster irradiation (0.01 and 0.04 MeV/u) [58], 85 MeV I ions [59], and 92 MeV Xe ions [60]. In this case, the amorphization process was suggested to occur through a multi-impact mechanism, as partially disordered tracks must overlap.

1.4.4 Chemical Modifications

Evidence of preferential disorder on the O sublattice, O ejection from track cores, cation reduction, and/or metallic inclusion formation has been observed in a variety of binary oxides. Some or all of the aforementioned effects have been observed in GeO_2 [26], CeO_2 [27,61–63], Al_2O_3 [64], yttria-stabilized ZrO_2 [65], UO_3 [63], SiO [66], and InO [67]. Irradiation of CeO_2 was shown to cause the reduction of Ce^{4+} to Ce^{3+} [61–63] and O-deficient track cores surrounded by O-rich regions [27]. A decrease in O coordination number suggested the presence of a large number of O vacancies [61,62]. Preferential disorder on the O sublattice has been seen in the irradiation of Al_2O_3 [64], and reduction of Zr^{4+} to Zr^{3+} has been observed in irradiated yttria-stabilized ZrO_2 [65]. In addition, irradiations of substoichiometric oxides have shown similar results. SiO has phase separated during irradiation, forming of Si and SiO_2 nanocrystals [68], and irradiation of InO has led to In nanocrystal formation along the track core, surrounded by In_2O_3 [67]. Related radiation effects are seen in the alkali-halides, as reduced cation clusters

were found to form within track cores in LiF [24], CaF$_2$ [28], also resulting in mobile F atoms that were likely ejected from the core.

Preferential oxygen loss and cation reduction has also been measured in lower energy ion irradiations. For example, nano-grained cubic ZrO$_2$ irradiated by 2 MeV Au ions revealed significant O loss with increasing dose, with the O/Zr ratio decreasing from approximately 2.0 to 1.65 at a dose of 35 dpa [49]. Irradiation of nano-scale TiO$_2$ with 1 MeV Kr ions has resulted in the preferential loss of oxygen [69]. Reduction has also been observed after 10 keV Ar irradiation, revealing that the concentration of Ti^{2+} species increased with fluence at the expense of the Ti^{4+} species [70]. Though these particular effects occurred after irradiation in the nuclear stopping regime, the mechanism of modification may be similar in the electronic stopping regime.

1.4.5 Group 14 oxides

SiO$_2$ and SnO$_2$ have been extensively studied with highly ionizing radiation. Previous studies on GeO$_2$ are also available but limited. Irradiation of SiO$_2$ (quartz) by SHIs resulted in the formation of continuous amorphous tracks along the ion trajectories [55,56], which were shown to have a core-shell morphology [71]. The shell (surrounding the amorphous core) was higher in density by approximately 2% as determined by small angle X-ray scattering (SAXS). The morphology of amorphous material was considered to be the same as samples amorphized through neutron and low energy ion irradiation [55]. This suggested that the amorphization mechanism involves a critical O vacancy concentration, above which the structure will relax and lose crystallinity [55]. Femtosecond laser irradiation (purely electronic in excitation) has also been shown to cause amorphization in quartz [72]. Irradiation of hexagonal GeO$_2$ resulted in the removal of O atoms from the irradiated region and the reduction of Ge^{4+} to Ge^0. Ge nanocrystals formed and were surrounded by O-rich GeO$_2$ [26]. The authors reported no other structural effects, but based on their GIXRD data, the material also amorphized (at least on the surface). The formation of Ge nanocrystals was also evidenced in GeO$_2$ glass subjected to an electron beam during TEM [73]. These authors also observed a loss of oxygen by measuring a

drop in the O K edge using electron energy loss spectroscopy (EELS). This decomposition process in GeO_2 glass was also induced by femtosecond laser pulses above 0.4 µJ [74]. Low energy ions (1.5 MeV Xe ions with approximately equal nuclear and electronic dE/dx) were used to determine that quartz SiO_2 was the most susceptible to amorphization in these conditions, followed by hexagonal, and finally rutile-type GeO_2 [75]. The most notable previous work on SnO_2 has been on nanopowders. Ions with high stopping power were shown to form empty cylindrical holes within SnO_2 nanoparticles. Material was proposed to have vaporized and escaped the material, leaving only cylindrical holes [48,76–78]. Fragmentation of particles into smaller grains was also observed. SHI irradiations of SnO_2 thin films resulted in an enhancement of crystallinity at low fluence, but a decrease at high fluences [10]. Nano-pillar structures were created on irradiated surfaces, increasing gas sensing efficiency [9]. There have not been prior irradiation studies on PbO_2 or Ta_2O_5.

1.5 Research Strategy

The relation between materials properties and their structural response to swift heavy ion irradiation is not well characterized; the ultimate goal is to obtain a full description for the radiation response of all materials. The important factors in a material's response to irradiation are the properties that make it susceptible to electronic excitation, and the mechanisms it has to recover. The damage models discussed in Section 1.3 attempt to model the observed structural effects but have difficulty doing so, as the effects are, to a great extent, material-specific. For example, the thermal-spike model has been very successful in describing radiation effects in many materials, but is unable to account for differences in track morphology in different materials [41] as well as variations in threshold stopping powers [39]. It is therefore necessary to attribute specific materials properties to their effect on radiation response. The Group 14 oxides offer an ideal system to study due to the gradual change in materials properties from SiO_2 to PbO_2, while their electronic configurations stay consistent. The study of this series will therefore facilitate the association of specific materials properties with their effect on radiation response. Based on data in the literature, a material's sensitivity to

14

structural modifications (and the character of modification) may be related to some or all of the following properties:

- melting temperature
- heat capacity
- crystal structure/symmetry
- band gap
- electrical resistivity
- cation electronegativity
- cation valence variability
- bond character/ionicity
- ionic/covalent radii and bond lengths
- bond dissociation energy
- cohesive energy and enthalpy of formation
- the ability to self-trap excitons

The purpose of this study is to concentrate on phase transitions in the Group 14 oxide system as a means to further advance these relations. This series of materials ranges from primarily covalent to ionic bonding, highly stable to relatively weak cohesive energies, and highly electrically resistive to essentially conductive (see Table 1.1). Ta_2O_5 has properties that lie within the range of the Group 14 oxides (for example, bond dissociation energy) as well as outside of this range (for example, electronegativity). A systematic study of the Group 14 series, with the addition of Ta_2O_5, offers a sufficiently diverse system with enough consistency to yield conclusive results.

Table 1.1. Materials Properties of Group 14 Dioxides and Ta_2O_5

Property	Units	Ta2O5	SiO2	GeO2	SnO2	PbO2	
cation atomic mass	amu	181.0	28.1	72.6	118.7	207.2	
melting temperature (Tm)	K	2173	1999	1389	1902	563	[r]
heat capacity (Cp)	kJ/mol-K	135.1	69.8	82.6	52.6	73.4	[r]
electrical resistivity (ρ)	ohm-cm	10^8	$5x10^{18}$	10^{15}	$5x10^{-4}$	10^{-4} [c]	[L]
ionic radius (4+ state)	Å	0.68 [k]	0.40	0.53	0.69	0.78	[t]
covalent radius (4+ state)	Å	1.34 [k]	1.18	1.22	1.41	1.46	[t]
bond length	Å	1.99 [u]	1.61 [v]	1.88 [w]	2.05 [x]	2.16 [u]	
band gap (Eg)	eV	4.74 [e]	9.0 [a]	6.1 [a]	3.5 [d]	0.23 [b], 1.6 [c]	
cohesive energy	eV/atom	7.41 [p]	7.45 [m]	6.6 [n]	4.91 [g]	not available	
crystal dissociation E	eV/atom	5.03	6.12	6.22	4.01	3.35	[r]
ΔH: MO2 (4+ state)	eV/atom	4.23 (5+)	3.15	2.00	1.99	0.96 [q]	[k]
ΔH: MO (2+ state)	eV/atom	N/A	N/A	N/A	1.45	1.13	[k]
ΔH: MxOy (mixed state)	eV/atom	N/A	N/A	N/A	N/A	1.04, 1.09 [q]	
bond dissociation E	ev/atom	1.67	2.76	2.29	1.89	1.31	[i]
cation electronegativity	unitless	1.98	1.91	1.76	1.63	1.62	[s]
fractional ionicity (M-O)	unitless	0.413	0.443	0.506	0.559	0.563	[y]

References (shown to the right of each row unless otherwise noted): a [79], b [80], c [81], d [10], e [82], f [77], g [83], h [56], i [84], j [85], k [86], L [87], n [88], q [89], r [90], s [91], t [4], u [92], v [55], w [93], x [94], y [95]

To study the effects of high energy heavy ion irradiation on the structure of these materials, we have employed complimentary analytical techniques to characterize the initial structures and the structure of samples irradiated to varying levels of ion fluence. These techniques include synchrotron X-ray diffraction (XRD), Raman spectroscopy, transmission electron microscopy (TEM), synchrotron small-angle X-ray scattering (SAXS), and X-ray photoelectron spectroscopy (XPS). Sets of cylindrical sample pellets were prepared for each material and irradiated at room temperature with 2.2 GeV [197]Au ions (11.1 MeV/u) using the UNILAC linear accelerator at the GSI Helmholtz Centre for Heavy Ion Research in Darmstadt, Germany. Synchrotron XRD patterns of unirradiated samples and those irradiated to each ion fluence were obtained at the National Synchrotron Light Source (NSLS), Brookhaven National Laboratory (λ = 0.407 Å) and the Advanced Photon Source (APS), Argonne National Laboratory (λ = 0.496 Å). Raman measurements were conducted using several laser systems at the University of Michigan (λ = 532 nm, 633 nm, 785 nm). TEM imaging and selected area diffraction were completed using an FEI Tecnai G2 F20 X-TWIN TEM at Stanford University, as well as a JEOL 3100R05 Double C_s-Corrected TEM at the University of Michigan (EMAL). SAXS

data were acquired at the Australian Synchrotron in Melbourne, Australia ($\lambda = 1.127$ Å), and XPS spectra were obtained using a Kratos Axis Ultra XPS at the University of Michigan (EMAL). The combination of these techniques provided sufficient data to characterize the effects of ion irradiation on the structure of each investigated material for the first time.

The experimental results of this study have been written as three journal articles, two of which are under peer-review, and are presented in Chapter 2, 3, and 4 of this dissertation. Chapter 2, "Phase transformation and chemical decomposition of nanocrystalline SnO_2 under heavy ion irradiation", has been submitted to *Nuclear Instruments and Methods in Physics Research Section B*, and is currently under review. Chapter 3, "Chemical and structural modifications of PbO_2 irradiated by swift heavy ions", will be submitted to the same journal in June, 2015. Finally, Chapter 4, "Amorphization of Ta_2O_5 under swift heavy ion irradiation", has been submitted to *Acta Materialia* and is currently under review. These results complete the body of data for the Group 14 oxide system and offer the information necessary to better understand the relations between a material's properties and its response to radiation.

References:

[1]   T. Lan, C.W. Li, B. Fultz, Phonon anharmonicity of rutile SnO2 studied by Raman spectrometry and first principles calculations of the kinematics of phonon-phonon interactions, Phys. Rev. B. 86 (2012) 134302. doi:10.1103/PhysRevB.86.134302.

[2]   M. Batzill, U. Diebold, The surface and materials science of tin oxide, Prog. Surf. Sci. 79 (2005) 47–154. doi:10.1016/j.progsurf.2005.09.002.

[3]   W.B. White, F. Dachille, R. Roy, High-Pressure--High-Temperature Polymorphism of the Oxides of Lead, J. Am. Ceram. Soc. 49 (1961).

[4]   N.N. Greenwood, A. Earnshaw, Chemistry of the Elements pt.2, in: Chem. Elem., 1997: pp. 374–388.

[5]   W. Andreoni, C. a. Pignedoli, Ta[sub 2]O[sub 5] polymorphs: Structural motifs and dielectric constant from first principles, Appl. Phys. Lett. 96 (2010) 062901. doi:10.1063/1.3308475.

[6]   P.C. Joshi, M.W. Cole, Influence of postdeposition annealing on the enhanced structural and electrical properties of amorphous and crystalline Ta[sub 2]O[sub 5] thin films for dynamic random access memory applications, J. Appl. Phys. 86 (1999) 871. doi:10.1063/1.370817.

[7]   X. Lu, Q. Hu, W. Yang, L. Bai, H. Sheng, L. Wang, et al., Pressure-Induced Amorphization in Single-Crystal Ta2O5 Nanowires: A Kinetic Mechanism and Improved Electrical Conductivity, J. Am. Chem. Soc. (2013) 13947–13953.

[8]   D.K. Avasthi, G.K. Mehta, Swift Heavy Ions for Materials Engineering and Nanostructuring, (2011) 142–230.

[9]   A. Sharma, K.D. Verma, M. Varshney, A.P. Singh, Y. Kumar, Growth of nanopillars in SnO2 thin films by ion irradiation and its gas sensing properties, Adv. Sci. Lett. 4 (2011) 501–507.

[10]   S. Rani, N.K. Puri, S.C. Roy, M.C. Bhatnagar, D. Kanjilal, Effect of swift heavy ion irradiation on structure, optical, and gas sensing properties of SnO2 thin films, Nucl. Instruments Methods Phys. Res. Sect. B Beam Interact. with Mater. Atoms. 266 (2008) 1987–1992. doi:10.1016/j.nimb.2008.02.062.

[11]   O.H. Pakarinen, F. Djurabekova, K. Nordlund, P. Kluth, M.C. Ridgway, Molecular dynamics simulations of the structure of latent tracks in quartz and amorphous SiO2, Nucl. Instruments Methods Phys. Res. Sect. B Beam Interact. with Mater. Atoms. 267 (2009) 1456–1459. doi:10.1016/j.nimb.2009.01.071.

[12]   C.L. Tracy, J. McLain Pray, M. Lang, D. Popov, C. Park, C. Trautmann, et al., Defect accumulation in ThO2 irradiated with swift heavy ions, Nucl. Instruments Methods Phys. Res. Sect. B Beam Interact. with Mater. Atoms. 326 (2014) 169–173. doi:10.1016/j.nimb.2013.08.070.

[13]   T. Wiss, H. Matzke, C. Trautmann, M. Toulemonde, S. Klaumunzer, Radiation damage in UO2, by swift heavy ions, Nucl. Instruments Methods Phys. Res. Sect. B Beam Interact. with Mater. Atoms. 122 (1997) 583–588.

[14]   A. Benyagoub, Mechanism of the monoclinic-to-tetragonal phase transition induced in zirconia and hafnia by swift heavy ions, Phys. Rev. B. 72 (2005) 094114. doi:10.1103/PhysRevB.72.094114.

[15]   M. Lang, F. Zhang, J. Zhang, C. Tracy, A. Cusick, J. von Ehr, et al., Swift Heavy Ion-Induced Phase Transformation in Gd2O3, Nucl. Instruments Methods Phys. Res. Sect. B Beam Interact. with Mater. Atoms. 326 (2014) 121–125.

[16]   S. Hemon, V. Chailley, E. Doorhyee, C. Dufour, F. Gourbilleau, F. Levesque, et al., Phase transformation of polycrystalline Y2O3 under irradiation with swift heavy ions, Nucl. Instruments Methods Phys. Res. Sect. B Beam Interact. with Mater. Atoms. 122 (1997) 563–565.

[17]   B. Schuster, F. Fujara, B. Merk, R. Neumann, T. Seidl, C. Trautmann, Response behavior of ZrO2 under swift heavy ion irradiation with and without external pressure, Nucl. Instruments Methods Phys. Res. Sect. B Beam Interact. with Mater. Atoms. 277 (2012) 45–52. doi:10.1016/j.nimb.2011.12.060.

[18]   W. Weber, Models and mechanisms of irradiation-induced amorphization in ceramics, Nucl. Instruments Methods Phys. Res. Sect. B Beam Interact. with Mater. Atoms. 166-167 (2000) 98–106. doi:10.1016/S0168-583X(99)00643-6.

[19]   V. Kumar, D. Pratap, A. Jain, D.C. Agarwal, I. Sulania, A. Tripathi, et al., Crystalline to amorphous phase transition of tin oxide nanocrystals induced by SHI at low temperature, AIP Conf. Proc. 715 (2012) 715–716. doi:10.1063/1.4710203.

[20]   A. Benyagoub, Investigations by X-ray diffraction of swift heavy ion induced effects in inorganic materials, Nucl. Instruments Methods Phys. Res. Sect. B Beam Interact. with Mater. Atoms. 225 (2004) 88–96. doi:10.1016/j.nimb.2004.03.083.

[21]   C.L. Tracy, M. Lang, J. Zhang, F. Zhang, Z. Wang, R.C. Ewing, Structural response of A2TiO5 (A=La, Nd, Sm, Gd) to swift heavy ion irradiation, Acta Mater. 60 (2012) 4477–4486. doi:10.1016/j.actamat.2012.05.005.

[22]   J.-J. Lee, H.-J. Kim, Y.-G. Kang, Y.-H. Kim, H.-G. Park, B.-Y. Kim, et al., Vertical Liquid Crystal Orientation on Amorphous Tantalum Pentoxide Surfaces Depending on Anisotropic Dipole–Dipole Interaction via Ion Beam Irradiation, Jpn. J. Appl. Phys. 50 (2011) 031701. doi:10.1143/JJAP.50.031701.

[23]   S. Park, M. Lang, C.L. Tracy, J. Zhang, F. Zhang, C. Trautmann, et al., Swift heavy ion irradiation-induced amorphization of La2Ti2O7, Nucl. Inst. Methods Phys. Res. B. 326 (2014) 145–149. doi:10.1016/j.nimb.2013.10.035.

[24]   K. Schwartz, G. Wirth, C. Trautmann, T. Steckenreiter, Ion-induced formation of colloids in LiF at 15 K, Phys. Rev. B. 56 (1997) 10711–10714. doi:10.1103/PhysRevB.56.10711.

[25]   A.B. Cusick, M. Lang, F. Zhang, J. Zhang, C. Trautmann, R.C. Ewing, Phase transformation and chemical decomposition of nanocrystalline SnO2 under heavy ion irradiation, 2015.

[26]   V. Saikiran, N. Srinivasa Rao, G. Devaraju, G.S. Chang, a. P. Pathak, Formation of Ge nanocrystals from ion-irradiated GeO2 nanocrystals by swift Ni ion beam, Nucl. Instruments Methods Phys. Res. Sect. B Beam Interact. with Mater. Atoms. 312 (2013) 1–6. doi:10.1016/j.nimb.2013.07.005.

[27]   S. Takaki, K. Yasuda, T. Yamamoto, S. Matsumura, N. Ishikawa, Atomic structure of ion tracks in Ceria, Nucl. Instruments Methods Phys. Res. Sect. B Beam Interact. with Mater. Atoms. 326 (2014) 140–144. doi:10.1016/j.nimb.2013.10.077.

[28]   J. Jensen, a Dunlop, S. Della-Negra, Microscopic observations of metallic inclusions generated along the path of MeV clusters in CaF2, Nucl. Instruments Methods Phys. Res. Sect. B Beam Interact. with Mater. Atoms. 146 (1998) 399–404. doi:10.1016/S0168-583X(98)00515-1.

[29]   N. Itoh, D.M. Duffy, S. Khakshouri, a M. Stoneham, Making tracks: electronic excitation roles in forming swift heavy ion tracks., J. Phys. Condens. Matter. 21 (2009) 474205. doi:10.1088/0953-8984/21/47/474205.

[30]   R.L. Fleischer, P.B. Price, R.M. Walker, Nuclear Tracks in Solids, University of California Press, 1975.

[31]   G. Schiwietz, K. Czerski, M. Roth, F. Staufenbiel, P.L. Grande, Femtosecond dynamics – snapshots of the early ion-track evolution, Nucl. Instruments Methods Phys. Res. Sect. B Beam Interact. with Mater. Atoms. 226 (2004) 683–704. doi:10.1016/j.nimb.2004.05.043.

[32]   N. Del Fatti, F. Vallee, C. Flytzanis, Y. Hamanaka, A. Nakamura, Electron dynamics and surface plasmon resonance nonlinearities in metal nanoparticles, Chem. Phys. (2000) 215–226.

[33]   M. Toulemonde, W. Assmann, C. Dufour, A. Meftah, F. Studer, C. Trautmann, The Electron-phonon Mean Free Path as a Link between Electronic Energy Deposition and Track Size in Insulators, 11 (2006) 2006.

[34]   M. Toulemonde, C. Dufour, A. Meftah, E. Paumier, Transient thermal processes in heavy ion irradiation of crystalline inorganic insulators, Nucl. Instruments Methods Phys. Res. Sect. B Beam Interact. with Mater. Atoms. 166-167 (2000) 903–912. doi:10.1016/S0168-583X(99)00799-5.

[35]   a. Benyagoub, Phase transformations in oxides induced by swift heavy ions, Nucl. Instruments Methods Phys. Res. Sect. B Beam Interact. with Mater. Atoms. 245 (2006) 225–230. doi:10.1016/j.nimb.2005.11.106.

[36]   G. Szenes, Thermal spike model of amorphous track formation in insulators irradiated by swift heavy ions, Nucl. Instruments Methods Phys. Res. Sect. B Beam Interact. with Mater. Atoms. 2 (1996) 1–4.

[37]   M. Toulemonde, J.M. Costantini, C. Dufour, A. Meftah, E. Paumier, F. Studer, Track creation in SiO2 and BaFe12O19 by swift heavy ions: a thermal spike description, Nucl. Instruments Methods Phys. Res. Sect. B Beam Interact. with Mater. Atoms. 116 (1996) 37–42.

[38]   F. Agulló-López, a. Mendez, G. García, J. Olivares, J. Cabrera, Synergy between thermal spike and exciton decay mechanisms for ion damage and amorphization by electronic excitation, Phys. Rev. B. 74 (2006) 174109. doi:10.1103/PhysRevB.74.174109.

[39]   N. Itoh, Subthreshold radiation-induced processes in the bulk and on surfaces and interfaces of solids, Nucl. Instruments Methods Phys. Res. Sect. B Beam Interact. with Mater. Atoms. 135 (1998) 175–183. doi:10.1016/S0168-583X(97)00523-5.

[40]   A. Rivera, M.L. Crespillo, J. Olivares, R. Sanz, J. Jensen, F. Agulló-López, On the exciton model for ion-beam damage: The example of TiO2, Nucl. Instruments Methods Phys. Res. Sect. B Beam Interact. with Mater. Atoms. 268 (2010) 3122–3126. doi:10.1016/j.nimb.2010.05.068.

[41]   K. Schwartz, C. Trautmann, R. Neumann, Electronic excitations and heavy-ion-induced processes in ionic crystals, Nucl. Instruments Methods Phys. Res. Sect. B Beam Interact. with Mater. Atoms. 209 (2003) 73–84. doi:10.1016/S0168-583X(02)02013-X.

[42]   C. Trautmann, M. Toulemonde, K. Schwartz, J.M. Costantini, a. Müller, Damage structure in the ionic crystal LiF irradiated with swift heavy ions, Nucl. Instruments Methods Phys. Res. Sect. B Beam Interact. with Mater. Atoms. 164 (2000) 365–376. doi:10.1016/S0168-583X(99)01066-6.

[43]   D. Pettifor, R. Podloucky, The structures of binary compounds: II. Theory of the pd-bonded AB compounds, J. Phys. C Solid State Phys. 315 (1986) 315–330.

[44]   K.H. Bennemann, Ultrafast dynamics in solids, J. Phys. Condens. Matter. 16 (2004) R995–R1056. doi:10.1088/0953-8984/16/30/R01.

[45]   G. Sciaini, M. Harb, S.G. Kruglik, T. Payer, C.T. Hebeisen, F.-J.M. zu Heringdorf, et al., Electronic acceleration of atomic motions and disordering in bismuth., Nature. 458 (2009) 56–9. doi:10.1038/nature07788.

[46]   A. Turos, L. Nowicki, F. Garrido, L. Thome, R. Fromknecht, J. Domagala, Polygonisation of Ionic Single Crystals - A New Effect of swift heavy ion bombardment, Acta Phys. Pol. B. 30 (1999).

[47]   F. Garrido, S. Moll, G. Sattonnay, L. Thomé, L. Vincent, Radiation tolerance of fluorite-structured oxides subjected to swift heavy ion irradiation, Nucl. Instruments Methods Phys. Res. Sect. B Beam Interact. with Mater. Atoms. 267 (2009) 1451–1455. doi:10.1016/j.nimb.2009.01.070.

[48]   A. Berthelot, S. Hémon, F. Gourbilleau, C. Dufour, E. Paumier, Behaviour of a nanometric SnO2 powder under swift heavy-ion irradiation: from sputtering to splitting, Philos. Mag. A. 80 (2000) 2257–2281.

[49]   Y. Zhang, W. Jiang, C. Wang, F. Namavar, P.D. Edmondson, Z. Zhu, et al., Grain growth and phase stability of nanocrystalline cubic zirconia under ion irradiation, Phys. Rev. B. 82 (2010) 184105. doi:10.1103/PhysRevB.82.184105.

[50]   A. Benyagoub, Phase stability of the two isomorphs monoclinic zirconia and hafnia under MeV ion irradiation, Acta Mater. 60 (2012) 5662–5669. doi:10.1016/j.actamat.2012.06.030.

[51]   S. Hemon, A. Berthelot, C. Dufour, F. Gourbilleau, E. Dooryhee, S. Begin-Colin, et al., Influence of the crystallite size on the phase transformation of yttria irradiated with swift heavy ions, Eur. Phys. J. B. 19 (2001) 517–523.

[52]   M. Tang, P. Lu, J. a. Valdez, K.E. Sickafus, Ion-irradiation-induced phase transformation in rare earth sesquioxides (Dy[sub 2]O[sub 3],Er[sub 2]O[sub 3],Lu[sub 2]O[sub 3]), J. Appl. Phys. 99 (2006) 063514. doi:10.1063/1.2184433.

[53]   M. Tang, P. Lu, J. a. Valdez, K.E. Sickafus, Heavy ion irradiation effects in the rare-earth sesquioxide Dy2O3, Nucl. Instruments Methods Phys. Res. Sect. B Beam Interact. with Mater. Atoms. 250 (2006) 142–147. doi:10.1016/j.nimb.2006.04.097.

[54] H. Rath, P. Dash, T. Som, P. V. Satyam, U.P. Singh, P.K. Kulriya, et al., Structural evolution of TiO2 nanocrystalline thin films by thermal annealing and swift heavy ion irradiation, J. Appl. Phys. 105 (2009) 074311. doi:10.1063/1.3103333.

[55] L. Douillard, J.P. Duraud, Swift heavy ion amorphization of quartz — a comparative study of the particle amorphization mechanism of quartz, Nucl. Instruments Methods Phys. Res. Sect. B Beam Interact. with Mater. Atoms. 107 (1996) 212–217. doi:10.1016/0168-583X(95)01044-0.

[56] A. Meftah, F. Brisard, J.M. Costantini, E. Dooryhee, M. Hage-Ali, M. Hervieu, et al., Track formation in SiO2 quartz and the thermal-spike mechanism, Phys. Rev. B. 49 (1994) 12457–12463. doi:10.1103/PhysRevB.49.12457.

[57] F. Lu, J. Wang, M. Lang, M. Toulemonde, F. Namavar, C. Trautmann, et al., Amorphization of nanocrystalline monoclinic ZrO2 by swift heavy ion irradiation, Phys. Chem. Chem. Phys. 14 (2012) 12295–12300. doi:10.1039/c2cp41553d.

[58] B. Canut, a Benyagoub, G. Marest, a Meftah, N. Moncoffre, S. Ramos, et al., Swift-uranium-ion-induced damage in sapphire., Phys. Rev. B. Condens. Matter. 51 (1995) 12194–12201. http://www.ncbi.nlm.nih.gov/pubmed/9977988.

[59] T. Aruga, Y. Katano, T. Ohmichi, S. Okayasu, Y. Kazumata, Amorphization behaviors in polycrystalline alumina irradiated with energetic iodine ions, Nucl. Instruments Methods Phys. Res. Sect. B Beam Interact. with Mater. Atoms. 166-167 (2000) 913–919. doi:10.1016/S0168-583X(99)00800-9.

[60] A. Kabir, A. Meftah, J.P. Stoquert, M. Toulemonde, I. Monnet, Amorphization of sapphire induced by swift heavy ions: A two step process, Nucl. Instruments Methods Phys. Res. Sect. B Beam Interact. with Mater. Atoms. 266 (2008) 2976–2980. doi:10.1016/j.nimb.2008.03.151.

[61] H. Ohno, a. Iwase, D. Matsumura, Y. Nishihata, J. Mizuki, N. Ishikawa, et al., Study on effects of swift heavy ion irradiation in cerium dioxide using synchrotron radiation X-ray absorption spectroscopy, Nucl. Instruments Methods Phys. Res. Sect. B Beam Interact. with Mater. Atoms. 266 (2008) 3013–3017. doi:10.1016/j.nimb.2008.03.155.

[62] A. Iwase, H. Ohno, N. Ishikawa, Y. Baba, N. Hirao, T. Sonoda, et al., Study on the behavior of oxygen atoms in swift heavy ion irradiated CeO2 by means of synchrotron radiation X-ray photoelectron spectroscopy, Nucl. Instruments Methods Phys. Res. Sect. B Beam Interact. with Mater. Atoms. 267 (2009) 969–972. doi:10.1016/j.nimb.2009.02.035.

[63] C.L. Tracy, M. Lang, J.M. Pray, F. Zhang, D. Popov, C. Park, et al., Redox response of actinide materials to highly ionizing radiation, Nat. Commun. 6 (2015) 6133. doi:10.1038/ncomms7133.

[64]   A. Kabir, A. Meftah, J.P. Stoquert, M. Toulemonde, I. Monnet, M. Izerrouken, Structural disorder in sapphire induced by 90.3 MeV xenon ions, Nucl. Instruments Methods Phys. Res. Sect. B Beam Interact. with Mater. Atoms. 268 (2010) 3195–3198. doi:10.1016/j.nimb.2010.05.087.

[65]   J.-M. Costantini, F. Beuneu, D. Gourier, C. Trautmann, G. Calas, M. Toulemonde, Colour centre production in yttria-stabilized zirconia by swift charged particle irradiations, J. Phys. Condens. Matter. 16 (2004) 3957–3971. doi:10.1088/0953-8984/16/23/014.

[66]   P.S. Chaudhari, T.M. Bhave, D. Kanjilal, S. V. Bhoraskar, Swift heavy ion induced growth of nanocrystalline silicon in silicon oxide, J. Appl. Phys. 93 (2003) 3486. doi:10.1063/1.1542913.

[67]   N. Tripathi, S. Rath, P.K. Kulriya, S. a. Khan, D. Kabiraj, D.K. Avasthi, Swift heavy ion induced structural modifications in indium oxide films, Nucl. Instruments Methods Phys. Res. Sect. B Beam Interact. with Mater. Atoms. 268 (2010) 3335–3339. doi:10.1016/j.nimb.2010.07.009.

[68]   P.S. Chaudhari, T.M. Bhave, R. Pasricha, F. Singh, D. Kanjilal, S.V. Bhoraskar, Controlled growth of silicon nanocrystallites in silicon oxide matrix using 150MeV Ag ion irradiation, Nucl. Instruments Methods Phys. Res. Sect. B Beam Interact. with Mater. Atoms. 239 (2005) 185–190. doi:10.1016/j.nimb.2005.04.069.

[69]   J. Zhang, J. Lian, F. Namavar, J. Wang, H. Haider, K. Garvin, et al., Nanosized Rutile (TiO2) Thin Film upon Ion Irradiation and Thermal Annealing, J. Phys. Chem. (2011) 22755–22760.

[70]   D. Lienen, Chemical effects in TiO2 and titanates due to bombardment with Ar + and O f ions of different energies (3.5-10 keV), Appl. Phys. A. 63 (1996) 237–242.

[71]   B. Afra, M.D. Rodriguez, C. Trautmann, O.H. Pakarinen, F. Djurabekova, K. Nordlund, et al., SAXS investigations of the morphology of swift heavy ion tracks in α-quartz., J. Phys. Condens. Matter. 25 (2013) 045006. doi:10.1088/0953-8984/25/4/045006.

[72]   J. Hernandez-Rueda, D. Puerto, J. Siegel, M. Galvan-Sosa, J. Solis, Plasma dynamics and structural modifications induced by femtosecond laser pulses in quartz, Appl. Surf. Sci. 258 (2012) 9389–9393. doi:10.1016/j.apsusc.2011.12.020.

[73]   N. Jiang, J. Qiu, J.C.H. Spence, Precipitation of Ge nanoparticles from GeO2 glasses in transmission electron microscope, Appl. Phys. Lett. 86 (2005) 1–3. doi:10.1063/1.1898423.

[74]   T. Asai, Y. Shimotsuma, T. Kurita, A. Murata, S. Kubota, M. Sakakura, et al., Systematic Control of Structural Changes in GeO $_2$ Glass Induced by Femtosecond Laser Direct Writing, J. Am. Ceram. Soc. 98 (2015) 1471–1477. doi:10.1111/jace.13482.

[75]   S.X. Wang, L.M. Wang, R.C. Ewing, Ion irradiation-induced amorphization of two GeO2 polymorphs, Nucl. Instruments Methods Phys. Res. B. 175-177 (2001) 615–619. http://www.sciencedirect.com/science/article/pii/S0168583X00006078.

[76]   S. Hemon, F. Gourbilleau, E. Paumier, E. Dooryhee, TEM study of irradiation effects on tin oxide nanopowder, Nucl. Instruments Methods Phys. Res. Sect. B Beam Interact. with Mater. Atoms. 122 (1997) 526–529.

[77]   A. Berthelot, F. Gourbilleau, C. Dufour, B. Domenges, E. Paumier, Irradiation of a tin oxide nanometric powder with swift heavy ions, Nucl. Instruments Methods Phys. Res. Sect. B Beam Interact. with Mater. Atoms. 167-167 (2000) 927–932.

[78]   A. Berthelot, S. Hemon, F. Gourbilleau, C. Dufour, E. Dooryhee, E. Paumier, Nanometric size effects on irradiation of tin oxide powder, Nucl. Instruments Methods Phys. Res. Sect. B Beam Interact. with Mater. Atoms. 146 (1998) 437–442.

[79]   J. Lin, K. Xiong, J. Robertson, Atomic structure, electronic structure, and band offsets at Ge:GeO:GeO2 interfaces, Appl. Phys. Lett. 97 (2010) 3. doi:10.1063/1.3525371.

[80]   D.O. Scanlon, A.B. Kehoe, G.W. Watson, M.O. Jones, W.I.F. David, D.J. Payne, et al., Nature of the Band Gap and Origin of the Conductivity of PbO2 Revealed by Theory and Experiment, Phys. Rev. Lett. 107 (2011) 246402. doi:10.1103/PhysRevLett.107.246402.

[81]   J.. Jacquemin, G. Bordure, Electronic energy band calculation in β-PbO2 comparison with SnO2 and GeO2 energy band structures, Solid State Commun. 11 (1972) 1563–1567. doi:10.1016/0038-1098(72)90520-0.

[82]   R.R. Krishnan, K.M. Nissamudeen, K.G. Gopchandran, V.P.M. Pillai, V. Ganesan, Effect of doping and substrate temperature on the structural and optical properties of reactive pulsed laser ablated tin oxide doped tantalum oxide thin films, Vacuum. 84 (2010) 1204–1211. doi:10.1016/j.vacuum.2009.10.026.

[83]   A.M. Mazzone, V. Morandi, Defects in nanocrystalline SnO2 studied by Tight Binding, Eur. Phys. J. B. 42 (2004) 435–440. doi:10.1140/epjb/e2004-00401-9.

[84]   T.L. Cottrell, The Strengths of Chemical Bonds, 2nd Ed., Butterworth, London, 1966.

[85]   A.A. Bolzan, C. Fong, B.J. Kennedy, C.J. Howard, Structural Studies of Rutile-Type Metal Dioxides, Acta Crystallogr. Sect. B Struct. Sci. 53 (1997) 373–380. doi:10.1107/S0108768197001468.

[86] D.R. Lide, CRC Handbook of Chemistry & Physics (18th Ed.), (2004).

[87] R. Magruder, D. Kinser, R. Weeks, Effect of Gamma Radiation on the Direct-Current Resistivity of GeO2, Commun. Am. Ceram. Soc. (1983) 1–2.

[88] D.M. Christie, J.R. Chelikowsky, Electronic and structural properties of germania polymorphs, Phys. Rev. B - Condens. Matter Mater. Phys. 62 (2000) 14703–14711. doi:10.1103/PhysRevB.62.14703.

[89] D. Risold, J.-I. Nagata, R.O. Suzuki, Thermodynamic description of the Pb-O system, J. Phase Equilibria. 19 (1998) 213–233. doi:10.1361/105497198770342238.

[90] N. Boubata, A. Roula, I. Moussaoui, Thermodynamic and relative approach to compute glass-forming ability of oxides, Bull. Mater. Sci. 36 (2013) 457–460. doi:10.1007/s12034-013-0494-8.

[91] M. Lenglet, Iono-Covalent Character of the Metal–Oxygen Bonds in Oxides: A Comparison of Experimental and Theoretical Data, Act. Passiv. Electron. Components. 27 (2004) 1–60. doi:10.1080/0882751031000116142.

[92] I.E. Grey, W.G. Mumme, R.S. Roth, The crystal chemistry of L-Ta2O5 and related structures, J. Solid State Chem. 178 (2005) 3308–3314. doi:10.1016/j.jssc.2005.08.011.

[93] J. Robertson, Electronic structure of SnO2, GeO2, PbO2, TeO2 and MgF2, J. Phys. C Solid State Phys. 12 (1979) 4767 – 4776. doi:10.1088/0022-3719/12/22/018.

[94] S. Cahen, N. David, J.M. Fiorani, a. Maître, M. Vilasi, Thermodynamic modelling of the O–Sn system, Thermochim. Acta. 403 (2003) 275–285. doi:10.1016/S0040-6031(03)00059-5.

[95] C. Catlow, A. Stoneham, Ionicity in Solids, Solid State Phys. (1983) 4321–4338. doi:10.1088/0022-3719/16/22/010.

Chapter 2

Phase transformation and chemical decomposition of nanocrystalline SnO$_2$ under heavy ion irradiation

Alex B. Cusick[a], Maik Lang[b], Fuxiang Zhang[c], Jiaming Zhang[d], Christina Trautmann[ef] and Rodney C. Ewing[acd]

[a]Materials Science & Engineering, University of Michigan, Ann Arbor, MI 48109, USA

[b]Nuclear Engineering, University of Tennessee, Knoxville, TN 37996, USA

[c]Earth & Environmental Sciences, University of Michigan, Ann Arbor, MI 48109, USA

[d]Geological Sciences, Stanford University, Stanford, CA 94305, USA

[e]GSI Helmholtz Centre for Heavy Ion Research, D-64291 Darmstadt, Germany

[f]Technische Universität Darmstadt, 64287 Darmstadt, Germany

Abstract

A phase transformation and chemical decomposition have been observed in SnO$_2$ nanopowder irradiated by 2.2 GeV ^{197}Au. X-ray diffraction (XRD), Raman spectroscopy, and transmission electron microscopy (TEM) confirm the transformation from tetragonal SnO$_2$ (*P4$_2$/mnm*) to tetragonal SnO (*P4/nmm*), with trace quantities of β-Sn (*I4$_1$/amd*) evidenced by XRD. At a fluence of approximately 2.0×10^{12} ions/cm^2, diffraction maxima corresponding to SnO were clearly evident and increase in intensity as fluence increases. Rietveld refinement of XRD data enabled the determination of the structures and the proportions of each phase up to a fluence of 2.4×10^{13} ions/cm^2, resulting in a maximum SnO phase fraction of 23.1 ± 0.8 %. Raman

spectra show high photoluminescence (PL) intensity before and during initial SnO formation, reflecting the high oxygen vacancy concentration and their potential importance in SnO formation. Small-angle X-ray scattering (SAXS) analysis provided evidence of ion tracks with similar electron density as compared to the SnO_2 matrix, providing a possible explanation as to why no tracks were observed using high-resolution TEM (HRTEM). The transformation likely occurs through a multiple-impact mechanism, based on the accumulation of O vacancies and partially localized Sn reduction.

Keywords: swift heavy ions; irradiation; phase transformation; tin oxide; nanocrystalline; decomposition; reduction

2.1. Introduction

SnO_2 has many applications in materials engineering due to its bulk and surface properties. It finds applications as a transparent conducting oxide, oxidation catalyst, and solid state gas sensor [1]. Under ambient conditions, SnO_2 exhibits the same tetragonal structure as rutile TiO_2 (*P4$_2$/mnm*). The unit cell parameters are: a = b = 4.737 Å and c = 3.186 Å; Z = 2 [2]. Each Sn atom is coordinated with six O atoms, forming columns of slightly-distorted, edge-sharing SnO_6 octahedra. Under hydrostatic pressure of 11.8 GPa, the rutile structure transforms into a $CaCl_2$-type structure (*Pnnm*). At higher pressures: pyrite-type (*Pa$\bar{3}$*), orthorhombic (*Pbca*), and cotunnite-type (*Pnam*) structures can form [3]. The high temperature behavior of SnO_2 has not been well established, as its experimentally measured critical temperatures vary greatly. The melting point has been measured at both 1625°C [4,5] and 2000°C [4], while the vaporization point has been measured at 1830°C [4] and also 2927°C [6]. Thermal decomposition of SnO_2 (to SnO, O_2, and sometimes Sn) has also been observed at temperatures between 1300°C and 1500°C [2,7,8]. This is not consistent with the observation that SnO is unstable above approximately 370°C and decomposes into Sn and SnO_2 [9], albeit the reaction rate is slow. Such variations in measured critical temperatures and high temperature stability suggest that a

28

multi-phase equilibrium may exist at high temperatures. Thus, some combination of SnO_2 melt and vapor, Sn, and gaseous SnO and O_2 may coexist over a range of temperatures.

High energy (swift) heavy ions interact with a solid by dissipating their energy to the material's electronic subsystem along their path. This energy is quantified the ion's "electronic stopping power", or the energy deposited per unit length in the material, often represented as "dE/dx" or "S_e". As an ion passes through the material, the electrons within a cylindrical volume around the ion's trajectory are left in a state of extremely high energy density. This energy is transferred to the atomic lattice leading to varying levels and types of damage, depending on the ion species, energy, charge state, velocity, energy deposition rate, and the material's ability to recover. The processes involved are very complex and are not fully understood, occurring over picosecond to nanosecond time frames. These cylindrical regions of damage are often termed "ion tracks", having dimensions typically on the order of nanometers in diameter and microns in length. Materials with high radiation stability, for example CeO_2 [10–12] and ThO_2 [13], show the formation of defects and lattice effects such as swelling, but no changes in crystalline structure. In other materials, such as SiO_2 [14], Al_2O_3 [15], and various complex oxides [16–21], complete long-range disorder is induced in the ion's wake, forming a fully amorphous track. Some materials have been shown to undergo crystalline-to-crystalline transformations in response to ion irradiation [22–25]. For example, ZrO_2 and HfO_2 undergo a monoclinic-to-tetragonal transformation under swift heavy ion irradiation [22]. Evidence of a different type of radiation response has been observed in GeO_2 [26], CeO_2 [27,10–12], Al_2O_3 [28], yttria-stabilized ZrO_2 [29], UO_3 [12], SiO [30], and InO [31], where observation of some or all of the following related effects have been made: preferential disorder on the O sublattice, O ejection from track cores, cation reduction, and metallic inclusion formation within track cores. These oxides share the aforementioned effects with the alkali-halides, LiF [32] and CaF_2 [33].

To date, no single theoretical model is able to fully explain all of the structural modifications observed in different materials. According to the thermal-spike model [34], the mechanism for transformation is the thermal transient itself, which occurs as the dense electronic excitation is transferred to the lattice through electron-phonon coupling. This thermal-spike is responsible for the formation of a melt phase within tracks, and inducing a pressure wave that propagates

into the surrounding matrix. As energy is quickly dissipated, non-equilibrium amorphous, high temperature, or high pressure phases may be quenched along the ion's path [22,24,25,35]. This model accounts well for these observations, as well as the dependence of amorphous track diameter on the ion stopping power. The observed stability of non-equilibrium phases may be due to the nanoscale track dimensions and kinetic limitations on the ordering process during rapid quenching [36]. Due to its success at describing these processes in many ion-induced phase transformations, the thermal-spike model has been generally accepted.

However, the thermal-spike model has limitations. The aforementioned energy transfer processes are very complex and occur on very short timescales. They therefore occur under highly non-equilibrium conditions. The thermal-spike model, however, relies on assumptions of thermodynamic equilibrium, using equilibrium critical values for melting and vaporization to determine melt-thresholds and track diameters, while assigning free parameters to fit experimental data [37–39]. Also, Arrhenius-type equations are used to account for defect production by ions with sub-threshold energies, assuming the equilibrium generation of thermal defects [40]. The model is also unable to account for material dependent effects, such as differences in track morphology [41] and variations in threshold stopping powers [39]. It is evident that the thermal-spike model must be supplemented with additional theory to enable a more fundamental understanding of ion-solid interactions. Introducing the formation and decay of self-trapped excitons to the previously developed theoretical framework has offered an advance in understanding for some materials [41–43]. The primary role of self-trapped excitons in this context is to localize electronic energy close to the track core; self-trapping renders them immobile and therefore unable to decrease the energy density through outward diffusion, and decay through defect production. Exciton self-trapping has also been associated with a change in cation charge state [39], an effect seen in some irradiated oxides which has yet to be explained.

Due to the potential for SnO_2 in engineering applications, nanoscale modifications to its structure may have significant technological implications. This paper describes a previously unobserved phase transformation involving chemical decomposition under swift heavy ion irradiation of a SnO_2 nanopowder. Synchrotron XRD data provide a detailed structural

characterization over a wide fluence regime; Raman spectroscopy provides insight into the evolution of short range order; SAXS reveals the evolving track morphology; TEM is used to document atomic-scale changes and variations in morphology of individual grains.

2.2. Experimental Methods

Sn(IV) oxide powder was obtained from Alfa Aesar with a theoretical density of 6.96 g/cm^3 and grain sizes between approximately 10 and 20 nm, as determined by TEM. Sample holders were prepared by drilling sets of 200 μm diameter holes (using electron discharge machining) into 50 μm thick stainless steel foils. The powder was then pressed into these holes using a hydraulic press at a pressure of 20 MPa. This formed sets of cylindrical sample pellets held within the foils, each approximately 200 μm in diameter and 50 μm thick. Each set contained seven samples for redundancy, in the event that pellets were lost or damaged during irradiation, characterization, or transportation. Ten sets of samples were prepared and irradiated with 2.2 GeV ^{197}Au ions (11.1 MeV/u) at room temperature, using the UNILAC linear accelerator at the GSI Helmholtz Centre for Heavy Ion Research, in Darmstadt, Germany. The sample sets were irradiated to 10 different fluences, increasing from 5.0×10^{10} to 4.9×10^{13} ions/cm^2. The flux was kept sufficiently low to avoid sample heating during irradiation, which was on average 4×10^9 ions/cm$^2 \cdot$s. SRIM code [44] simulation indicated a projected ion range of 56.6 μm based on the material's theoretical density. However, because the fabrication of the pressed powders was not followed by sintering, the actual sample density was significantly lower than the ideal value. The range was therefore corrected, as described previously by Lang et al. [24], using the actual sample density of approximately 60% of theoretical. The resulting ion range is approximately 90 μm, confirming the assumption that all incident ions pass completely through the sample thickness. The electronic stopping power, S_e, was determined to have an approximately constant profile through the sample thickness, with an average value of 44.2 keV/nm ± 1.0 keV/nm.

Post-irradiation analysis included the use of synchrotron XRD with high energy X-rays (λ = 0.407 Å) at the National Synchrotron Light Source (NSLS), Brookhaven National Laboratory. Data were collected from at least three sample pellets for each fluence. The measurements

were performed in transmission mode using a CCD detector, with an X-ray spot size of 25 μm and an exposure time of 600 s. The diffraction images were integrated with Fit2D software [45]. The resulting diffraction patterns were then quantitatively analyzed using Rietveld refinement conducted with FullProf software [46]. These analyses utilized pseudo-Voigt function models to fit each peak in the diffraction spectra, as well as the background, to obtain information about each phase present at each fluence. Raman measurements were performed in backscattering geometry with a green solid-state laser (λ = 532 nm, E = 2.33 eV) and an Olympus microscope with 100x objective. The laser power was limited to 10 mW to avoid sample heating during the 75 s exposure times. Several measurements were taken on each sample pellet. Samples at various fluences were then dispersed onto holey carbon films supported by Cu grids for TEM analysis. HRTEM imaging and selected area diffraction were completed using an FEI Tecnai G2 F20 X-TWIN TEM with the field emission gun operated at 200 keV. SAXS data were obtained from samples irradiated to 5.0×10^{10} ion/cm^2 at the Australian Synchrotron, using 11 keV X-rays in transmission mode.

2.3. Results

2.3.1. Synchrotron X-ray diffraction

The evolution of diffraction patterns as a function of fluence is shown in Figure 2.1. The diffraction maxima marked "*" in the unirradiated profile, at approximately 6.9° (110), 8.8° (101), and 13.3° (211), correspond to the initial tetragonal SnO$_2$ structure (*P4$_2$/mnm*). All peaks in the unirradiated sample pattern fit very well with the tetragonal SnO$_2$ refinement model; thus, the SnO$_2$ is considered to be pure. The relatively broad diffraction maxima are consistent with the presence of nanocrystalline particles, as shown by TEM analysis. A second set of diffraction maxima become evident at a fluence of 2.0×10^{12} ions/cm^2. These are marked "#" in the high fluence profile at approximately 7.8° (101), 8.7° (110), 12.3° (200), and 13.0° (112). These peaks show an increase in relative intensity as fluence increases, as compared with those of SnO$_2$. Through Rietveld refinement, it was determined that these diffraction maxima correspond to tetragonal SnO (*P4/nmm*). Note that these peaks are initially shifted from the position they assume at high fluences, indicating microstrain in the SnO structure upon initial

formation. In addition, the emergence of a third set of diffraction maxima was identified, labeled "β", which also become observable at a fluence of 2.0×10^{12} ions/cm^2. These maxima generally appear to increase in intensity with fluence, however, their intensity is highly variable (sample to sample, even at the same fluence), and never reach an intensity sufficient for quantitative analysis. Although it was not possible to refine this structure, these peaks agree well with the tetragonal form of metallic tin, β-Sn ($I4_1/amd$). The labelled diffraction maxima in Figure 2.1 at 8.3° and 11.3° most likely correspond to the (200) and (211) Sn spacings, the two highest intensity maxima in this structure.
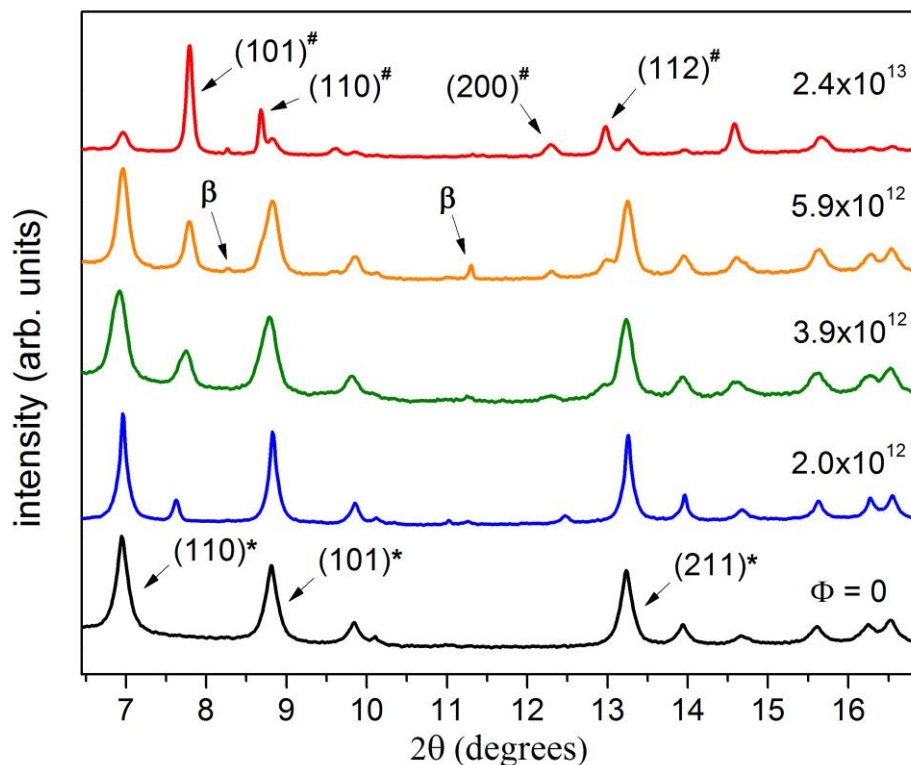
Figure 2.1. Representative synchrotron-XRD patterns of unirradiated and irradiated SnO$_2$ for a range of fluences (ions/cm^2). The peaks labeled "*" on the unirradiated profile correspond to the most prominent SnO$_2$ diffraction maxima, and those labeled "#" on the high fluence profile correspond to those of SnO. Those marked "β" correspond to metallic β-Sn.

Because the superposition of SnO$_2$ and SnO refinement models accounts for all peaks in each high fluence profile (except the two associated with metallic Sn), the high fluence samples must

contain a mixture of only these three structures. This suggests the loss of O during irradiation. No amorphous phase was evident, which can be seen in the refinement models shown in Figure 2.2. Diffraction maxima widths show slight variation as a function of fluence, but no systematic trends. At a fluence of 2.0×10^{12} ions/cm^2, the first evidence of phase transformation is observed as peaks emerge at approximately 7.6° and 12.5° with moderate intensity (corresponding to SnO), as well as 8.3° and 11.3° at very low intensity (corresponding to metallic Sn). All diffraction patterns of samples irradiated to this fluence show these peaks. One of three diffraction patterns at 6.8×10^{11} ions/cm^2 also showed these peaks, albeit at very low intensity. Because the intensity contribution from metallic Sn is very low in all profiles, as compared with SnO$_2$ and SnO, these peaks will not be considered in further analysis. At a fluence of 5.9×10^{12} ions/cm^2, SnO peaks have shifted to approximately 7.8° and 12.3°, and remain at these positions for all of the higher fluence patterns. At a fluence of 3.9×10^{12} ions/cm^2, the aforementioned peaks are in the process of transitioning, which can be seen by the composite nature of the (101) maxima, comprised of overlapping 7.6° and 7.8° peaks, as well as the broad width of the (200), comprised of overlapping 12.5° and 12.3° peaks. These observations are important to understanding the environment in which initial formation of SnO occurs, as the initial peak shifts are related to anisotropic strain. The degree of structural distortion may be defined as a spontaneous strain, where the square root of squared strain tensor eigenvalues is divided by 3 [47]. This formulation yields an estimated strain of 2.6% for the SnO phase when initially formed.
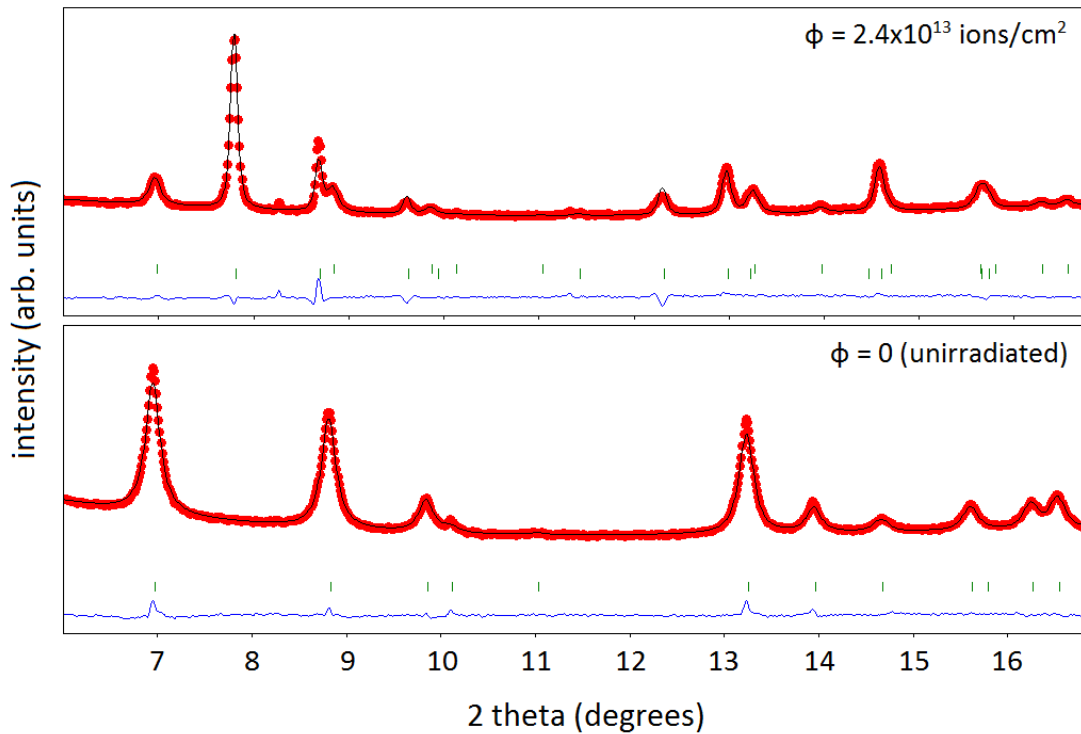
Figure 2.2. Rietveld refinement model (black) superimposed onto experimental XRD data (red), showing that the SnO$_2$ structure model agrees very well with the unirradiated data and that a superposition of SnO$_2$ and SnO models is in excellent agreement with the high fluence data. The green vertical lines under each profile represent expected peak positions, while the blue lines below these show the small difference between refinement model and measured data.

The relative proportion of SnO *vs.* SnO$_2$ can be estimated at each fluence by determining each phase's individual contribution to the total diffraction area. The relative integrated intensities of each phase are calculated during refinement. The SnO "phase fraction" can therefore be calculated by forming a ratio of phase contributions from the SnO phase, to the total profile area (the sum of both phases). The results are shown in Figure 2.3. The proportion of SnO clearly increases with increasing fluence, reaching a maximum SnO phase fraction of 23.1 ± 0.8 % at the maximum fluence of 2.4×10^{13} ions/cm^2. Although the impact mechanism cannot be determined due to limited data, the increase in SnO is relatively slow, suggesting either a very small track size or a multi-impact transformation mechanism. The up-down variation of values in the intermediate fluence regime may be due to uncertainties in the

fluence values, or heterogeneity in the transformed regions, as the X-ray spot size was approximately 12 μm.
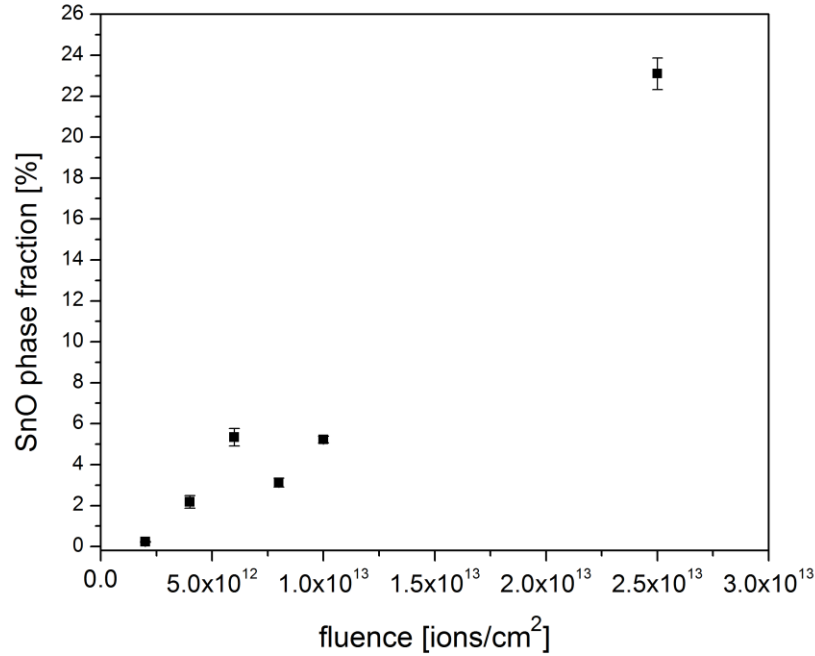
Figure 2.3. The relative quantities of SnO and SnO$_2$ estimated on the basis of Rietveld refinement of the XRD data.

2.3.2. Raman Spectroscopy

Raman spectra from the unirradiated samples (Figure 2.4) show two prominent bands at approximately 633 cm^{-1} and 774 cm^{-1}, which correspond to the highest intensity Raman-active vibrational modes of SnO$_2$ (A$_{1g}$ and B$_{2g}$, respectively) [1]. Along with these modes, a broad peak centered about 574 cm^{-1} is evident, corresponding to surface defect states typically observed in nanocrystalline SnO$_2$. This band is associated with O vacancies in the in-plane sites at the nanocrystalline surfaces [48] and potentially the trapping of electrons into bound states [49].

All Raman-active bands quickly decrease in intensity with respect to background as fluence increases. Two lower frequency peaks emerge at high fluences as the background intensity diminishes. These bands correspond to the B$_{1g}$ and A$_{1g}$ vibrational modes of tetragonal SnO, observed at 113 cm^{-1} and 210 cm^{-1}, respectively [50]. The SnO$_2$ bands are not observed with any appreciable intensity at high fluences, although the A$_{1g}$ mode still produces a small maximum at

633 cm^{-1}. The Raman bands of SnO become evident at a fluence of 3.9x10^{12} ions/cm^2 (and all higher fluences), the same fluence at which the newly emerged SnO diffraction maxima begin to assume their relaxed positions. These data independently confirm the formation of crystalline SnO due to swift heavy ion irradiation. The highest fluence investigated using Raman spectroscopy (shown in Figure 2.4) is 9.8×10^{12} ions/cm^2 due to loss of the majority of material irradiated to higher fluences. At this fluence, there is sufficient evidence of the Raman-active vibrational modes of SnO, and for higher fluences we would expect a further increase in intensity.
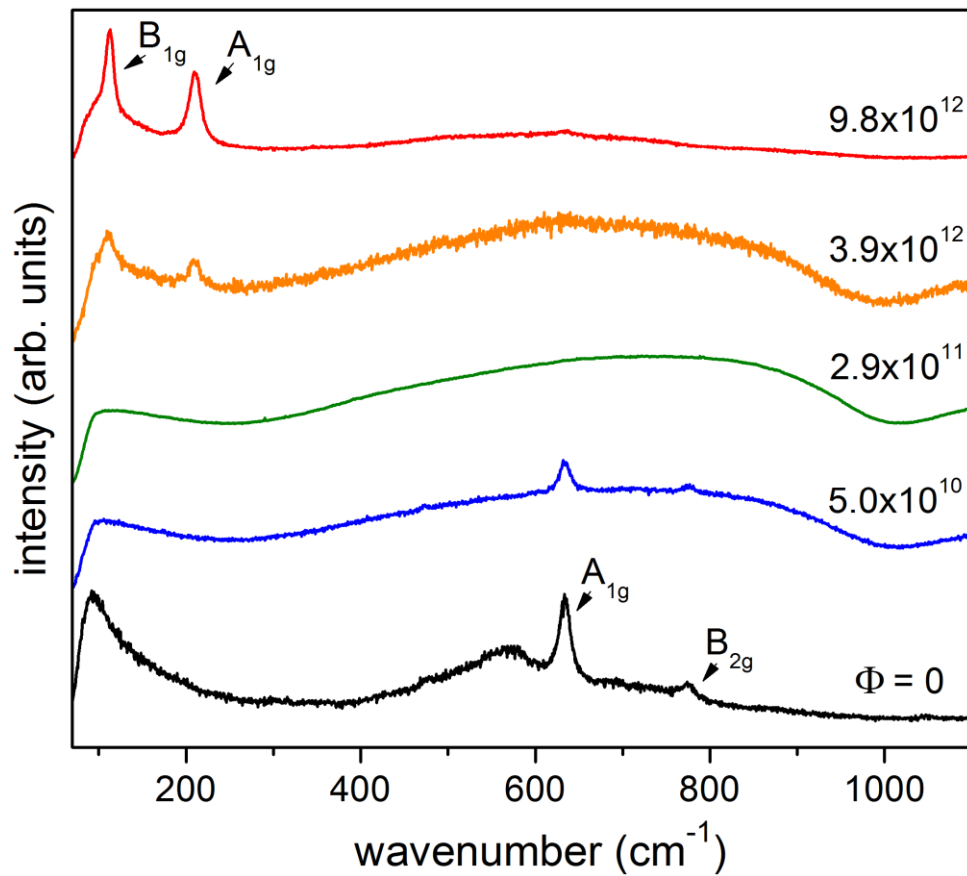

Figure 2.4. Representative Raman spectra for a range of fluences. The labeled peaks in the unirradiated profile correspond to the most prominent SnO$_2$ vibrational modes. The labeled peaks in the high fluence spectrum correspond to SnO vibrational modes.

In the intermediate fluence range of 2.9×10^{11} ions/cm^2 to 2.0×10^{12} ions/cm^2, no Raman-active bands are observable, and the spectra are dominated by a high-intensity broad background. This regime is prevalent for an order of magnitude increase in fluence. This smooth, diffuse background is most likely caused by enhanced photoluminescence (PL), directly resulting from high defect concentrations induced by the irradiation. This high background may obscure the relatively weak Raman band intensities. It is also possible that the high defect concentrations interfere with the Raman-active modes, rendering them unobservable regardless of background intensity. It has been shown that PL intensity of SnO$_2$ depends strongly on the degree of crystallinity [51], as its origin is related to the decay of F-centers and weakly bound electrons to surface-related defects, primarily those involving O vacancies [52,53]. Along with the 532 nm excitation wavelength, the samples were also investigated with a 785 nm laser in an attempt to avoid this luminescence. Excitation with the longer wavelength resulted in a similar high-count background with no observable Raman bands, though the intensity was significantly lower. The existence of high PL intensities over the intermediate fluence regime is important to understanding the mechanism of phase transformation and will be discussed in detail below.

2.3.3. Transmission electron microscopy

Changes in structure and grain morphology due to irradiation were investigated using TEM. An image comparison of unirradiated and high-fluence samples is shown in Figure 2.5. The top row of images (Figure 2.5(a)) show unirradiated grains (left), a high-resolution image of a single grain (center), and a selected area electron diffraction pattern of this region (right). The grains are periodic and have sharply defined edges, with an approximate size distribution between 10 and 20 nm. The diffraction pattern consists of continuous rings that confirm that the unirradiated material is composed of nanoscale particles, with d-spacings consistent with SnO$_2$.
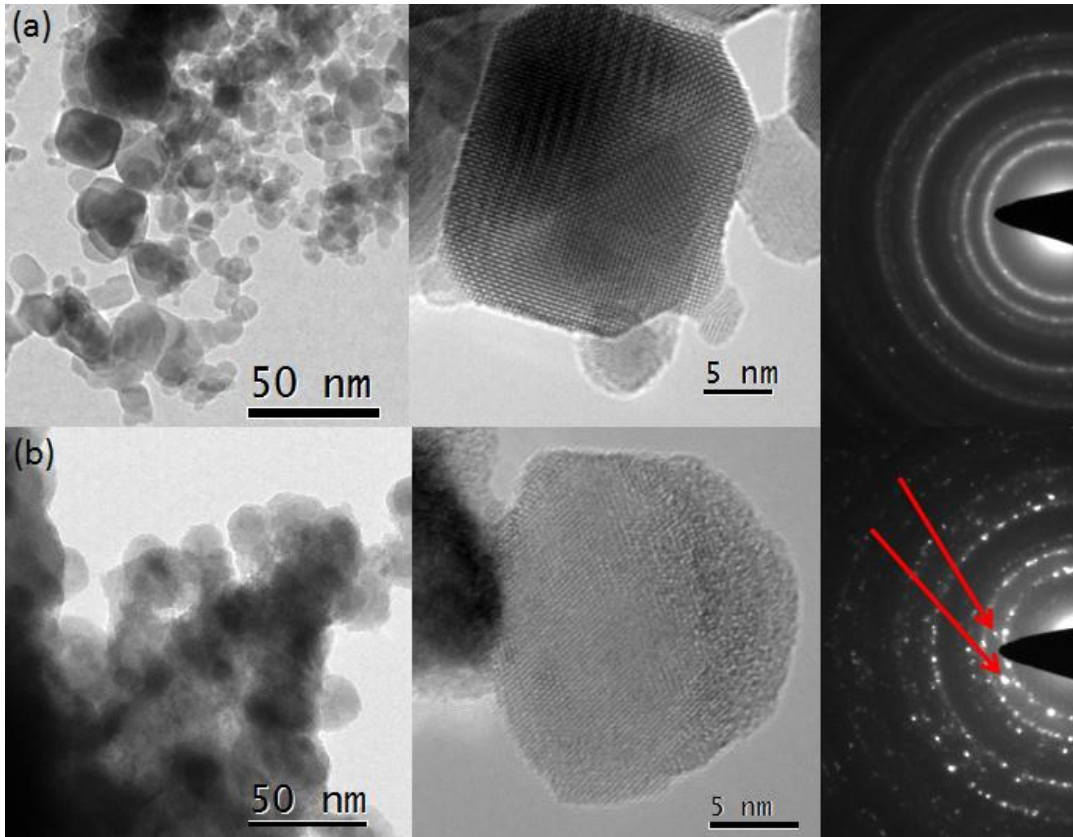
Figure 2.5. TEM images of the unirradiated material (a) and samples irradiated to the maximum fluence of 2.4×10^{13} ions/cm^2 (b). Aggregates of grains are imaged on the left, high resolution images of single grains in the center, and electron diffraction patterns on the right. Arrows indicate diffraction maxima that correspond to tetragonal SnO.

The bottom row of images (Figure 2.5(b)) shows that irradiation to a fluence of 2.4×10^{13} ions/cm^2 has changed the grain morphology and structure significantly. The particles clearly show some degree of agglomeration after irradiation (left). The high resolution image (center) shows a representative grain which has a discontinuous lattice and rounded edges, and happens to be of similar size to the unirradiated grain in Figure 2.5(b). The diffraction pattern (right) confirms the presence of SnO at high fluence, as the two marked diffraction spots have d-spacings that correspond to the (101) of SnO. All of the initially continuous rings became "spotty" after irradiation, indicating that ion-induced grain growth occurred. The electron diffraction pattern of the high-fluence sample is dominated by the SnO$_2$ structure, yet there is clear evidence of the presence of SnO. Despite considerable effort, no ion tracks were observed in samples irradiated to 5.0×10^{10} ions/cm^2 or at any higher fluences. This suggests that the

difference in density between track regions and the matrix is low, and therefore the structures are likely to be very similar. This may imply that overlapping damage regions are required for the transformation to occur, suggesting a multi-impact transformation mechanism.

2.3.4. Small-angle X-ray Scattering

Strong scattering was observed for samples irradiated to 5.0×10^{10} ions/cm^2. Low intensity curved streaks were seen, centered at the beam stop. These features changed orientation as the sample was tilted, indicating the presence of ion tracks. Intensity profiles were extracted and analyzed after background subtraction. Using a hard cylinder model, assuming constant density along the track and sharp boundaries, an average track radius was determined to be approximately 4.0 ± 1.0 nm. The large uncertainty is due to the low streak intensities (significantly lower than those of the matrix), most likely representing a small difference in electron density between the track regions and matrix. This is consistent with TEM results, as no tracks were observable. Thus, it is likely that these single ion tracks consist of SnO$_2$ in a highly defective state; this, along with defect ordering, may provide an environment suitable for the formation of SnO upon subsequent impacts. Using the estimated track size obtained in the SAXS analysis, track overlap should occur at a fluence of approximately 2.4×10^{12} ± 1.1×10^{12} ions/cm^2. Although there is a large uncertainty, this estimation agrees well with the initial observation of SnO in the XRD data at 2.0×10^{12} ions/cm^2.
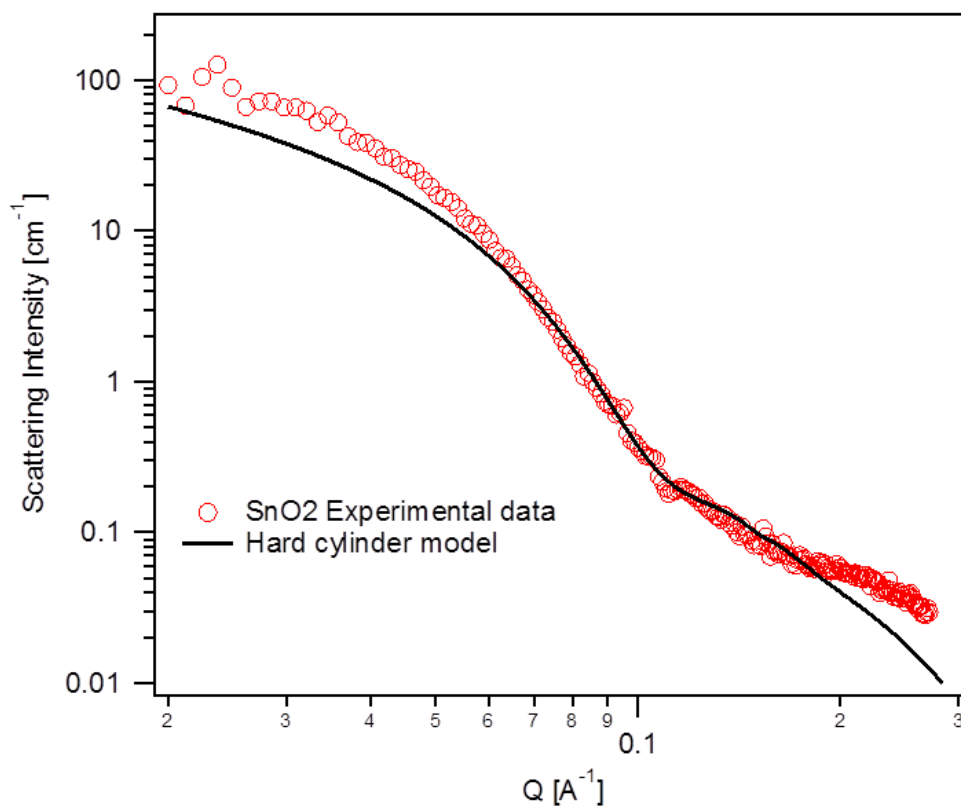
Figure 2.6. SAXS intensity (red) vs. scattering vector, along with the best fit using a hard cylinder model (black).

2.4. Discussion

In the fluence regime below 2.0×10^{12} ions/cm^2, no irradiation-induced modifications to the long-range periodicity of SnO$_2$ occurred, as there are no significant changes in the relative intensities, widths, or positions of the XRD peaks. Raman spectra clearly show the Raman-active modes of SnO$_2$ (A$_{1g}$ and B$_{2g}$) in their normal positions [1]. TEM images show a regular atomic structure, sharp grain edges, and the smooth and continuous diffraction rings typical of nanocrystalline powders, all of which are consistent with the d-spacings of SnO$_2$. At a fluence of 5.0×10^{10} ions/cm^2, the Raman-active modes begin to decrease in intensity relative to background, providing the first evidence of structural changes due to irradiation.

In the medium fluence regime (approximately 2.9×10^{11} to 2.0×10^{12} ions/cm^2), Raman spectra no longer show the Raman-active modes of SnO_2, and are characterized by intense, diffuse backgrounds due to laser-induced photoluminescence (PL). The PL intensity of SnO_2 depends strongly on the degree of crystallinity [51] and is known to increase with O vacancy concentrations. This is supported by data showing that reduction of SnO_2 in an H_2N_2 atmosphere, causing high O weight loss, induces very large PL intensity [54]. The mechanisms of PL in SnO_2 nanoparticles primarily consist of the decay of F-centers and electrons close to the conduction band, to surface-related defect states (mostly involving O vacancies) having energies within the band gap [52,53]. Irradiation of SnO_2 with 75 MeV Ni ions (1.3 MeV/amu) has been shown to result in a broad luminescence band from 540 - 570 nm, which increased in intensity with increasing fluence [55]. These wavelengths correspond to wavenumbers in the range of approximately 288 cm^{-1} to 1253 cm^{-1}, which agrees well with the observed PL-induced background seen in Figure 2.4. Defect-related increase in PL is not unique to SnO_2. Irradiation induced F-centers have been shown to cause high PL intensity in Al_2O_3 [56] and In_2O_3 [57]. In ZnO, high PL intensity was ascribed to recombination of delocalized electrons with vacancy-related defects [58,59].

It is therefore evident from Figure 2.4 that irradiation of SnO_2 has induced high defect concentrations in this fluence regime. Most significant are O vacancies, to which Raman spectroscopy is very sensitive [60]. This provides a strong argument for the role of O vacancies in the transformation process, as high defect concentrations exist well before SnO forms, and decrease as the phase begins to form and assumes a relaxed structure. In other words, high O vacancy concentrations may be the driving force for the transformation. Although this fluence regime is characterized by high defect concentrations, XRD patterns remain consistent with the pure and crystalline SnO_2 structure below 2.0×10^{12} ions/cm^2. Thus, short-range order is lost to some extent, while little or no change occurs in the long-range SnO_2 structure. Increases in XRD peak widths due to defect accumulation and lattice strain were not observed in this fluence regime, but small changes may be masked by the broad peaks that are typical of nano-scale materials.

New, low-intensity diffraction peaks begin emerging at a fluence of 2.0×10^{12} ions/cm^2, corresponding to the early stages of SnO formation. These new peaks, however, are shifted from positions typical of tetragonal SnO. The peaks which correspond to the (101) are shifted by 0.2° to a lower two-theta value, and those that correspond to the (200) are shifted by 0.2° to a higher two-theta value. This suggests that upon initial formation of the SnO phase, the *a*-parameter was compressed and the *c*-parameter was stretched in comparison to their typical values. The degree of lattice strain is estimated to be 2.6%. This anisotropic strain is due to stresses experienced by the SnO phase emerging within SnO_2, which may be related to defect ordering. Also at this fluence, very low intensity peaks are observed at approximately 8.3° and 11.3°, corresponding to the β-Sn phase. This phase represents a small proportion of Sn atoms that have been reduced to the neutral state and have crystallized. Although defect concentrations are high, the SnO_2 diffraction maxima become *more* defined at this fluence, with lower peak widths. This is likely associated with the TEM observation of particle agglomeration. Electron diffraction shows an increase in effective gain size at this fluence.

At a fluence of 3.9×10^{12} ions/cm^2, the initial SnO diffraction maxima have begun to "shift" to positions consistent with the expected values as the structure relaxes. These peaks remain in these positions for all higher fluences. The SnO diffraction maxima actually consist of overlapped peaks, corresponding to both strained and relaxed positions, showing that the relaxation process is only partially complete. At this fluence, the SnO_2 diffraction maxima appear to broaden, which is likely associated with increased lattice disorder due to further irradiation, the associated microstrain, and the increasing quantity of SnO_2-SnO interfaces.

XRD data show a clear structural transition to tetragonal SnO (and minor β-Sn) only after the Raman spectra have remained overwhelmed by PL for almost an order of magnitude increase in fluence. This suggests that high defect concentrations may be an important precursor to the transformation, as this condition precedes the onset of diffraction maxima and Raman bands characteristic of SnO. This is consistent with a multi-impact mechanism as this intermediate defect-rich SnO_2 phase may be necessary for the transformation to occur. The diffraction maxima from the initial SnO phase (at approximately 2.0×10^{12} ions/cm^2) precede the onset of SnO Raman bands, suggesting that long-range periodicity of SnO is attained prior to full short-

range crystallization. This also suggests that SnO begins to stabilize while defect concentrations are high.

The Raman-active modes of SnO become evident at a fluence of 3.9×10^{12} ions/cm^2, the same fluence at which XRD patterns show the presence of a relaxed SnO phase. This indicates that the O vacancy concentration (as well as other luminescence-inducing defects) has decreased, allowing observation of the Raman-active modes from the newly emerging structure. This may be associated with a general increase in short range order related to the reduction of radiation-induced defects as they are incorporated into the SnO structure during its formation. At a fluence of 2.4×10^{13} ions/cm^2, XRD patterns show that the SnO peak intensities dominate those of SnO_2, although Rietveld refinement indicates that the majority phase is still SnO_2 due to its higher contribution to the profile area. Because these peak intensities are related to the site occupancy, this reflects the defective nature of the SnO_2 structure. This is also evident in the Raman spectra, as the SnO bands are significantly higher in intensity than those of the SnO_2 phase. This may reflect that defects in SnO_2 are interfering with its Raman-active modes. Because loss of oxygen is more efficient at the pellet surfaces than in the interior, the surfaces may contain higher quantities of SnO. As only the surfaces are investigated by Raman spectroscopy (the laser extinction length is on the order of microns), the SnO band intensities may reflect the relatively higher SnO concentration at the surface.

TEM analysis shows that the grain structure becomes discontinuous at high fluences, confirming the existence of high defect concentrations and suggesting that SnO_2 and SnO may coexist within the same particle. These particles have also agglomerated. The "spotty" electron-diffraction pattern is consistent with the presence of larger grains than those that are present in the unirradiated sample, and is observed for both SnO_2 and SnO phases. This is consistent with defect-driven grain growth, as observed in previous irradiation studies [61–63]. The high concentrations of defects in medium fluence samples enhance this mechanism and may contribute to the phase transformation by facilitating the formation of a more crystalline, defect-free material. This increase in crystallinity due to irradiation has been shown to occur in many materials and is known as ion beam-induced recrystallization [30,55,64–68]. This process should therefore play a role in the observed agglomeration, as well. The observation of grain

growth may also be associated with an oriented attachment of particles, as there may be preferential binding of like-planes. This spontaneous self-assembly has been identified as the mechanism of nanorod formation from SnO_2 nanoparticles, where particles have been observed to join at their (001) faces, likely due to that plane having the highest surface energy [69].

Although no ion tracks were observed in low fluence samples using HRTEM, SAXS data provided evidence of tracks with inferred diameters of approximately 8.0 ± 2.0 nm. The low streak intensities are probably due to the small difference in electron density between the matrix and damaged regions, which may also explain why tracks were not observable in TEM. Due to this, a well crystallized SnO phase is unlikely to occur within a single ion track, suggesting a multi-impact transformation mechanism. The track region is more likely characterized by a defective SnO_2 structure with approximately the same lattice spacings as the matrix. On the other hand, the lattice parameters of SnO are quite similar to those of SnO_2, making it difficult to distinguish the two phases from one another.

The damage cross-section for the formation of defects appears to be quite high, as the Raman spectra become overwhelmed with PL backgrounds above a low fluence of 5.0×10^{10} ions/cm^2. On the other hand, at a fluence of 2.4×10^{13} ions/cm^2, there is still an appreciable amount of SnO_2 present, indicating a rather low transformation cross-section. At this stage, it is not possible to accurately determine a value for the transformation cross-section, as this would require information at higher fluences that is not currently available.

By analogy with previous studies, it is likely that the effective removal of O, indirectly observed in this study, occurs by anion ejection from the track core [26–28,32,33]. The addition of the self-trapped exciton decay mechanism to the thermal-spike model may account for this observation. As O atoms are ejected, a simultaneous redox reaction likely occurs in which the Sn^{4+} is reduced to Sn^{2+}, as O atoms become neutral. With energy provided by the thermal-spike and/or exciton decay, free O atoms may quickly diffuse away from the track-core region. This diffusion is facilitated by the unusually high diffusion rates observed in sub-stoichiometric and irradiated oxides, promoting the accumulation of O-vacancies [61]. It has been shown that defects that lead to oxygen deficiency are favored in SnO_2. This is because charge is

compensated by a delocalized reduction of surrounding Sn atoms, forming the most stable defect in SnO_2 [70]. DFT calculations have shown the reduction to be partially localized on the three Sn atoms surrounding the O vacancy [70]. This reduction results in a change in Sn coordination from 6 to 5, which stabilizes the local structure, yet makes the material more susceptible to further reduction [70]. The formation of O vacancies is facilitated by the ease with which Sn^{4+} reduces to Sn^{2+} and coordination changes to compensate the charge imbalance. This is a likely mechanism by which the SnO phase is formed from the initial SnO_2 structure. In addition, the cohesive energies of SnO and SnO_2 (the energies needed to separate the solid into single neutral atoms) are comparable at 4.36 and 4.91 eV, respectively [71]. This phase change is further facilitated by the increase in size of Sn^{2+} versus Sn^{4+}, compensating for the local tensile strain caused by the removal of O atoms from the transformed regions.

Energy deposited by the ions in combination with a high vacancy concentration may lead to defect ordering [72], causing a "collapse" of the SnO_2 structure into SnO. The change in unit cell volume after transformation is small, decreasing slightly from 71.5 $Å^3$ to 69.3 $Å^3$. Because of this, and the fact that both structures are tetragonal, the phase transition can occur with only small changes to Sn positions. O vacancies in SnO_2 lead to symmetry changes, and as a result, O positions are no longer equivalent. Vacancies may then order into energetically preferred sites, potentially leading to an effective removal of an entire plane of oxygen at high vacancy concentrations. At this point, a restructuring of O atoms, with only a slight relaxation of Sn atoms, directly results in the formation of tetragonal SnO. The accumulation of O vacancies and Sn reduction during irradiation may therefore be the driving force for transformation, suggesting a multi-impact mechanism. This is also consistent with the absence of amorphization, as it may be more energetically favorable to transform into SnO. Multi-impact mechanisms have been previously proposed for several crystalline-to-crystalline transformations induced by ion irradiation, such as those observed in ZrO_2, HfO_2, and Dy_2O_3 [22,35,73,74].

O atoms may be ejected from the damaged regions and reach the nanoparticle surfaces quickly due to their high kinetic energy and high mobility in vacancy-rich, substoichiometric SnO_2. O diffusion has also been shown to be three to four orders of magnitude greater at oxide

grain boundaries than in the bulk [61]. The O may therefore diffuse to the particle surfaces, traverse to the pellet surface by grain boundary diffusion, and quickly be lost to the beamline vacuum. Preferential disorder on the O sublattice and O ejection from ion track cores have been observed in several oxides irradiated with swift heavy ions, as previously noted. Irradiation of GeO_2 resulted in the removal of O atoms from the irradiated region and the reduction of Ge^{4+} to Ge^0. This led to the formation of Ge nanocrystals, surrounded by O-rich GeO_2 [26]. Irradiation of CeO_2 was shown to cause the reduction of Ce^{4+} to Ce^{3+} [10–12] and O-deficient track cores surrounded by O-rich regions [27], revealing a similar ejection process. Preferential disorder on the O sublattice was observed in the irradiation of Al_2O_3 [28], and reduction of Zr^{4+} to Zr^{3+} was observed in irradiated yttria-stabilized ZrO_2 [29]. In addition, irradiation of SiO has resulted in the formation of Si and SiO_2 nanocrystals [75], and irradiation of InO led to In nanocrystal formation along the track core, surrounded by In_2O_3 [31]. Oxygen loss has also been measured in lower energy irradiation studies of oxides such as cubic-ZrO_2 [61] and TiO_2 [66,76]. Very similar radiation effects are seen in the alkali-halides, as reduced cation clusters were found to form within track cores in LiF [32], CaF2 [33], also resulting in mobile F atoms that were likely ejected from the core.

All of the measurements discussed here support a mechanism of preferential anion displacement after energy transfer from the electronic subsystem, which is closely related to a simultaneous redox reaction. It was proposed that this type of radiation response mechanism is fundamentally different than the damage accumulation in non-reducible materials, as it is driven by the redox reaction itself [12]. All of the materials discussed here are known to form self-trapped excitons: SnO_2 [77,78], GeO_2 [79], CeO_2 [80], Al_2O_3 [81], ZrO_2 [82], TiO_2 [83], LiF [32], CaF2 [33]. Although for CeO_2, the definition of "self-trapped" must be used loosely, and in ZrO_2, these exciton states have been seen only at very low temperatures. Nevertheless, there may be a connection between preferential O loss and the direct formation of Frenkel-pairs by the decay of self-trapped excitons.

There has been evidence, using HRTEM, that ions with S_e within the range of this study (44.2 keV/nm) leave behind empty cylindrical holes in nanocrystalline SnO_2; the material was proposed to have vaporized due to the thermal-spike and escaped the particles [5,84,6,85]. The

nanograins used in the previous studies were irradiated after being dispersed onto TEM grids, which exposed the entire surface of each particle to vacuum during irradiation, thereby facilitating material loss. In contrast, the samples used in this study were pressed powders, which had direct vacuum-exposed boundaries only on the front and back faces of the cylindrical pellets. Due to the inherent porosity of these samples, vaporized material (if indeed formed during irradiation) would be able to expand into these cavities but not entirely escape the sample. Although the high temperature behavior of SnO_2 is not well understood, decomposition into gaseous SnO and O_2 has been measured to occur at temperatures between 1300 and 1500°C [2,7,8]. It is possible that this thermally-induced formation of SnO molecules could drive the production of the SnO phase, which would imply a single-impact process that would fit well with the previous studies. Despite their convincing application of this model, it is likely that the transformation observed in the current study occurs by an entirely different mechanism.

The data presented in this study provides a strong case for a defect-driven, multi-impact transformation mechanism. Low intensity streaks in the SAXS data suggest that tracks have an electron density very close to the surrounding SnO_2. Thus, track regions likely consist of defective SnO_2 with the same or very similar lattice spacings as compared to the surrounding matrix. This would also explain why tracks were not observable using HRTEM, as low contrast would be expected. Thus, single ion tracks probably do not consist of empty holes or the SnO phase. A thermally-driven single-impact mechanism is therefore unlikely. Also, the slow increase of the SnO phase fraction represents a transformation that is relatively inefficient, which would also support a multi-impact mechanism. The Raman spectra show high PL intensity leading up to the initial formation of SnO seen in the XRD data, indicating that a high O vacancy concentration may be a necessary precursor to the transformation. In addition, O vacancies are charge compensated by the reduction of surrounding Sn atoms, creating a favorable environment for the production of SnO after defect accumulation.

We propose that the following sequence of events drive the transformation from SnO_2 to SnO. Electrons thermalize and relax after being highly excited by ion interaction, with some proportion of excitons becoming self-trapped. Energy is transferred to the lattice through

electron-phonon coupling, as well as by the decay of self-trapped excitons, leading to a high temperature transient and defect production. With the deposited energy and enhanced diffusion, O atoms are effectively ejected from the track core, quickly reaching the nanoparticle surfaces where they escape from the solid. The vacancy-rich core is compensated by a delocalized reduction of Sn^{4+} to Sn^{2+} (partially localized on the three Sn atoms surrounding each vacancy), and a related change in Sn coordination from 6 to 5. Once vacancy concentrations reach a threshold, or perhaps after subsequent ion impacts and sufficient defect ordering occurs, the SnO_2 structure "collapses" into the SnO structure. This process is facilitated by transfer of electronic energy to the lattice, the ease of O vacancy formation and partially localized reduction of Sn, and the fact that the SnO structure is energetically favored over SnO_2 for high O vacancy concentrations.

5. Conclusion

A crystalline-to-crystalline phase transformation has been observed in 2.2 GeV ^{197}Au irradiated SnO_2 nanopowder, including chemical decomposition. The transformation from tetragonal SnO_2 (*$P4_2/mnm$*) to tetragonal SnO (*P4/nmm*) also results in trace quantities of β-Sn (*$I4_1/amd$*). XRD data confirm a continuous phase transition with increasing fluence, with no amorphization. Raman spectra confirm the formation of SnO, and also show high PL intensity before and during the initial phase transition, indicating high O vacancy concentrations. TEM images show the effects of particle agglomeration and grain growth during irradiation, as well as the existence of SnO, though no ion tracks were observed. SAXS data provide evidence of tracks with very similar electron densities as compared with the surrounding matrix.

A multi-impact transformation mechanism best describes the experimental results, which is likely driven by O vacancy formation and partially localized reduction of Sn^{4+} to Sn^{2+}. As with other reducible oxides, O atoms may be ejected from the track core, leaving behind reduced Sn ions within a vacancy-rich volume. The removal of O atoms is facilitated by enhanced diffusion rates, which allows them to quickly reach the nanoscale particle surfaces and be lost to beamline chamber vacuum. At high O vacancy concentrations, defect ordering on the O sublattice with small shifts in Sn positions causes a "collapse" to the SnO structure.

References

[1]   T. Lan, C.W. Li, B. Fultz, Phonon anharmonicity of rutile SnO2 studied by Raman spectrometry and first principles calculations of the kinematics of phonon-phonon interactions, Phys. Rev. B. 86 (2012) 134302. doi:10.1103/PhysRevB.86.134302.

[2]   M. Batzill, U. Diebold, The surface and materials science of tin oxide, Prog. Surf. Sci. 79 (2005) 47–154. doi:10.1016/j.progsurf.2005.09.002.

[3]   S. Shieh, A. Kubo, T. Duffy, V. Prakapenka, G. Shen, High-pressure phases in SnO2 to 117 GPa, Phys. Rev. B. 73 (2006) 014105. doi:10.1103/PhysRevB.73.014105.

[4]   G. Paparoni, D. Walker, J.D. Webster, Cassiterite-saturated minimum melting behavior within Sn-SnO2-SiO2 at 1 atm and 10 kbar, Am. Mineral. 95 (2010) 784–798. doi:10.2138/am.2010.3319.

[5]   A. Berthelot, S. Hémon, F. Gourbilleau, C. Dufour, E. Paumier, Behaviour of a nanometric SnO2 powder under swift heavy-ion irradiation: from sputtering to splitting, Philos. Mag. A. 80 (2000) 2257–2281.

[6]   A. Berthelot, F. Gourbilleau, C. Dufour, B. Domenges, E. Paumier, Irradiation of a tin oxide nanometric powder with swift heavy ions, Nucl. Instruments Methods Phys. Res. Sect. B Beam Interact. with Mater. Atoms. 167-167 (2000) 927–932.

[7]   C.L. Hoenig, W. Searcy, Knudsen and Langmuir Evaporation Studies of Stannic Oxide, J. Am. Ceram. Soc. 49 (1966) 128–134.

[8]   E.R. Leite, J.A. Cerri, E. Longo, J.A. Varela, C.A. Paskocima, Sintering of ultrafine undoped SnO2 powder, J. Eur. Ceram. Soc. 21 (2001) 669–675.

[9]   J.C. Platteeuw, G. Meyer, The System Tin + Oxygen, Trans. Faraday Soc. (1956) 1066–1073.

[10]   H. Ohno, a. Iwase, D. Matsumura, Y. Nishihata, J. Mizuki, N. Ishikawa, et al., Study on effects of swift heavy ion irradiation in cerium dioxide using synchrotron radiation X-ray absorption spectroscopy, Nucl. Instruments Methods Phys. Res. Sect. B Beam Interact. with Mater. Atoms. 266 (2008) 3013–3017. doi:10.1016/j.nimb.2008.03.155.

[11] A. Iwase, H. Ohno, N. Ishikawa, Y. Baba, N. Hirao, T. Sonoda, et al., Study on the behavior of oxygen atoms in swift heavy ion irradiated CeO2 by means of synchrotron radiation X-ray photoelectron spectroscopy, Nucl. Instruments Methods Phys. Res. Sect. B Beam Interact. with Mater. Atoms. 267 (2009) 969–972. doi:10.1016/j.nimb.2009.02.035.

[12] C.L. Tracy, M. Lang, J.M. Pray, F. Zhang, D. Popov, C. Park, et al., Redox response of actinide materials to highly ionizing radiation, Nat. Commun. 6 (2015) 6133. doi:10.1038/ncomms7133.

[13] C.L. Tracy, J. McLain Pray, M. Lang, D. Popov, C. Park, C. Trautmann, et al., Defect accumulation in ThO2 irradiated with swift heavy ions, Nucl. Instruments Methods Phys. Res. Sect. B Beam Interact. with Mater. Atoms. 326 (2014) 169–173. doi:10.1016/j.nimb.2013.08.070.

[14] P. Kluth, C.S. Schnohr, O.H. Pakarinen, F. Djurabekova, D.J. Sprouster, R. Giulian, et al., Fine structure in swift heavy ion tracks in amorphous SiO2, Phys. Rev. Lett. 101 (2008) 1–4. doi:10.1103/PhysRevLett.101.175503.

[15] T. Aruga, Y. Katano, T. Ohmichi, S. Okayasu, Y. Kazumata, Amorphization behaviors in polycrystalline alumina irradiated with energetic iodine ions, Nucl. Instruments Methods Phys. Res. Sect. B Beam Interact. with Mater. Atoms. 166-167 (2000) 913–919. doi:10.1016/S0168-583X(99)00800-9.

[16] W. Weber, Models and mechanisms of irradiation-induced amorphization in ceramics, Nucl. Instruments Methods Phys. Res. Sect. B Beam Interact. with Mater. Atoms. 166-167 (2000) 98–106. doi:10.1016/S0168-583X(99)00643-6.

[17] V. Kumar, D. Pratap, A. Jain, D.C. Agarwal, I. Sulania, A. Tripathi, et al., Crystalline to amorphous phase transition of tin oxide nanocrystals induced by SHI at low temperature, AIP Conf. Proc. 715 (2012) 715–716. doi:10.1063/1.4710203.

[18] A. Benyagoub, Investigations by X-ray diffraction of swift heavy ion induced effects in inorganic materials, Nucl. Instruments Methods Phys. Res. Sect. B Beam Interact. with Mater. Atoms. 225 (2004) 88–96. doi:10.1016/j.nimb.2004.03.083.

[19] C.L. Tracy, M. Lang, J. Zhang, F. Zhang, Z. Wang, R.C. Ewing, Structural response of A2TiO5 (A=La, Nd, Sm, Gd) to swift heavy ion irradiation, Acta Mater. 60 (2012) 4477–4486. doi:10.1016/j.actamat.2012.05.005.

[20] S. Park, M. Lang, C.L. Tracy, J. Zhang, F. Zhang, C. Trautmann, et al., Swift heavy ion irradiation-induced amorphization of La2Ti2O7, Nucl. Inst. Methods Phys. Res. B. 326 (2014) 145–149. doi:10.1016/j.nimb.2013.10.035.

[21]   M. Lang, J. Lian, J. Zhang, F. Zhang, W.J. Weber, C. Trautmann, et al., Single-ion tracks in Gd2 Zr2-x Tix O7 pyrochlores irradiated with swift heavy ions, Phys. Rev. B - Condens. Matter Mater. Phys. 79 (2009) 1–9. doi:10.1103/PhysRevB.79.224105.

[22]   A. Benyagoub, Mechanism of the monoclinic-to-tetragonal phase transition induced in zirconia and hafnia by swift heavy ions, Phys. Rev. B. 72 (2005) 094114. doi:10.1103/PhysRevB.72.094114.

[23]   P.M. Ossi, Structural changes induced by swift heavy ions in non-metallic compounds, Nucl. Instruments Methods Phys. Res. Sect. B Beam Interact. with Mater. Atoms. 209 (2003) 55–61. doi:10.1016/S0168-583X(02)02060-8.

[24]   M. Lang, F. Zhang, J. Zhang, C. Tracy, A. Cusick, J. von Ehr, et al., Swift Heavy Ion-Induced Phase Transformation in Gd2O3, Nucl. Instruments Methods Phys. Res. Sect. B Beam Interact. with Mater. Atoms. 326 (2014) 121–125.

[25]   S. Hemon, V. Chailley, E. Doorhyee, C. Dufour, F. Gourbilleau, F. Levesque, et al., Phase transformation of polycrystalline Y2O3 under irradiation with swift heavy ions, Nucl. Instruments Methods Phys. Res. Sect. B Beam Interact. with Mater. Atoms. 122 (1997) 563–565.

[26]   V. Saikiran, N. Srinivasa Rao, G. Devaraju, G.S. Chang, a. P. Pathak, Formation of Ge nanocrystals from ion-irradiated GeO2 nanocrystals by swift Ni ion beam, Nucl. Instruments Methods Phys. Res. Sect. B Beam Interact. with Mater. Atoms. 312 (2013) 1–6. doi:10.1016/j.nimb.2013.07.005.

[27]   S. Takaki, K. Yasuda, T. Yamamoto, S. Matsumura, N. Ishikawa, Atomic structure of ion tracks in Ceria, Nucl. Instruments Methods Phys. Res. Sect. B Beam Interact. with Mater. Atoms. 326 (2014) 140–144. doi:10.1016/j.nimb.2013.10.077.

[28]   A. Kabir, A. Meftah, J.P. Stoquert, M. Toulemonde, I. Monnet, M. Izerrouken, Structural disorder in sapphire induced by 90.3 MeV xenon ions, Nucl. Instruments Methods Phys. Res. Sect. B Beam Interact. with Mater. Atoms. 268 (2010) 3195–3198. doi:10.1016/j.nimb.2010.05.087.

[29]   J.-M. Costantini, F. Beuneu, D. Gourier, C. Trautmann, G. Calas, M. Toulemonde, Colour centre production in yttria-stabilized zirconia by swift charged particle irradiations, J. Phys. Condens. Matter. 16 (2004) 3957–3971. doi:10.1088/0953-8984/16/23/014.

[30]   P.S. Chaudhari, T.M. Bhave, D. Kanjilal, S. V. Bhoraskar, Swift heavy ion induced growth of nanocrystalline silicon in silicon oxide, J. Appl. Phys. 93 (2003) 3486. doi:10.1063/1.1542913.

[31]   N. Tripathi, S. Rath, P.K. Kulriya, S. a. Khan, D. Kabiraj, D.K. Avasthi, Swift heavy ion induced structural modifications in indium oxide films, Nucl. Instruments Methods Phys. Res. Sect. B Beam Interact. with Mater. Atoms. 268 (2010) 3335–3339. doi:10.1016/j.nimb.2010.07.009.

[32]   K. Schwartz, G. Wirth, C. Trautmann, T. Steckenreiter, Ion-induced formation of colloids in LiF at 15 K, Phys. Rev. B. 56 (1997) 10711–10714. doi:10.1103/PhysRevB.56.10711.

[33]   J. Jensen, a Dunlop, S. Della-Negra, Microscopic observations of metallic inclusions generated along the path of MeV clusters in CaF2, Nucl. Instruments Methods Phys. Res. Sect. B Beam Interact. with Mater. Atoms. 146 (1998) 399–404. doi:10.1016/S0168-583X(98)00515-1.

[34]   M. Toulemonde, C. Dufour, A. Meftah, E. Paumier, Transient thermal processes in heavy ion irradiation of crystalline inorganic insulators, Nucl. Instruments Methods Phys. Res. Sect. B Beam Interact. with Mater. Atoms. 166-167 (2000) 903–912. doi:10.1016/S0168-583X(99)00799-5.

[35]   B. Schuster, F. Fujara, B. Merk, R. Neumann, T. Seidl, C. Trautmann, Response behavior of ZrO2 under swift heavy ion irradiation with and without external pressure, Nucl. Instruments Methods Phys. Res. Sect. B Beam Interact. with Mater. Atoms. 277 (2012) 45–52. doi:10.1016/j.nimb.2011.12.060.

[36]   J. Zhang, M. Lang, R.C. Ewing, R. Devanathan, W.J. Weber, M. Toulemonde, Nanoscale phase transitions under extreme conditions within an ion track, J. Mater. Res. 25 (2011) 1344–1351. doi:10.1557/JMR.2010.0180.

[37]   M. Toulemonde, J.M. Costantini, C. Dufour, A. Meftah, E. Paumier, F. Studer, Track creation in SiO2 and BaFe12O19 by swift heavy ions: a thermal spike description, Nucl. Instruments Methods Phys. Res. Sect. B Beam Interact. with Mater. Atoms. 116 (1996) 37–42.

[38]   G. Szenes, Thermal spike model of amorphous track formation in insulators irradiated by swift heavy ions, Nucl. Instruments Methods Phys. Res. Sect. B Beam Interact. with Mater. Atoms. 2 (1996) 1–4.

[39]   N. Itoh, D.M. Duffy, S. Khakshouri, a M. Stoneham, Making tracks: electronic excitation roles in forming swift heavy ion tracks., J. Phys. Condens. Matter. 21 (2009) 474205. doi:10.1088/0953-8984/21/47/474205.

[40]   F. Agulló-López, a. Mendez, G. García, J. Olivares, J. Cabrera, Synergy between thermal spike and exciton decay mechanisms for ion damage and amorphization by electronic excitation, Phys. Rev. B. 74 (2006) 174109. doi:10.1103/PhysRevB.74.174109.

[41]   N. Itoh, Subthreshold radiation-induced processes in the bulk and on surfaces and interfaces of solids, Nucl. Instruments Methods Phys. Res. Sect. B Beam Interact. with Mater. Atoms. 135 (1998) 175–183. doi:10.1016/S0168-583X(97)00523-5.

[42]   A. Rivera, M.L. Crespillo, J. Olivares, R. Sanz, J. Jensen, F. Agulló-López, On the exciton model for ion-beam damage: The example of TiO2, Nucl. Instruments Methods Phys. Res. Sect. B Beam Interact. with Mater. Atoms. 268 (2010) 3122–3126. doi:10.1016/j.nimb.2010.05.068.

[43]   K. Schwartz, C. Trautmann, R. Neumann, Electronic excitations and heavy-ion-induced processes in ionic crystals, Nucl. Instruments Methods Phys. Res. Sect. B Beam Interact. with Mater. Atoms. 209 (2003) 73–84. doi:10.1016/S0168-583X(02)02013-X.

[44]   J.F. Ziegler, M.D. Ziegler, J.P. Biersack, SRIM – The stopping and range of ions in matter (2010), Nucl. Instruments Methods Phys. Res. Sect. B Beam Interact. with Mater. Atoms. 268 (2010) 1818–1823. doi:10.1016/j.nimb.2010.02.091.

[45]   A.P. Hammersley, S.O. Svensson, M. Hanfland, A.N. Fitch, D. Häusermann, FIT2D, (2005).

[46]   J. Rodriguez-Carvajal, FULLPROF Suite, (2011).

[47]   Bilbao Crystallographic Server, (2015). http://www.cryst.ehu.es/ (accessed January 5, 2015).

[48]   L.Z. Liu, X.L. Wu, F. Gao, J.C. Shen, T.H. Li, P.K. Chu, Determination of surface oxygen vacancy position in SnO2 nanocrystals by Raman spectroscopy, Solid State Commun. 151 (2011) 811–814. doi:10.1016/j.ssc.2011.03.029.

[49]   A. Kar, S. Kundu, A. Patra, Surface defect-related luminescence properties of SnO2 nanorods and nanoparticles, J. Phys. Chem. C. 115 (2011) 118–124. doi:10.1021/jp110313b.

[50]   J. Geurts, S. Rau, W. Richter, F.J. Schmitte, SnO FILMS AND THEIR OXIDATION TO SnO2: RAMAN SCATTERING, IR REFLECTIVITY AND X-RAY DIFFRACTION STUDIES, Thin Solid Films. 121 (1984) 217–225.

[51]   D. Wang, J. Yang, X. Li, J. Wang, R. Li, M. Cai, et al., Observation of Surface/Defect States of SnO2 Nanowires on Different Substrates from X-ray Excited Optical Luminescence, Cryst. Growth Des. 12 (2012) 397–402.

[52]   X.T. Zhou, J.G. Zhou, M.W. Murphy, J.Y.P. Ko, F. Heigl, T. Regier, et al., The effect of the surface of SnO2 nanoribbons on their luminescence using x-ray absorption and luminescence spectroscopy., J. Chem. Phys. 128 (2008) 144703. doi:10.1063/1.2841419.

[53]   S. Lettieri, M. Causà, a Setaro, F. Trani, V. Barone, D. Ninno, et al., Direct role of surface oxygen vacancies in visible light emission of tin dioxide nanowires., J. Chem. Phys. 129 (2008) 244710. doi:10.1063/1.3041775.

[54]   S.S. Chang, S.O. Yoon, H.J. Park, Characteristics of SnO2 annealed in reducing atmosphere, Ceram. Int. 31 (2005) 405–410. doi:10.1016/j.ceramint.2004.05.026.

[55]   S. Rani, N.K. Puri, S.C. Roy, M.C. Bhatnagar, D. Kanjilal, Effect of swift heavy ion irradiation on structure, optical, and gas sensing properties of SnO2 thin films, Nucl. Instruments Methods Phys. Res. Sect. B Beam Interact. with Mater. Atoms. 266 (2008) 1987–1992. doi:10.1016/j.nimb.2008.02.062.

[56]   K.S. Jheeta, D.C. Jain, R. Kumar, K.B. Garg, Effect of swift heavy ion irradiation on the optical properties of sapphire, 46 (2008) 400–402.

[57]   N. Tripathi, S. Rath, Effect of Thermal Annealing and Swift Heavy Ion Irradiation on the Optical Properties of Indium Oxide Thin Films, ECS J. Solid State Sci. Technol. 3 (2014) P21–P25. doi:10.1149/2.002403jss.

[58]   T.M. Borseth, B.G. Svensson, a. Y. Kuznetsov, P. Klason, Q.X. Zhao, M. Willander, Identification of oxygen and zinc vacancy optical signals in ZnO, Appl. Phys. Lett. 89 (2006). doi:10.1063/1.2424641.

[59]   X.L. Wu, G.G. Siu, C.L. Fu, H.C. Ong, Photouminescence and cathodoluminescence studies of stoichiometric and oxygen-deficient ZnO films, Appl. Phys. Lett. 78 (2001) 2285–2287. doi:10.1063/1.1361288.

[60]   X.-B. Chen, N.T.M. Hien, I.-S. Yang, D. Lee, T.-W. Noh, A Raman Study of the Origin of Oxygen Defects in Hexagonal Manganite Thin Films, Chinese Phys. Lett. 29 (2012) 126103. doi:10.1088/0256-307X/29/12/126103.

[61]   Y. Zhang, W. Jiang, C. Wang, F. Namavar, P.D. Edmondson, Z. Zhu, et al., Grain growth and phase stability of nanocrystalline cubic zirconia under ion irradiation, Phys. Rev. B. 82 (2010) 184105. doi:10.1103/PhysRevB.82.184105.

[62]   N.G. Deshpande, R. Sharma, Modifications in physical, optical and electrical properties of tin oxide by swift heavy Au8+ ion bombardment, Curr. Appl. Phys. 8 (2008) 181–188. doi:10.1016/j.cap.2007.08.004.

[63]   H. Rath, P. Dash, T. Som, P. V. Satyam, U.P. Singh, P.K. Kulriya, et al., Structural evolution of TiO2 nanocrystalline thin films by thermal annealing and swift heavy ion irradiation, J. Appl. Phys. 105 (2009) 074311. doi:10.1063/1.3103333.

[64] R.S. Chauhan, V. Kumar, D.C. Agarwal, D. Pratap, I. Sulania, a. Tripathi, SHI induced modifications in SnO2 thin films: Structural, optical and surface morphological studies, Nucl. Instruments Methods Phys. Res. Sect. B Beam Interact. with Mater. Atoms. 286 (2012) 295–298. doi:10.1016/j.nimb.2012.01.057.

[65] S. Ezhilvalavan, T.-Y. Tseng, Conduction mechanisms in amorphous and crystalline Ta[sub 2]O[sub 5] thin films, J. Appl. Phys. 83 (1998) 4797. doi:10.1063/1.367272.

[66] J. Zhang, J. Lian, F. Namavar, J. Wang, H. Haider, K. Garvin, et al., Nanosized Rutile (TiO2) Thin Film upon Ion Irradiation and Thermal Annealing, J. Phys. Chem. (2011) 22755–22760.

[67] A. Benyagoub, Phase stability of the two isomorphs monoclinic zirconia and hafnia under MeV ion irradiation, Acta Mater. 60 (2012) 5662–5669. doi:10.1016/j.actamat.2012.06.030.

[68] D.K. Avasthi, G.K. Mehta, Swift Heavy Ions for Materials Engineering and Nanostructuring, Dordrecht : Springer Science+Business Media B.V., 2011.

[69] G. Xi, J. Ye, Ultrathin SnO2 nanorods: Template- and surfactant-free solution phase synthesis, growth mechanism, optical, gas-Sensing, and surface adsorption properties, Inorg. Chem. 49 (2010) 2302–2309. doi:10.1021/ic902131a.

[70] K.G. Godinho, A. Walsh, G.W. Watson, Energetic and Electronic Structure Analysis of Intrinsic Defects in SnO 2, (2009) 439–448.

[71] A.M. Mazzone, V. Morandi, Defects in nanocrystalline SnO2 studied by Tight Binding, Eur. Phys. J. B. 42 (2004) 435–440. doi:10.1140/epjb/e2004-00401-9.

[72] S. Hull, S.T. Norberg, I. Ahmed, S.G. Eriksson, D. Marrocchelli, P. a. Madden, Oxygen vacancy ordering within anion-deficient Ceria, J. Solid State Chem. 182 (2009) 2815–2821. doi:10.1016/j.jssc.2009.07.044.

[73] M. Tang, P. Lu, J. a. Valdez, K.E. Sickafus, Ion-irradiation-induced phase transformation in rare earth sesquioxides (Dy[sub 2]O[sub 3],Er[sub 2]O[sub 3],Lu[sub 2]O[sub 3]), J. Appl. Phys. 99 (2006) 063514. doi:10.1063/1.2184433.

[74] M. Tang, P. Lu, J. a. Valdez, K.E. Sickafus, Heavy ion irradiation effects in the rare-earth sesquioxide Dy2O3, Nucl. Instruments Methods Phys. Res. Sect. B Beam Interact. with Mater. Atoms. 250 (2006) 142–147. doi:10.1016/j.nimb.2006.04.097.

[75] P.S. Chaudhari, T.M. Bhave, R. Pasricha, F. Singh, D. Kanjilal, S.V. Bhoraskar, Controlled growth of silicon nanocrystallites in silicon oxide matrix using 150MeV Ag ion irradiation,

Nucl. Instruments Methods Phys. Res. Sect. B Beam Interact. with Mater. Atoms. 239 (2005) 185–190. doi:10.1016/j.nimb.2005.04.069.

[76]   D. Lienen, Chemical effects in TiO2 and titanates due to bombardment with Ar + and O f ions of different energies (3.5-10 keV), Appl. Phys. A. 63 (1996) 237–242.

[77]   J.B. Varley, a. Janotti, C. Franchini, C.G. Van De Walle, Role of self-trapping in luminescence and p-type conductivity of wide-band-gap oxides, Phys. Rev. B - Condens. Matter Mater. Phys. 85 (2012) 2–5. doi:10.1103/PhysRevB.85.081109.

[78]   R. Liu, Y. Chen, F. Wang, L. Cao, A. Pan, G. Yang, et al., Stimulated emission from trapped excitons in SnO2 nanowires, Phys. E Low-Dimensional Syst. Nanostructures. 39 (2007) 223–229. doi:10.1016/j.physe.2007.04.009.

[79]   A.N. Trukhin, LUMINESCENCE OF A SELF-TRAPPED EXCITON IN GeO2 CRYSTAL, Solid State Commun. 85 (1993) 723–728.

[80]   S. Mochizuki, F. Fujishiro, The photoluminescence properties and reversible photoinduced spectral change of CeO2 bulk, film and nanocrystals, Phys. Status Solidi Basic Res. 246 (2009) 2320–2328. doi:10.1002/pssb.200844419.

[81]   B.R. Namozov, M.E. Fominich, R.I. Zakharchenya, Structure of the self-trapped exciton luminescence in a-Al2O3, Phys. Solid State. 40 (1998) 8–9.

[82]   M. Kirm, J. Aarik, M. Jürgens, I. Sildos, Thin films of HfO 2 and ZrO 2 as potential scintillators, Nucl. Instruments Methods Phys. Res. Sect. A Accel. Spectrometers, Detect. Assoc. Equip. 537 (2005) 251–255. doi:10.1016/j.nima.2004.08.020.

[83]   M. Watanabe, T. Hayashi, Time-resolved study of self-trapped exciton luminescence in anatase TiO2 under two-photon excitation, J. Lumin. 112 (2005) 88–91. doi:10.1016/j.jlumin.2004.09.001.

[84]   S. Hemon, F. Gourbilleau, E. Paumier, E. Dooryhee, TEM study of irradiation effects on tin oxide nanopowder, Nucl. Instruments Methods Phys. Res. Sect. B Beam Interact. with Mater. Atoms. 122 (1997) 526–529.

[85]   A. Berthelot, S. Hemon, F. Gourbilleau, C. Dufour, E. Dooryhee, E. Paumier, Nanometric size effects on irradiation of tin oxide powder, Nucl. Instruments Methods Phys. Res. Sect. B Beam Interact. with Mater. Atoms. 146 (1998) 437–442.

Chapter 3

Chemical and structural modifications of PbO$_2$ irradiated by swift heavy ions

Alex B. Cusick[a], Maik Lang[b], Fuxiang Zhang[c], Zhongrui Li[c], Weixing Li[d], Christina Trautmann[ef] and Rodney C. Ewing[acd]

[a]Materials Science & Engineering, University of Michigan, Ann Arbor, MI 48109, USA

[b]Nuclear Engineering, University of Tennessee, Knoxville, TN 37996, USA

[c]Earth & Environmental Sciences, University of Michigan, Ann Arbor, MI 48109, USA

[d]Geological Sciences, Stanford University, Stanford, CA 94305, USA

[e]GSI Helmholtz Centre for Heavy Ion Research, D-64291 Darmstadt, Germany

[f]Technische Universität Darmstadt, 64287 Darmstadt, Germany

Abstract

PbO$_2$ powders were irradiated by 2.2 GeV ^{197}Au ions to investigate chemical and structural stability under dense electronic excitation. PbO$_2$ separated into multiple lead-oxide compositions, forming six distinct crystalline structures: Pb$_2$O$_3$ (monoclinic), Pb$_3$O$_4$ (orthorhombic), Pb$_3$O$_4$ (tetragonal), PbO (tetragonal), PbO (orthorhombic), Pb (cubic), and an amorphous phase of unknown composition. These structures were identified through analysis of synchrotron X-ray diffraction (XRD) data. Raman spectra confirmed the formation of Pb$_3$O$_4$ and both PbO structures. X-ray photoelectron spectroscopy (XPS) revealed a gradual shift in the 4f peaks of Pb from positions consistent with Pb^{4+} to those of Pb^{2+}, confirming existence of the lower lead oxides. Transition directly to the most stable lead oxide, tetragonal PbO, was

complicated by the stability (or metastability) of the intermediate oxides that combine ions in both valence states (such Pb_3O_4), as they have higher enthalpies of formation as compared with PbO_2. Tetragonal PbO became the dominant phase at high fluences.

Keywords: swift heavy ions; irradiation; phase transformations; lead oxide; radiation effects; decomposition

3.1. Introduction

PbO_2 is a strong oxidizing agent and is used in the production of pyrotechnics, matches, and dyes [1]. However, these applications may be considered secondary to its *in situ* production during the operation of lead-acid batteries [2]. PbO_2 is used as electrodes in this application due to its intrinsic metallic behavior [3], good corrosion resistance (even in highly acidic environments), and high overvoltage properties. Pure PbO_2 exhibits n-type conductivity with carrier concentrations in the range of 10^{19}-10^{21} cm^{-3}, mainly being attributed to O vacancies, Pb interstitials, and the incorporation of hydrogen [4]. The lead-oxygen system has many stoichiometries and structures [1], offering a wide range of properties that have been used to advantage for millennia.

High energy "swift" heavy ions (> 1 MeV/u) have been used to modify the structure and properties of materials at the nanoscale by depositing dense electronic energy into the material's electronic subsystem. As the electronic energy is transferred to the atomic structure, cylindrical damage regions or "tracks" are formed along the ion's trajectory, which are typically microns in length and only nanometers in diameter. In materials susceptible to this damage, swift heavy ions can induce amorphization within the track, the formation of high temperature/high pressure crystalline phases, or modifications to a material's chemical state.

The stable crystalline phase in ambient conditions, β-PbO_2, is tetragonal ($P4_2/mnm$) with $a =$ 4.91 Å, $c =$ 3.39 Å, Z = 2 [5], and is isomorphic to rutile TiO_2 and SnO_2. Known as plattnerite in mineral form, β-PbO_2 is comprised of PbO_6 octahedra that share edges to form chains (Figure 3.1). At pressures greater than 1.3 MPa and temperatures above 100°C, α-PbO_2 forms [2], known as scrutinyite due to its rarity. This phase has an orthorhombic structure (*Pbcn*), with $a =$ 4.97 Å, $b =$ 5.96 Å, $c =$ 5.44 Å, Z = 4. In this structure, PbO_6 octahedra are linked by adjacent

edges to form zigzag chains [6]. As O vacancies are the dominant defect, PbO_2 is inherently prone to substoichiometry [7], in which charge is compensated through electrons in the conduction band [8].
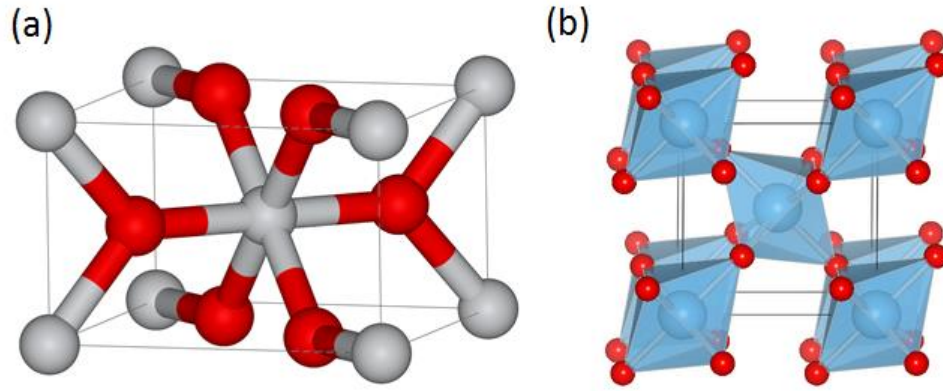

Figure 3.1. The Rutile β-PbO_2 unit cell (a) [9] and arrangement of polyhedra (b) [5]

Because Pb^{4+} is relatively unstable as compared with Pb^{2+} [1], the most common lead oxides are comprised of either Pb^{2+} only (PbO), or a combination of the two oxidation states. There are many such intermediate oxides (Figure 3.2), the most stable of which is Pb_3O_4 ($PbO_{1.33}$). Known as red lead or minimum, this compound is tetragonal ($P4_2/mbc$) at ambient conditions, with a = 8.80 Å, c = 6.56 Å [8]. The structure exhibits PbO_6 octahedra that share opposite edges and form chains along the c-axis [10], similar to β-PbO_2, but are linked by Pb^{2+} in a 3-fold pyramid coordination [1] (Figure 3.3a). Two orthorhombic structures are formed at high pressure, reached at approximately 0.2 GPa and 5.1 GPa, respectively. Both structures are orthorhombic (*Pbam*) with a = 9.38, b = 6.46, c = 6.64, Z = 2, but the higher pressure variant has a halved c-dimension [10]. Pb_3O_4 is usually reported to be a nonstoichiometric oxide, though data shows homogeneity within the range $PbO_{1.31-1.33}$ [8].
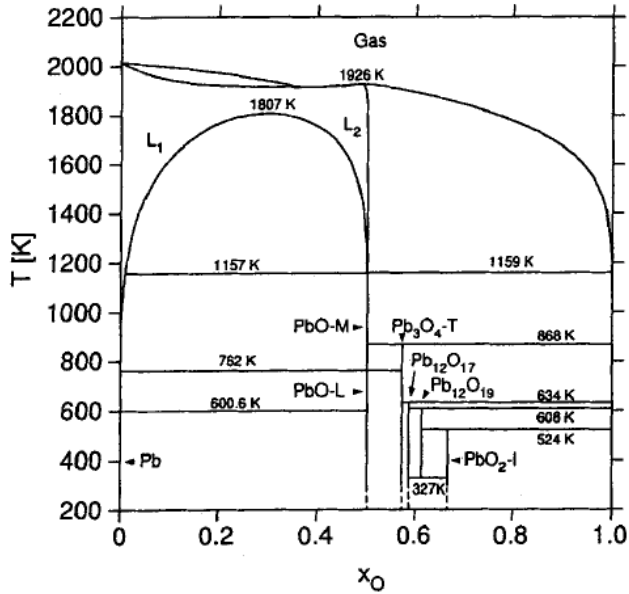
Figure 3.2. Phase diagram of the Pb-O system at 1 bar [11].

Another intermediate oxide, Pb_2O_3 ($PbO_{1.5}$), is rare and formed by decomposition of PbO_2 at 580°C - 620°C under oxygen pressure over 100 MPa [2]. The structure is monoclinic ($P12_1/a1$), with a = 7.00 Å, b = 5.63 Å, c = 3.91 Å, β = 82° 19', and in this case, Pb^{2+} atoms are between layers of distorted PbO_6 octahedra [1]. $Pb_{12}O_{19}$ ($PbO_{1.58}$) is monoclinic (a = 5.496 Å, b = 5.424 Å, c = 5.392 Å, β = 89.5°) [12] but also considered to have a pseudo-cubic defect-fluorite structure with 10 ordered O vacancies, $Pb_{24}O_{38}(vac)_{10}$, and no detectible variability in composition [1]. Another intermediate oxide is $Pb_{12}O_{17}$ ($PbO_{1.42}$), which normally has a stoichiometric ordered defect-fluorite structure ($Pb_{24}O_{34}(vac)_{14}$), though randomly disordered O vacancies lead to compositions from $PbO_{1.42}$ to $PbO_{1.57}$ during oxidation [13].

The most stable oxide of lead is PbO, which under ambient conditions is tetragonal ($P4_2/mbc$) with a = b = 3.98 Å, c = 5.02 Å [8]. This structure is layered (Figure 3.3b), in which stacked oxide planes are held together by Pb-Pb interaction, leading to symmetric Pb-O bond lengths [8]. An orthorhombic structure ($Pbcm$) forms in ambient pressure at 540°C, or in ambient temperature at 2.5 GPa [14]. This structure (with a = 5.49 Å, b = 4.76 Å, c = 5.90 Å) is essentially a distorted version of the tetragonal structure [1] with unequal Pb-O distances, becoming metastable at room temperature after fast quenching [8]. Most of the aforementioned stoichiometries can be created by decomposing PbO_2 at high temperatures in air as follows: PbO_2 -> $Pb_{12}O_{19}$ (293°C) -> $Pb_{12}O_{17}$ (351°C) -> Pb_3O_4 (374°C) -> PbO (605°C) [12].

Note that the final product is PbO, as this is the most stable form, and that Pb_2O_3 is not formed under these conditions. Products with other stoichiometries have been reported but will not be discussed.
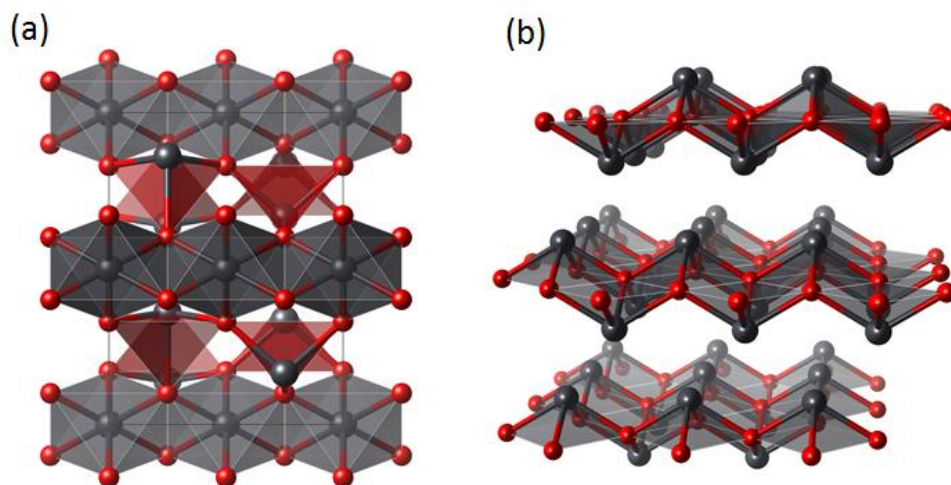
Figure 3.3. Pb_3O_4 structure, showing $Pb^{4+}O_6$ octahedra linked by $Pb^{2+}O_3$ units (a) [15], and the *t*-PbO structure comprised of stacked layers [16].

3.2. Experimental Methods

Lead(IV) oxide powder was obtained from Alfa Aesar with a theoretical density of 9.38 g/cm^3. Sample holders were made by drilling sets of 130 μm diameter holes, into 12.5 μm thick steel foils, using electron discharge machining. The powder was then pressed into these holes using a hydraulic press with a pressure of 20 MPa. This formed sets of cylindrical sample pellets held within the foils, each approximately 130 μm in diameter and 12.5 μm thick. Each set contained seven samples for redundancy, in the event that pellets were lost from the foils during transportation, irradiation, or characterization. Details of this sample preparation method can be found in Ref. [17]. Ten sets of samples were prepared and irradiated with 2.2 GeV [197]Au ions (11.1 MeV/u) at room temperature, using the UNILAC linear accelerator at the GSI Helmholtz Centre for Heavy Ion Research, in Darmstadt, Germany. Each set was irradiated to a different fluence, increasing from 5×10^{10} to 1×10^{13} ions/cm^2. The flux was kept sufficiently low to avoid sample heating during irradiation, which was on average 4×10^9 ions/cm^2·s. The

projected ion range was calculated using SRIM code [18], indicating a range of 55.4 µm (with a straggle of 1.18 µm) based on the material's theoretical density. Thus, it is evident that ions pass completely through the sample thickness and are not imbedded within the sample. The electronic stopping power, dE/dx, was determined to have an approximately constant profile through the sample thickness, with an average value of 46.3 ± 1.0 keV/nm.

Post-irradiation analysis included synchrotron-XRD with high energy X-rays (λ = 0.496 Å) at the Advanced Photon Source (APS), Argonne National Laboratory. Data were collected from several sample pellets irradiated to each fluence level, including unirradiated samples. The measurements were performed in transmission mode using a MAR345 image plate, with an X-ray spot size of 4.5 × 12 µm (at FWHM), and an exposure time of 120 s. The diffraction images were integrated with Fit2D software [19]. The unirradiated sample diffraction patterns were then quantitatively analyzed using Rietveld refinement conducted with FullProf software [20], in order to characterize the initial structure. This was not possible for any higher fluence samples due to the complexity of each profile (Section 3.1). Raman measurements were performed in backscattering geometry with a red-orange solid state laser (λ = 633 nm) and 20x microscope objective. The laser power was limited to 0.64 mW to avoid thermal effects during the 30 s exposures. Several measurements were taken on samples irradiated to all fluences. Samples at various fluences were then dispersed onto TEM grids for characterization. Imaging and selected area diffraction were completed using an FEI Tecnai G2 F20 X-TWIN TEM with the field emission gun operated at 200 keV. XPS data were acquired using a Kratos Axis Ultra XPS, before and after surface cleaning with an Ar^+ beam, and analysis was completed with CasaXPS software [21].

3.3. Results & Discussion

There are a number of different stoichiometries and structures for the Pb-oxides: tetragonal PbO_2 and PbO (t-PbO_2 and t-PbO), orthorhombic PbO_2 and PbO (o-PbO_2 and o-PbO), monoclinic Pb_2O_3 (m-Pb_2O_3), orthorhombic Pb_3O_4 (o-Pb_3O_4), and cubic Pb (c-Pb).

3.3.1. Synchrotron X-ray diffraction

The unirradiated material contains both polymorphs of PbO_2; Rietveld refinement was used to identify and quantify the proportion of these two structures. Along with the ambient t-PbO_2 structure, approximately 12.0 ± 0.6 % of the material was in the high pressure, o-PbO_2 phase. These structures are labeled A and B in Figure 4, respectively. At a fluence of 3×10^{11} ions/cm^2, the diffraction profile changes significantly with the addition of several new structures and a diffuse amorphous background. Diffraction maxima from m-Pb_2O_3 emerge, marked C in Figure 4. Due to peak overlap, the additional maxima are difficult to assign, but there is a likely some combination of t-PbO, o-PbO, or o-Pb_3O_4 structures in the sample (D, E, and F in Figure 4, respectively). At 8×10^{11} ions/cm^2, there is no longer evidence of the o-PbO_2 structure, and the t-PbO_2 is very low in intensity. At this fluence, the amorphous phase has reached its maximum intensity (relative to crystalline maxima), and gradually decreases as fluence is further increased. Peak overlap in the 8° to 10.5° range also becomes severe at this fluence.
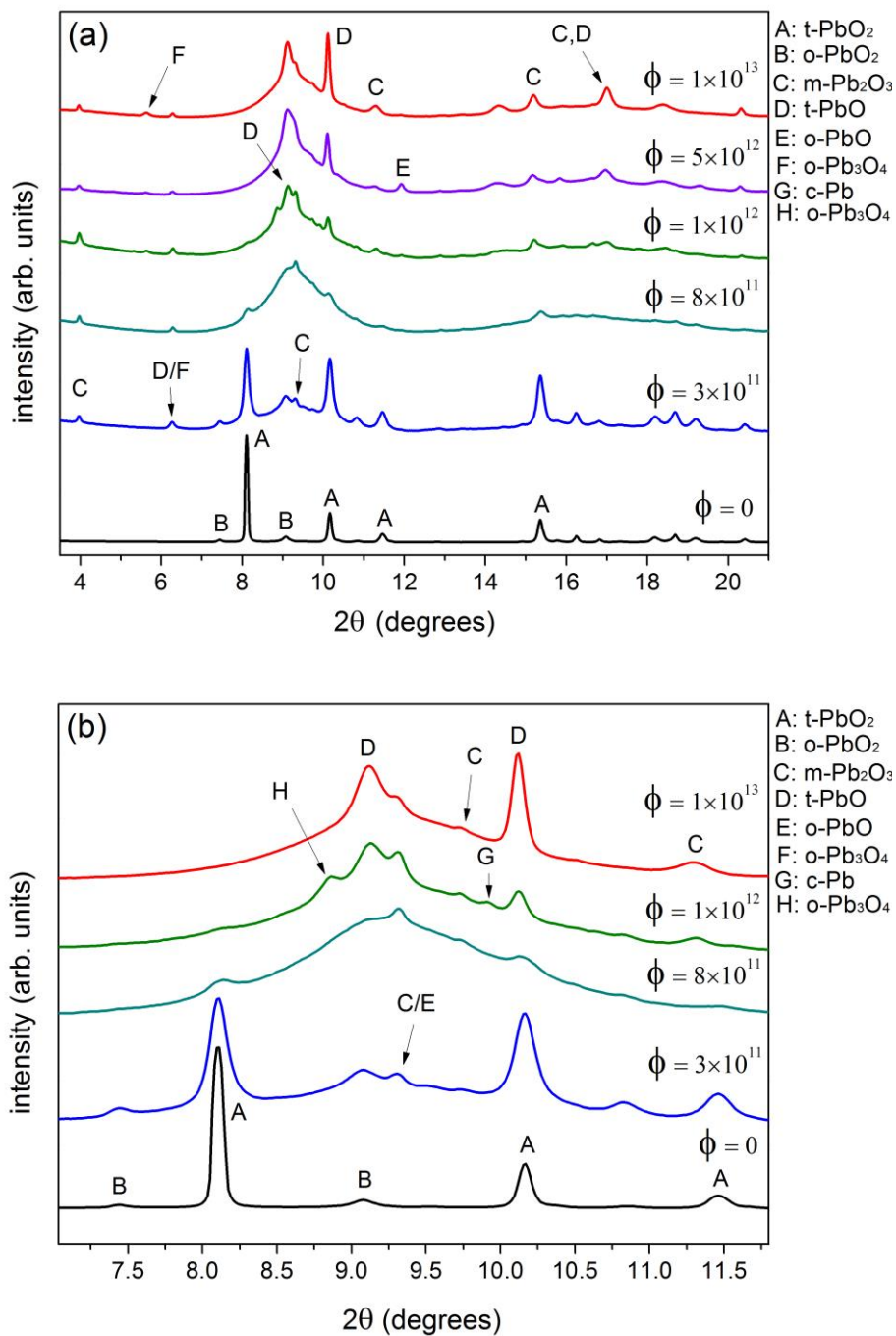
Figure 3.4. Representative synchrotron-XRD patterns for a range of fluences (ions/cm^2). Profiles in (a) show the growth of new peaks and the amorphous background induced by irradiation. A more narrow range of angles (b) shows a detailed view of the emerging diffraction maxima. A: t-PbO$_2$, B: o-PbO$_2$, C: m-Pb$_2$O$_3$, D: t-PbO, E: o-PbO, F: o-Pb$_3$O$_4$, H: t-Pb$_3$O$_4$, G: c-Pb. Peaks labeled D/F and C/E are attributed to one of the two possible phases, and those marked C,D are attributed to peak overlap from both phases.

At 1×10^{12} ions/cm^2, several new diffraction maxima become evident, including those related to the t-PbO, o-Pb$_3$O$_4$, t-Pb$_3$O$_4$, o-PbO, and c-Pb structures. Note that o-Pb$_3$O$_4$ and o-PbO are high-pressure/high-temperature variants. Samples irradiated to this fluence contain only trace quantities of t-PbO$_2$, and o-PbO. Figure 5 shows the high level of peak overlap at 1×10^{12} ions/cm^2, which prevented refinement of these phases. At 5×10^{12} ions/cm^2, a mixture of m-Pb$_2$O$_3$, t-PbO, o-PbO, o-Pb$_3$O$_4$, and amorphous phases exist. There is a significant increase in the o-PbO peak intensities at this fluence. At 1×10^{13} ions/cm^2, all phases present in the 5×10^{12} ions/cm^2 samples exist, but only trace quantities of o-PbO. The relative intensity of the amorphous background has decreased back to a level comparable to its initial formation at 3×10^{11} ions/cm^2. Table 1 summarizes the phases present at each fluence, and corresponding stoichiometry.

Table 3.1. Phases present as a function of fluence (ion/cm^2)

|	$\Phi = 0$	5×10^{10}	3×10^{11}	5×10^{11}	8×10^{11}	1×10^{12}	3×10^{12}	5×10^{12}	8×10^{12}	1×10^{13}	x in PbO$_x$
t-PbO$_2$	yes	yes	yes	yes	yes	trace	no	no	no	no	2
o-PbO2	yes	yes	yes	trace	no	no	no	no	no	no	2
amorph.	no	no	yes	yes	yes	yes	yes	yes	yes	yes	unknown
m-Pb$_2$O$_3$	no	no	yes	yes	yes	yes	yes	yes	yes	yes	1.5
o-Pb$_3$O$_4$	no	no	possible	possible	possible	yes	yes	possible	yes	yes	1.33
t-Pb$_3$O$_4$	no	no	no	no	possible	yes	yes	possible	no	no	1.33
t-PbO	no	no	possible	possible	trace	yes	yes	yes	yes	yes	1
o-PbO	no	no	possible	possible	trace	yes	yes	yes	yes	trace	1
c-Pb	no	no	no	no	no	yes	possible	trace	possible	possible	0
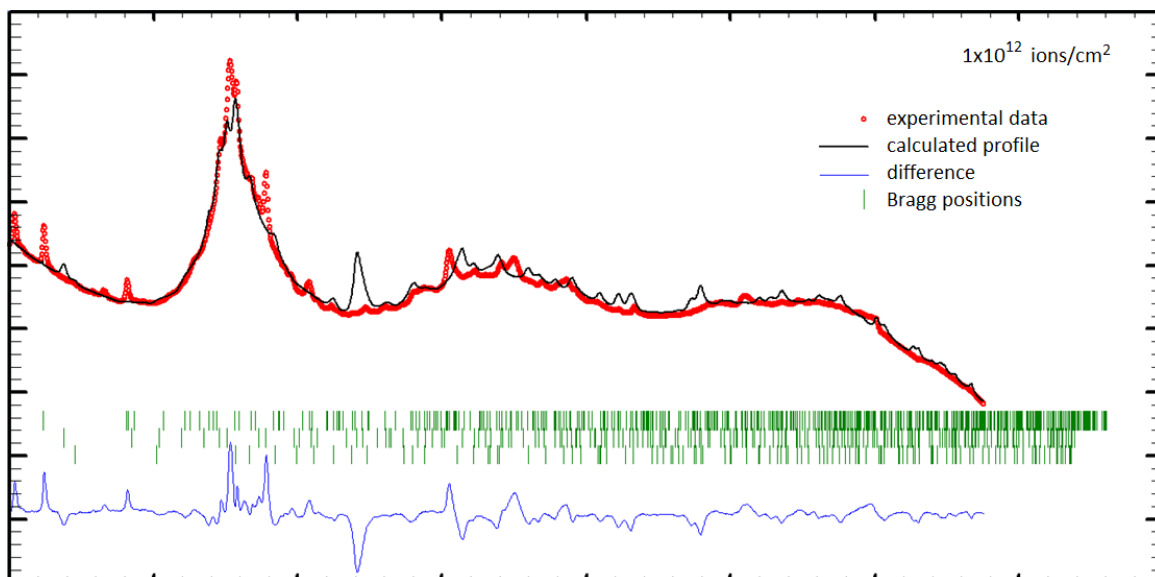
Figure 3.5. Rietveld refinement of the 1×10^{12} ions/cm^2 profile, showing the difficulty of obtaining a good fit due to peak overlap. Experimental data is shown in red, the refinement model in black, their difference in blue, and the calculated positions of diffraction maxima in green.

The stoichiometry (represented by the "x" parameter in Table 1) is observed to decrease gradually as a function of fluence, suggesting an ion-induced loss of O and cation reduction to the Pb^{2+} state. These processes are likely associated with the relatively low bond dissociation energy of PbO$_2$ of 1.31 eV/atom [22], low enthalpy of formation of 0.96 eV/atom [11], and low cation electronegativity of 1.62 [23] in respect to many other metal-dioxides [23]. The increased concentration of Pb^{2+} ions destabilize the PbO$_2$ structure and promote the formation of the intermediate oxide and PbO structures. Structural changes are facilitated by the small rearrangements needed to transition and energetic favorability. For example, Figure 3.3a shows that the Pb$_3$O$_4$ structure is comprised of very similar Pb^{4+}O$_6$ octahedra as the initial rutile structure, but these are joined by Pb^{2+}O$_3$ triangular pyramid structures. Thus, polyhedral units are preserved to some extent during the formation to this structure, without major restructuring. The ease of transition is facilitated by the relatively higher enthalpy of formations for these oxides in comparison with PbO$_2$. Values for Pb$_3$O$_4$ and PbO are 1.09 eV/atom and 1.13 eV/atom, respectively, compared to that of PbO$_2$ which is 0.96 eV/atom.

3.3.2. Raman spectroscopy

67

The bands at approximately 515 cm^{-1} and 650 cm^{-1} in the unirradiated spectrum are associated with Raman-active modes in t-PbO$_2$ [24], and are labeled A in Figure 6. The shoulder at ~545 cm^{-1} may be associated with o-PbO$_2$ (561 cm^{-1}) [25] or trace quantities of o-Pb$_3$O$_4$ (548 cm^{-1}) [26,27], as it is a strong scatterer. The broad band from approximately 345 cm^{-1} to 445 cm^{-1} is likely a superposition of bands from t-PbO$_2$ (424 cm^{-1}) [24], o-PbO$_2$ (352 cm^{-1}[25] or 360 cm^{-1} [28]) and trace quantities of o-Pb$_3$O$_4$ (340 cm^{-1} [29] and 391 cm^{-1} [24]). The o-Pb$_3$O$_4$ is probably on the sample face only due to surface reduction, as its periodic structure is not observed in the XRD profile. Note that Raman spectra from o-PbO$_2$ are essentially absent from the literature; the values taken from Ref. [28] were not confirmed with XRD, and those from Ref. [25] were calculated using the primitive unit cell.
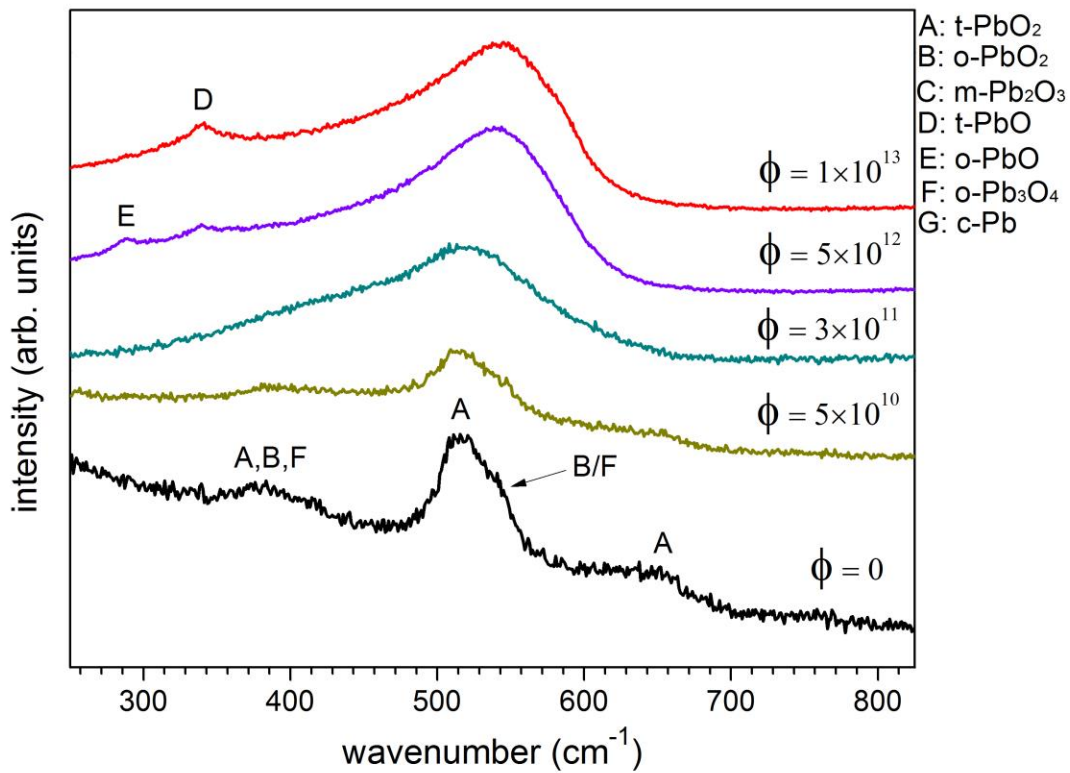

Figure 3.6. Representative Raman spectra for a range of fluences (in units of ions/cm^2).

A significant change in the spectra is seen at 3×10^{11} ions/cm^2, where the t-PbO$_2$ band at 515 cm^{-1} has apparently broadened significantly with a maximum at 532 cm^{-1}. This may be associated with the amorphous phase, though no data on amorphous PbO$_2$ or intermediate oxides exist in the literature, or an increase in o-Pb$_3$O$_4$ (at 550 cm^{-1}) [24,27]. As fluence is further increased, this broad band appears to shift to higher wavenumbers. At 5×10^{12} ions/cm^2, bands at approximately 289 cm^{-1} and 336 cm^{-1} appear, which correspond to o-PbO [26,27,29] and t-PbO [24,26,30], respectively. At the highest fluence of 1×10^{13} ions/cm^2, the broad band has shifted to 546 cm^{-1}, likely a result of overlapping bands from the amorphous material, o-Pb$_3$O$_4$ at 550 cm^{-1} [24,27], or other intermediate oxides. The band associated with t-PbO has increased in intensity at this fluence, in agreement with XRD data.

3.3.3. X-ray photoelectron spectroscopy

The unirradiated sample spectrum is shown in Figure 7. The 7/2 and 5/2 Pb 4f peaks are centered at 137.8 eV and 142.7 eV, respectively, in agreement with values in the literature for PbO$_2$ [3,31]. As fluence increases, these peaks appear to shift to higher binding energies, until reaching positions consistent with Pb in its 2+ valence state at 8×10^{11} ions/cm^2 [3,31], though there is likely still intensity contribution from PbO$_2$. This shift supports the observation in XRD and Raman data that intermediate oxides and PbO were formed during irradiation, and that the proportion of lead in its Pb^{2+} state increases as fluence increases (at the expense of Pb^{4+}). The shoulders on the PbO$_2$ peaks in the unirradiated profile (136.2 and 141.1 eV) increase in intensity with fluence, while their positions stay approximately constant. These positions are moderately consistent with metallic Pb, though its existence in the unirradiated material is improbable, and the peak intensities (relative to Pb^{4+} and Pb^{2+}) would suggest an unreasonable quantity. Thus, these peaks were not able to be assigned explicitly, but may be associated with nonstoichiometry and/or poorly crystallized material. The increase in intensity with fluence would therefore reflect an increase in disorder as a result of irradiation. A lower binding energy is expected for a defective structure, which may exist on the unirradiated sample face due to surface reduction (as suggested by the observation of Pb$_3$O$_4$ Raman bands). These peaks, however, are not associated with well crystallized Pb$_3$O$_4$ [32]. As PbO$_2$ is known to be

intrinsically substoichiometric [3,4,7], O vacancies near the sample surface, causing longer bond lengths and an increase in free energy, may lead the observed decrease in binding energy. These peaks may also be associated with intermediate lead oxides that have not been studied with XPS, for example Pb_2O_3, $Pb_{12}O_{19}$, $Pb_{12}O_{17}$, and/or the existence of the rare and unstable Pb^{3+} [33] or Pb^{1+} in Pb_2O. Another anomaly presents itself as two new peaks appear at 8×10^{11} ions/cm^2 (135.2 and 140.1 eV), also increasing in intensity with fluence. These may be associated with poorly crystallized metallic c-Pb. Although these two sets of peaks were not able to be assigned explicitly, their peak separations are consistent with Pb 4f.

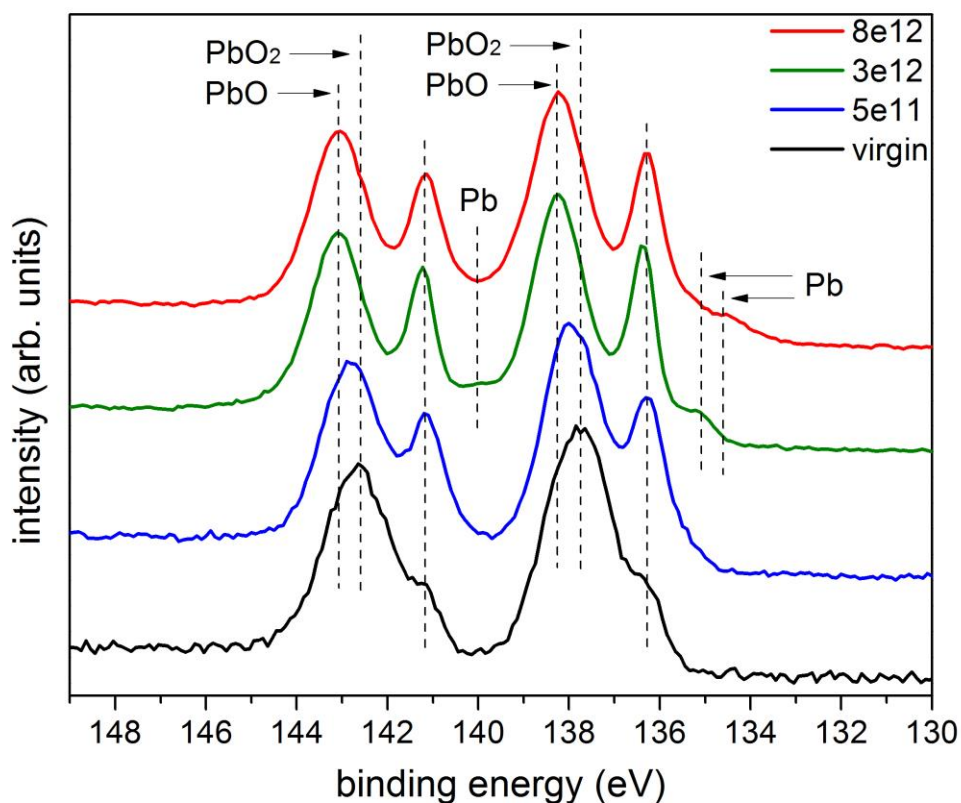Figure 3.7. Representative XPS spectra for unirradiated and irradiated samples. The PbO_2 peaks (relating to the Pb^{4+} state) gradually shift to higher binding energies, becoming consistent with formation of Pb^{2+} during irradiation.

70

3.4. Transmission electron microscopy

Ion tracks were not observed in irradiated PbO_2. An interesting effect of electron-beam induced bubble formation was observed during TEM analysis (Figure), reflecting the chemical instability of this material under charged-particle irradiation. These bubbles may be empty (voids) or may contain O_2 gas after the decomposition of PbO_2.

Figure 3.8. Electron-beam induced bubbles formed in PbO_2 sample during TEM analysis

3.4. Conclusion

Swift heavy ion irradiation of PbO_2 led to the formation of crystalline Pb_2O_3 (monoclinic), Pb_3O_4 (both tetragonal and orthorhombic), PbO (both tetragonal and orthorhombic), and Pb (cubic) structures, along with an amorphous phase of unknown composition. At a fluence of $3{\times}10^{11}$ ions/cm^2, the Pb_2O_3 structure and amorphous phase first become evident in the XRD profile, while the PbO_2 diffraction maxima decreased in intensity. The highest intensity Raman mode in PbO_2 significantly broadens at this fluence (with the other Raman bands becoming unobservable), and the Pb 4f photoelectron peaks shift to higher binding energies (consistent

with reduction to Pb^{2+}). By a fluence of 1×10^{12} ions/cm^2, there are only trace quantities of PbO_2 evident in the XRD profile, and the material consist of Pb_2O_3, Pb_3O_4, PbO (both phases), and metallic Pb structures, along with the amorphous phase. As fluence further increases, XRD data show that the tetragonal PbO phase increases in proportion (relative to all others) and appears to become the dominant phase. The Pb 4f peaks continue to shift until their positions agree with the Pb^{2+} state at high fluences.

Many of the intermediate oxides of lead form under thermal decomposition [1]. The ion-induced phase transformations may be explained by the thermal-spike model [34], as the sharp increase in temperature may destabilize Pb-O bonds and promote the formation of the lower stoichiometric phases. However, Pb_2O_3 has not been reported to form under high thermal conditions, which is likely the first phase to form during ion irradiation. Furthermore, the transformation process is likely similar to that observed in the formation of SnO in irradiated SnO_2 (under the same irradiation conditions). The transition to SnO was attributed to a multi-impact mechanism and supports the importance of high defect concentrations [35]. The loss of oxygen was not measured directly in irradiated PbO_2, but indirect evidence was given as each new crystalline form was of a lower O concentration, and an increase in the proportion of the Pb^{2+} state was observed. These processes are supported by the intrinsically substoichiometric matrix and high anion conductivity [3,4,7], along with the relatively low bond dissociation energy [22]. The loss of oxygen and related cation reduction appear to control the radiation response of PbO_2.

Acknowledgements

References

[1] N.N. Greenwood, A. Earnshaw, Chemistry of the Elements pt.2, in: Chem. Elem., 1997: pp. 374–388.

[2] W.B. White, F. Dachille, R. Roy, High-Pressure--High-Temperature Polymorphism of the Oxides of Lead, J. Am. Ceram. Soc. 49 (1961).

[3] D.J. Payne, R.G. Egdell, D.S.L. Law, P. a Glans, T. Learmonth, K.E. Smith, et al., Experimental and theoretical study of the electronic structures of alpha-PbO and beta-PbO2, (2007) 267–277. doi:10.1039/b612323f.

[4] D.O. Scanlon, A.B. Kehoe, G.W. Watson, M.O. Jones, W.I.F. David, D.J. Payne, et al., Nature of the Band Gap and Origin of the Conductivity of PbO2 Revealed by Theory and Experiment, Phys. Rev. Lett. 107 (2011) 246402. doi:10.1103/PhysRevLett.107.246402.

[5] Harada, Crystal Data for B-PbO2, (1981) 0–1.

[6] J. Taggart, E. Foord, A. Rosenzweig, T. Hanson, SCRUTINYITE, NATURAL OCCURRENCES OF aPbO2 FROM BINGHAM , NEW MEXICO, U.S.A., AND MAPIMI, MEXICO, 26 (1988) 905–910.

[7] R. a. Evarestov, V. a. Veryazov, I.I. Tupitsyn, V.V. Afanasiev, The Electronic Structure of Crystalline Lead Oxides, J. Electron Spectros. Relat. Phenomena. 68 (1994) 555–563. doi:10.1016/0368-2048(94)80021-9.

[8] Pavlov, Chapter 5: Leady Oxide, in: Lead-Acid Batter. Sci. Technol., 2011. doi:10.1016/B978-0-444-52882-7.10005-9.

[9]   a. a. Bolzan, C. Fong, B.J. Kennedy, C.J. Howard, Structural Studies of Rutile-Type Metal Dioxides, Acta Crystallogr. Sect. B Struct. Sci. 53 (1997) 373–380. doi:10.1107/S0108768197001468.

[10] Dinnebier, Bulk moduli and high-pressure crystal structures of minium, Pb 3 O 4 , determined by X-ray powder diffraction, Am. Mineral. 88 (2003) 996–1002.

[11] D. Risold, J.-I. Nagata, R.O. Suzuki, Thermodynamic description of the Pb-O system, J. Phase Equilibria. 19 (1998) 213–233. doi:10.1361/105497198770342238.

[12] W.B. White, R. Roy, Phase Relations in the System Lead-Oxygen, J. Inorg. Nucl. Chem. 18 (1964) 143–147. doi:10.1016/0022-1902(61)80381-3.

[13] J.S. Anderson, M. Sterns, The Intermediate Oxides of Lead, J. Electrochem. Soc. 106 (1959) 369. doi:10.1149/1.2427362.

[14]   D.M. Adams, A.G. Christy, J. Haines, S.M. Clark, Second-order phase transition in PbO and SnO at high pressure: Implications for the litharge-massicot phase transformation David, 46 (1992) 358–367.

[15]   S.T. Gross, The crystal structure of Pb3O4, J. Am. Chem. Soc. 65 (1943) 1107–1110.

[16]   J. Leciejewicz, On the crystal structure of tetragonal (red) PbO, Acta Crystallogr. 14 (1961) 1304–1304. doi:10.1107/S0365110X61003892.

[17]   M. Lang, C.L. Tracy, R.I. Palomares, F. Zhang, D. Severin, M. Bender, et al., Characterization of Ion-Induced Radiation Effects in Nuclear Materials using Synchrotron X-ray Techniques, 2014.

[18]   J.F. Ziegler, M.D. Ziegler, J.P. Biersack, SRIM – The stopping and range of ions in matter (2010), Nucl. Instruments Methods Phys. Res. Sect. B Beam Interact. with Mater. Atoms. 268 (2010) 1818–1823. doi:10.1016/j.nimb.2010.02.091.

[19]   A.P. Hammersley, S.O. Svensson, M. Hanfland, A.N. Fitch, D. Häusermann, FIT2D, (2005).

[20]   J. Rodriguez-Carvajal, FULLPROF Suite, (2011).

[21]   N. Fairley, C.S. Ltd, CasaXPS Manual 2.3.15: CasaXPX Processing Software for XPS Spectra, Casa Software Limited, 2009. https://books.google.com/books?id=wCU8MwEACAAJ.

[22]   T.L. Cottrell, The Strengths of Chemical Bonds, 2nd Ed., Butterworth, London, 1966.

[23]   M. Lenglet, Iono-Covalent Character of the Metal–Oxygen Bonds in Oxides: A Comparison of Experimental and Theoretical Data, Act. Passiv. Electron. Components. 27 (2004) 1–60. doi:10.1080/0882751031000116142.

[24]   L. Burgio, R.J.H. Clark, S. Firth, Raman spectroscopy as a means for the identification of plattnerite (PbO2), of lead pigments and of their degradation products, Analyst. 126 (2001) 222–227. doi:10.1039/b008302j.

[25]   R. Caracas, E. Bobocioiu, The WURM project - A freely available web-based repository of computed physical data for minerals, Am. Mineral. 96 (2011) 437–443. doi:10.2138/am.2011.3532.

[26]   M. San Andres, J.M. De la Roja, S.D. Dornheim, Litharge and massicot: Thermal decomposition synthetic route for basic lead(II) carbonate and Raman spectrocopy analysis, Lasers Conserv. Artworks Proc. Int. Conf. (2008).

[27] K.R. Bullock, Electrochemical and spectroscopic methods of characterizing lead corrosion films, J. Electroanal. Chem. Interfacial Electrochem. 222 (1987) 347–366. doi:10.1016/0022-0728(87)80299-1.

[28] Scrutinyite, RRUFF Proj. (n.d.). www.rruff.info.

[29] I.M. Bell, R.J. Clark, P.J. Gibbs, Raman spectroscopic library of natural and synthetic pigments (pre- approximately 1850 AD)., Spectrochim. Acta. A. Mol. Biomol. Spectrosc. 53A (1997) 2159–2179. doi:10.1016/S1386-1425(97)00140-6.

[30] S. Venkataraj, J. Geurts, H. Weis, O. Kappertz, W.K. Njoroge, R. Jayavel, et al., Structural and optical properties of thin lead oxide films produced by reactive direct current magnetron sputtering, J. Vac. Sci. Technol. A Vacuum, Surfaces, Film. 19 (2001) 2870. doi:10.1116/1.1410948.

[31] J.F. Moulder, W.F. Stickle, P.E. Sobol, K.D. Bomben, Handbook of X-ray Photoelectron Spectroscopy, (1995) 9–261.

[32] J.M. Thomas, M.J. Tricker, Electronic Structure of the Oxides of Lead, J. Chem. Soc. Faraday Trans. 71 (1974) 313.

[33] H. Liu, A.M. Kuznetsov, A.N. Masliy, J.F. Ferguson, G. V. Korshin, Formation of Pb(III) intermediates in the electrochemically controlled Pb(II)/PbO 2 system, Environ. Sci. Technol. 46 (2012) 1430–1438. doi:10.1021/es203084n.

[34] M. Toulemonde, J.M. Costantini, C. Dufour, A. Meftah, E. Paumier, F. Studer, Track creation in SiO2 and BaFe12O19 by swift heavy ions: a thermal spike description, Nucl. Instruments Methods Phys. Res. Sect. B Beam Interact. with Mater. Atoms. 116 (1996) 37–42.

[35] A.B. Cusick, M. Lang, F. Zhang, J. Zhang, C. Trautmann, R.C. Ewing, Phase transformation and chemical decomposition of nanocrystalline SnO2 under heavy ion irradiation, 2015.

Amorphization of Ta_2O_5 under swift heavy ion irradiation

Alex B. Cusick[a], Maik Lang[b], Fuxiang Zhang[c], Kai Sun[a], Weixing Li[d], Patrick Kluth[e], Christina Trautmann[fg] and Rodney C. Ewing[acd]

[a]Materials Science & Engineering, University of Michigan, Ann Arbor, MI 48109, USA

[b]Nuclear Engineering, University of Tennessee, Knoxville, TN 37996, USA

[c]Earth & Environmental Sciences, University of Michigan, Ann Arbor, MI 48109, USA

[d]Geological Sciences, Stanford University, Stanford, CA 94305, USA

[e]Research School of Physics and Engineering, Australian National University, Canberra ACT 2601, Australia

[f]GSI Helmholtz Centre for Heavy Ion Research, D-64291 Darmstadt, Germany

[g]Technische Universität Darmstadt, 64287 Darmstadt, Germany

Abstract

Crystalline Ta_2O_5 powder is shown to amorphize under 2.2 GeV [197]Au ion irradiation. Synchrotron X-ray diffraction (XRD), Raman spectroscopy, small-angle X-ray scattering (SAXS), and transmission electron microscopy (TEM) were used to characterize the structural transition from crystalline to fully-amorphous. Based on Rietveld refinement of XRD data, the initial structure is orthorhombic (*P2mm*) with a very large unit cell (a = 6.20, b = 40.29, c = 3.89 Å; V = 971.7 Å^3), ideally containing 22 tantalum and 55 oxygen atoms. At a fluence of approximately 3.0×10^{11} ions/cm^2, a diffuse amorphous background becomes evident in the XRD profile, increasing in intensity relative to diffraction maxima until full amorphization is achieved at approximately 3.0×10^{12} ions/cm^2. An anisotropic distortion of the orthorhombic structure

occurred during the amorphization process, with an approximately constant unit cell volume. The amorphous phase fraction as a function of fluence was determined, yielding a trend that is consistent with a direct-impact model for amorphization. SAXS and TEM data indicate that ion tracks exhibit a core-shell morphology. Raman data show that the amorphous phase is comprised of TaO_6 and TaO_5 coordination-polyhedra in contrast with the TaO_6 and TaO_7 units that exist in crystalline Ta_2O_5. Analysis of Raman data shows that oxygen-deficiency increases with fluence, indicating a removal of oxygen that leads to an estimated final stoichiometry of $Ta_2O_{4.2}$ at a fluence of 1.0×10^{13} ions/cm^2.

Keywords: swift heavy ions; irradiation; phase transformation; tantalum oxide; amorphization;

4.1. Introduction

Ta_2O_5 is a complex and versatile material that has many applications in materials engineering. One of the most notable characteristics of Ta_2O_5 is its high dielectric constant (relative permittivity) [1–11], which has an unusually high value in the range of 25 to 100 depending on processing factors, such as synthesis methodology and annealing temperature [1]. Although the crystalline state has a higher absolute value on average (ranging from 56 - 59) [12], it is highly anisotropic. Therefore, the amorphous form is often used in microelectronics in order to avoid this effect [7]. The amorphous form also exhibits improved leakage current properties due to the decreased loss at grain boundaries [13]. The high dielectric constant, high dielectric breakdown strength [2], and good leakage current properties [2,14] make Ta_2O_5 a useful material for gate dielectrics in transistors [1,6], dielectric resonators in microwave communication devices [1], and charge capacitors in dynamic RAM devices [5]. Due to these properties, Ta_2O_5 is also regarded as one of the best candidate materials to replace conventional SiO_2 and Si_3N_4 thin-film circuit devices [12]. This is because Si containing materials have reached their physical limit for size reduction [12] and use of Ta_2O_5 will allow the down-scaling that future microelectronic devices will rely on [4].

Tantalum pentoxide is also widely used due to its optical properties, typically in the amorphous state, in order to avoid scattering loss at grain boundaries [7]. Ta_2O_5 is commonly

used as a coating on solar cells due to its high refractive index, forming a low loss, anti-reflective layer that increases cell efficiency [1,5,7,8,15]. Ta_2O_5 is used in optical waveguides [6], electroluminescent displays [6], and also as a photocatalyst [8,15,16]. In addition, it is utilized as a chemical catalyst [7], gas sensor [5,15], proton conductor [7], and in surface acoustic wave devices [6]. As the structure highly affects its usefulness, the crystalline-to-amorphous transition is of great interest.

The structures of various polymorphs are not well defined for Ta_2O_5, largely due to the complexity of their crystallization behavior. There are two common ambient pressure structures, the low temperature L-Ta_2O_5 (or β-Ta_2O_5) phase and high temperature H-Ta_2O_5 (or α-Ta_2O_5) phase. L-Ta_2O_5 is generally considered to be orthorhombic [17–20], comprised of corner- and edge-sharing TaO_6 octahedra and TaO_7 pentagonal bipyramids [21]. A monoclinic model has also been proposed [17]. Although many unit cell parameters have been reported, the value of the longest parameter varies greatly, ranging from approximately 3.66 Å [22] to over 69.55 Å [17] in order to obtain cell symmetry. One of the most widely accepted models, given by Stephenson & Roth [20], is orthorhombic (*P2mm*) with dimensions: a = 6.20, b = 40.29, c = 3.89 Å. This model contains 11 formula units and relies on several O-vacancies and/or Ta-interstitials for charge neutrality; a representation of this structure is shown in Figure 4.1.

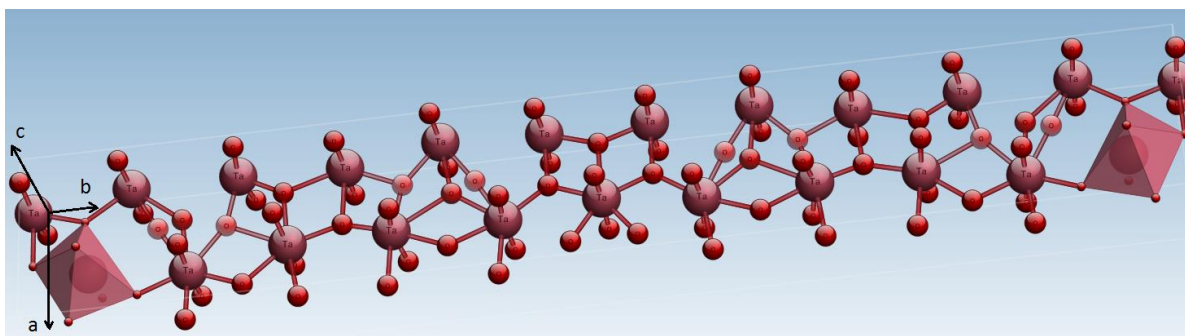Figure 4.1. Orthorhombic structure model proposed by Stephenson & Roth [20], comprised of TaO_6 and TaO_7 polyhedra.

A hexagonal structure, δ-Ta_2O_5 [23,24], has also been reported and is thought to be stable at ambient conditions with L-Ta_2O_5. This phase has been shown to have tantalum coordination numbers of both 6 and 8 [25], which has been confirmed by computational simulations of the

structure [26]. Transformation of δ-Ta_2O_5 into an orthorhombic structure was found to occur upon heating to 900°C [23]. At temperatures above ~1340°C [5,19] L-Ta_2O_5 transforms to H-Ta_2O_5. This structure is often considered to be orthorhombic [27,28], though it apparently has several variants including tetragonal [22,28,29], monoclinic [1,21,22,30], and triclinic [22]. Because the transformation from H-Ta_2O_5 is slow, and cooling of H-Ta_2O_5 has been shown to form several intermediate phases [19], it is difficult to prepare high quality L-Ta_2O_5 crystals by conventional high-temperature methods.

Two main high-pressure phases have been reported, both with monoclinic structures. B-Ta_2O_5 is comprised of TaO_6 polyhedra only [31]; whereas, Z-Ta_2O_5 consists of TaO_7 polyhedra only [24,31]. These two structures are closely related, easily transforming from one to the other, and a mixture of the two structures has been shown to form at 8 GPa and 1197°C [31]. Another monoclinic phase has been shown to form at 297-347°C and 20 MPa, denoted ε-Ta_2O_5 [24], which is 6-coordinated and is likely equivalent to B-Ta_2O_5. This ε-Ta_2O_5 phase has been shown to irreversibly transform into L-Ta2O5 at 887°C [24]. Transformation from a monoclinic to trigonal structure has also been observed by very slow cooling from 1000°C [32]. Due to the complex structure of Ta_2O_5, it has been shown to accommodate high dopant concentrations without significant alteration to its structure [33].

Materials subjected to swift heavy ion irradiation undergo complex structural modifications at the nano-scale; the extent of modification is dependent on the material, as well as the ion species and energy. The effects on radiation-resistant materials consist of defect production and clustering, grain growth, fragmentation, swelling, and polygonization [34,35]. In materials with a higher susceptibility to damage accumulation, the effects include crystalline-to-crystalline phase transformations (often into high temperature or high pressure phases) [36–39], amorphization [2,37,40–44], and cation reduction with associated anion loss [45–49]. Because the properties of a material are so highly dependent on structure, nano-scale structure modifications using ion beams are of great interest.

Swift heavy ions are highly ionized heavy atoms accelerated to energies of over 1 MeV/nucleon (often in the GeV range). As the ions bombard a target material, their energy is deposited into the material's electronic subsystem, causing intense electronic excitation and

ionization as the ions slow. This energy deposition (dE/dx) is concentrated in a very small cylindrical volume along the ion's trajectory, resulting in an extremely high energy density. The subsequent transfer of energy to the atomic lattice induces a cylindrical damage zone, often termed an "ion track". Although there have been many models proposed to describe this phenomenon, there is no general consensus on the exact mechanism of formation. According to the thermal-spike model, energy from the electronic subsystem is transferred to atoms within the lattice through electron-phonon coupling, which results in a sharp increase in temperature throughout the ion track [50–53]. This high-temperature transient results in the melting or vaporization of material within this region, leaving behind a highly modified and defective structure (often amorphous) after rapid quenching to the bulk. This model also provides a framework for understanding the high-temperature and high-pressure phase formation during irradiation, as rapid kinetics may lead to crystallization of these structures during the transient. The Coulomb-explosion model provides an alternative model for track formation, and focuses on the massive charge separation caused by dense ionization, inducing strong electro-static forces that displace atoms from their sites [54–56]. Other models have been proposed, based on the decay of self-trapped excitons [57,58] and bond-weakening [59,60], but these are not discussed here.

Ion tracks are typically on the order of several nanometers in diameter and many microns in length. This geometry is unique to swift heavy ion effects. Due to the significance of Ta_2O_5 in engineering applications, nanoscale modifications to its structure may have significant technological implications. This paper describes the previously unobserved amorphization of crystalline Ta_2O_5 under swift heavy ion irradiation. Synchrotron-XRD data were obtained for detailed structural characterization over a wide fluence regime, Raman spectroscopy for details on short-range order modifications, along with SAXS and TEM analyses for ion track and grain morphology characterization.

4.2. Experimental Methods

Tantalum(V) oxide powder was obtained from MTI Corporation with a theoretical density of 8.2 g/cm^3 and particle sizes on the order of 5-10 μm. Sample holders were fabricated by drilling

sets of 130 μm diameter holes, using electron discharge machining, into 12.5 μm thick molybdenum foils. The powder was then pressed into these holes using a hydraulic press with a pressure of 20 MPa. This formed sets of cylindrical sample pellets held within the foils, each approximately 130 μm in diameter and 12.5 μm thick. Each set contained seven samples for redundancy, in the event that pellets were lost from the foils during transportation, irradiation, or characterization. Further detail of the sample preparation method can be found in Ref. [61].Ten sets of samples were prepared and irradiated with 2.2 GeV [197]Au ions (11.1 MeV/u) at room temperature, using the UNILAC linear accelerator at the GSI Helmholtz Centre for Heavy Ion Research, in Darmstadt, Germany. Each set was irradiated to a different fluence, increasing from 5×10^{10} to 1×10^{13} ions/cm^2. The flux was kept sufficiently low to avoid sample heating during irradiation, which was on average 4×10^9 ions/cm^2·s. SRIM code [62] simulations indicated a projected ion range of 57.9 μm (with a straggle of 1.13 μm) based on the material's theoretical density. Therefore, all incident ions passed completely through the sample thickness and are not implanted into the sample. The electronic stopping power, dE/dx, was determined to have an approximately constant profile through the sample thickness, with an average value of 43.5 ± 1.0 keV/nm.

Post-irradiation analysis included synchrotron XRD with high energy X-rays (λ = 0.496 Å) at the Advanced Photon Source (APS), Argonne National Laboratory. Data were collected from several sample pellets irradiated to each fluence level, including unirradiated samples. The measurements were performed in transmission mode using a MAR345 image plate, with an X-ray spot size of 4.5 × 12 μm (at FWHM) and an exposure time of 120 s. The diffraction images were integrated with Fit2D software [63]. The unirradiated sample diffraction patterns were then quantitatively analyzed using Rietveld refinement conducted with FullProf software [64], in order to characterize the initial structure. Deconvolution of each XRD profile, by manually fitting peaks with Pseudo-Voigt functions, allowed the quantitative separation of intensity contributions from diffraction maxima and amorphous backgrounds. Because the relative quantities of the crystalline and amorphous phases are proportional to the relative diffraction pattern area contribution, an "amorphous fraction" was determined for each fluence by calculating the area ratio of amorphous peaks *vs.* the total pattern area (the sum of amorphous

and crystalline peak areas). Peak positions were used to calculate the orthorhombic unit cell parameters as a function of fluence, using the UnitCell code [65].

Raman measurements were performed in backscattering geometry with a red-orange solid state laser (λ = 633 nm) and 20x microscope objective. The laser power was limited to 0.64 mW to avoid thermal effects during the 40 s exposures. Several measurements were taken on samples irradiated to all fluences, and analysis of this data was conducted using a deconvolution and peak-fitting procedure. Samples at various fluences were then dispersed onto holey carbon films supported by Cu grids for TEM characterization. Imaging and selected area diffraction were completed using an FEI Tecnai G2 F20 X-TWIN TEM with the field emission gun operated at 200 keV. SAXS data were gathered in transmission mode from samples irradiated to 5.0×10^{10} ion/cm^2 at the SAXS/WAXS beamline at the Australian Synchrotron, using 11 keV X-rays and a camera length of approximately 1600 mm. Spectra were collected using a Pilatus 1M detector and exposure times of 5 and 10 s. More details on SAXS measurements of ion tracks using this beamline can be found in Ref. [66,67].

4.3. Results

4.3.1. Synchrotron X-ray diffraction

The evolution of the diffraction patterns as a function of fluence is shown in Figure 4.2. The unirradiated profile was best fit with an orthorhombic structure model (*P2mm*), PDF#: 04-007-0695, published by Stephenson & Roth in 1971 [20]. Because this model fits the data very closely, the initial phase was considered to be pure with no contamination. Manual peak fitting was used to track the positions and widths of the crystalline phase diffraction maxima as the fluence was increased, as well as the amorphous background as it increased in intensity. The diffraction maxima broaden with increasing fluence due to the accumulation of defects and microstrain during irradiation. The maxima corresponding to (001), (1,11,0), and (1,11,1) shift to higher 2θ values with increasing fluence, whereas those corresponding to (0,13,0) and (211) shift to lower values. Therefore, the two doublets (centered around approximately 9.1° and 11.8°) appear to merge. These peak shifts were used to determine the change in unit cell

parameters with increasing fluence, using the UnitCell code; the results of which are shown in Figure 4.3. The unit cell undergoes an anisotropic distortion during irradiation, where the *a* parameter expands and *b* and *c* parameters contract. The *a* parameter changes by approximately 0.40%, the *b* parameter by 0.08%, and the *c* parameter by 0.29%. The unit cell volume remains approximately constant.
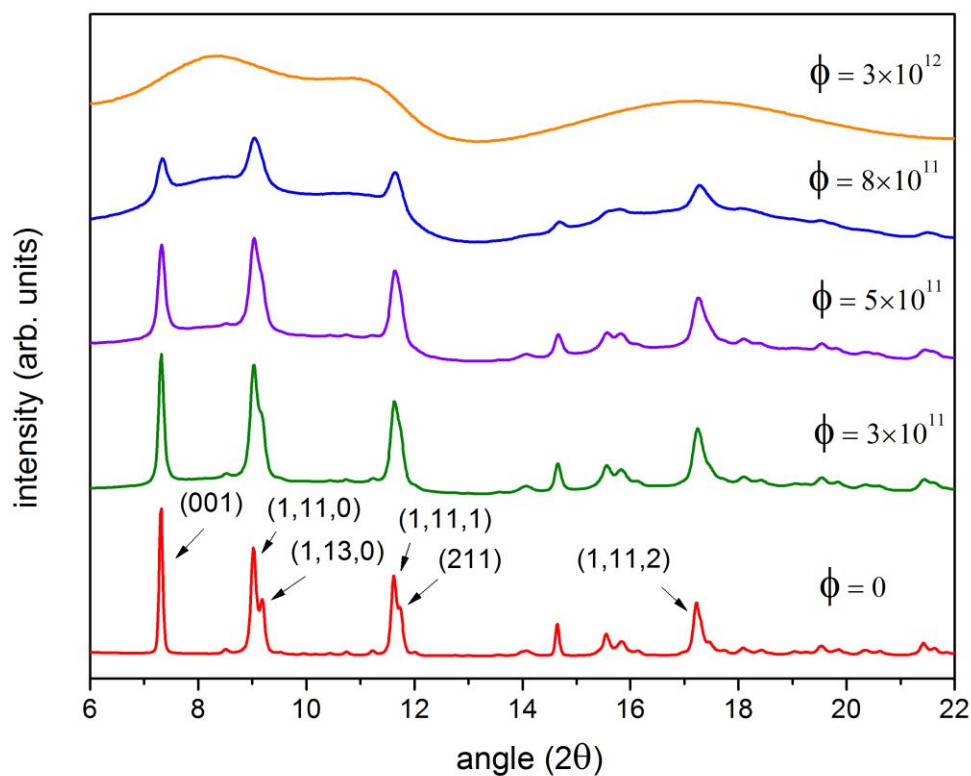
Figure 4.2. Synchrotron-XRD patterns of unirradiated and irradiated samples for a range of ion fluences, ϕ (in ions/cm^2). The peaks labeled on the unirradiated profile correspond to the most prominent diffraction maxima of orthorhombic L-Ta$_2$O$_5$.
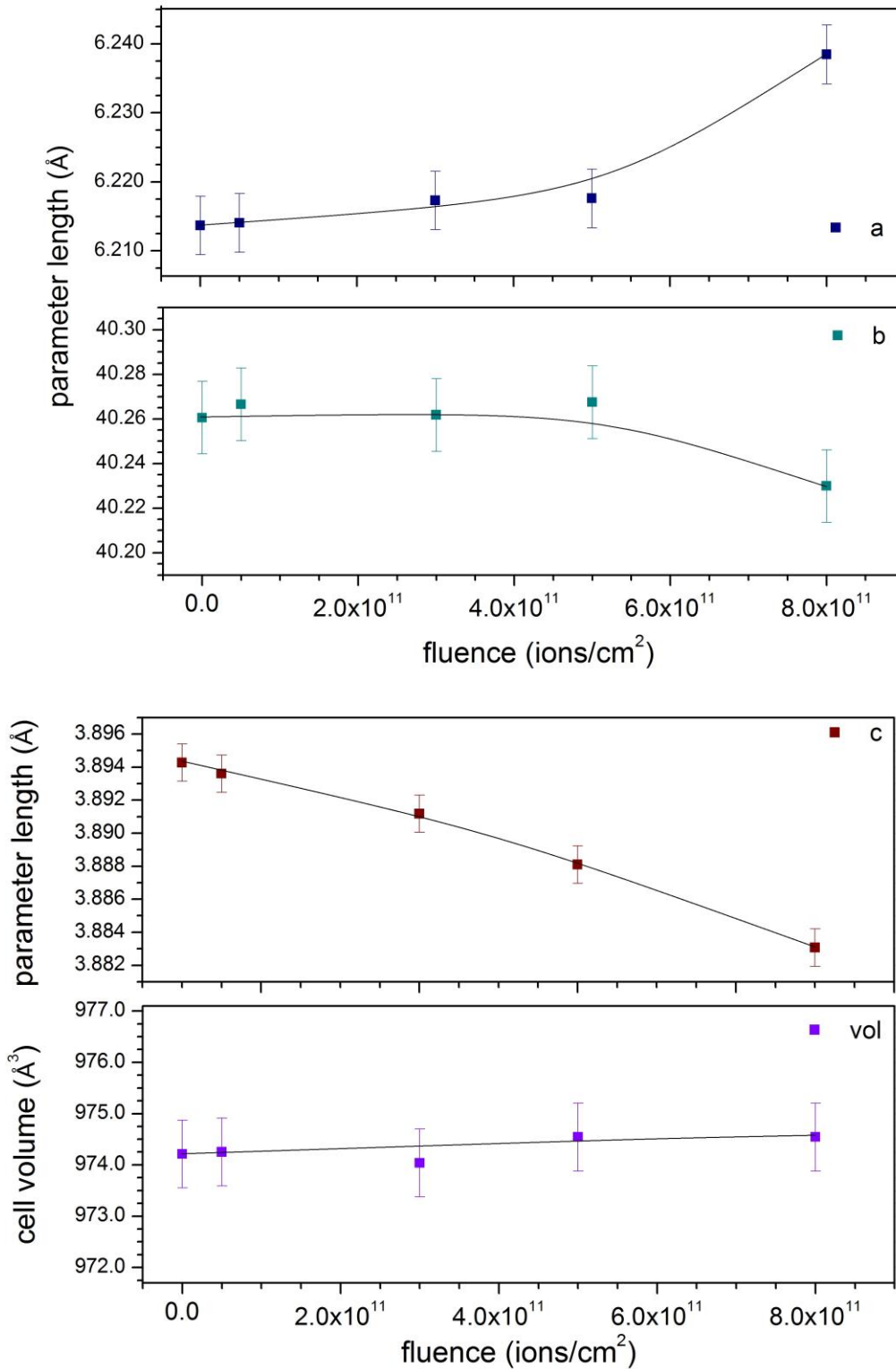
Figure 4.3. The evolution of unit cell parameters *a*, *b*, and *c*, along with the corresponding unit cell volume, as a function of ion fluence. Curves are shown only to guide the eye.

At a fluence of 3.0×10^{11} ions/cm^2, a diffuse amorphous background becomes evident in the XRD profile. As fluence increases, the intensity of this background increases with respect to the diffraction maxima. At 3.0×10^{12} ions/cm^2, crystalline peaks are no longer evident, indicating that the material has become fully-amorphous. The amorphous fraction as a function of fluence was determined after the deconvolution of each profile in order to separate the intensity contributions from the crystalline and amorphous phases. This fraction represents the proportion of amorphous material within the sample, and is shown in Figure 4.4. Errors were determined using the standard deviation of the five separate Pseudo-Vogt function fits used to calculate the average amorphous fractions. Four mathematical models were used to determine a best-fit to this data: direct-impact, double-overlap, direct-impact/cascade-overlap, and direct-impact/defect-stimulated models. These models and corresponding mechanisms are discussed in detail by Weber et al. [40].

Figure 4.4. The amorphous fraction as a function of fluence, with each of the four mathematical model fits.

The closest fit to the data is given by the simplest model, representing a direct-impact mechanism of amorphization, shown in Equation 1. The direct-impact mechanism is 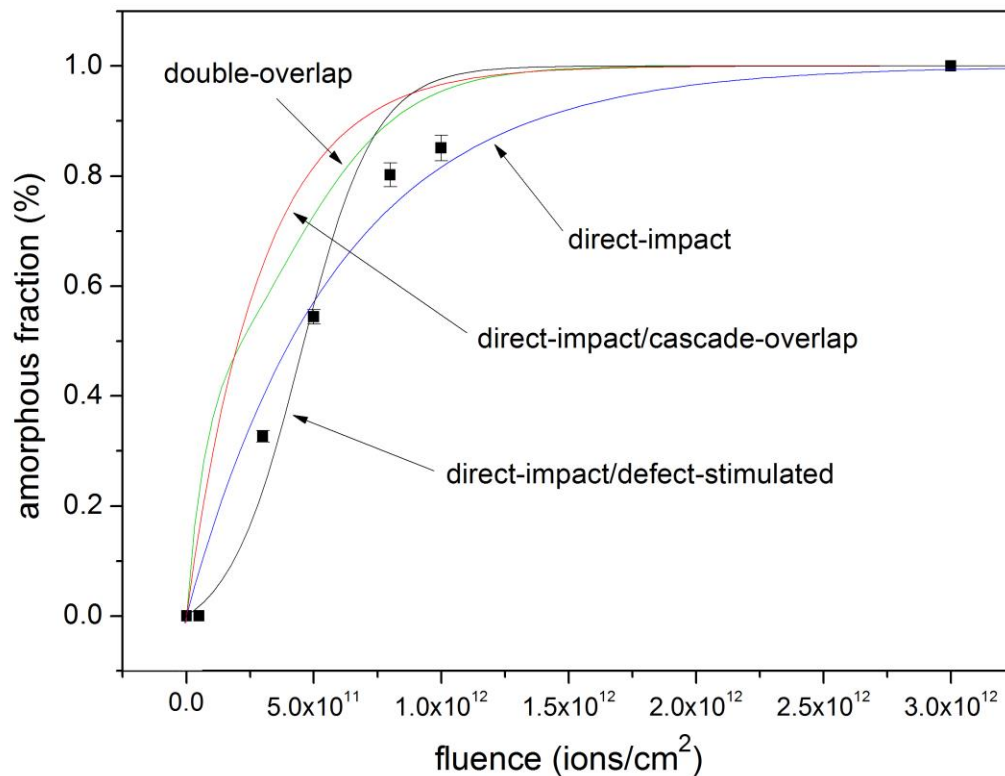associated with a heterogeneous amorphization, meaning that the phase originates from within each cylindrical ion track.

$$f_A = 1 - e^{-\sigma_a \phi} \tag{1}$$

In this model, the amorphous fraction, f_A, is represented in terms of the amorphization cross-section, σ_a, and ion fluence, ϕ. A fit to the data yielded σ_a = 1.695×10^{-12} cm^2 (169.5 nm^2), which gives an amorphous track diameter of 14.7 nm. This is unusually large, and reflects the material's high susceptibility to amorphization.

4.3.2. Raman Spectroscopy

The Raman spectrum for unirradiated Ta$_2$O$_5$ shows many Raman-active bands between 200 and 1000 cm^{-1}, consistent with previously published data [3,7,8,68,69]. This spectrum is shown in Figure 4.5, with bands labelled A through E. Peak A at 265 cm^{-1} has been attributed to inter-polyhedral Ta-O-Ta bending [3,69,70], and peak B at 498 cm^{-1} is associated with torsional motion within polyhedra [69]. Peaks labelled "C" correspond to symmetric Ta-O vibrations in TaO$_6$ polyhedra [3,69,71], and peak D, at approximately 845 cm^{-1}, has been ascribed to Raman-active modes in TaO$_7$ polyhedra within β-Ta$_2$O$_5$ [3]. Peak E is currently unassigned but appears to be due to secondary scattering. The determination that both TaO$_6$ and TaO$_7$ polyhedra are present in the unirradiated crystalline sample is consistent with the orthorhombic structure model used to fit the XRD data.
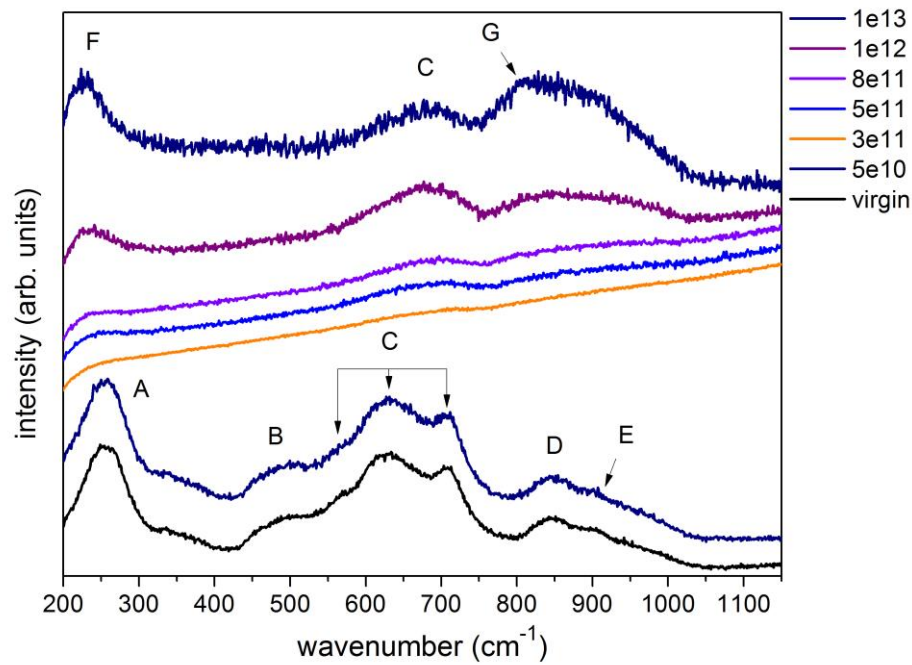
Figure 4.5. Raman spectra for a range of fluences up to 1×10^{13} ions/cm^2. Peaks labelled A through E correspond to Raman-active modes in crystalline Ta$_2$O$_5$, associated with TaO$_6$ and TaO$_7$ polyhedra. Peaks F and G correspond to TaO$_5$ polyhedra within the amorphous phase.

Little change is observed in the Raman spectra until 3.0×10^{11} ions/cm^2, at which point the Raman-active modes become overwhelmed by a high intensity background. This background appears to increase linearly with wavenumber, and reaches a maximum intensity of over six times that of all other profiles. This is due to enhanced photoluminescence (PL) emission, which has been attributed to high concentrations of O vacancies in crystalline Ta$_2$O$_5$ [72,73]. Very broad PL emission bands have been observed for O-deficient Ta$_2$O$_5$, centered around 695 or 705 nm depending on annealing temperature [72,73], which correspond to wavenumbers of 1409 and 1613 cm^{-1}. The Raman spectra are therefore showing only the left-hand portion of the broad luminescence peak that reaches a maximum at over 1400 cm^{-1}, just beyond the highest wavenumber investigated (1200 cm^{-1}). High PL intensity is not associated with either amorphous or well crystallized Ta$_2$O$_5$, and has only been observed in substoichiometric crystalline samples [72]. Therefore, the intense PL background reflects high concentrations of radiation-induced O vacancies introduced into the crystalline Ta$_2$O$_5$. These concentrations then

decrease as the proportion of the amorphous phase increases, causing the observed drop in PL intensity as fluence further increases.

As the PL intensity diminishes, several Raman-active modes are revealed. These are labelled F, C, and G in Figure 4.5. Peak C is associated with the same symmetric Ta-O vibrations in TaO_6 polyhedra as seen in the unirradiated sample. However, peaks F and G, emerging at 220 cm^{-1} and 815 cm^{-1}, respectively, are both associated with Raman-active modes seen in substoichiometric amorphous Ta_2O_5. Peak F is related to the Ta-Ta interaction, likely across basal planes of TaO_5 pyramids [3,69], and G is associated with the Ta-O vibrations in the same coordination [3]. These bands have been shown to be prominent only for O-deficient samples [3], as the TaO_5 configuration does not exist in orthorhombic Ta_2O_5 [20]. This indicates that not only is long-range order lost during irradiation-induced amorphization, but the short-range order is also modified. The increase in intensity of peak G is complimentary to the decrease in intensity of peak D, which is consistent with the proposal by Tsuchiya et al. [3], that amorphous Ta_2O_5 is mostly comprised of TaO_5 and TaO_6 polyhedra and the absence of TaO_7. The short-range order modification from TaO_6 and TaO_7 polyhedra only, to having a significant presence of TaO_5 (at the expense of TaO_7 [3]), suggests a loss of oxygen from the material during irradiation.

In order to estimate the change in stoichiometry and proportion of TaO_5 in the amorphous material as a function of fluence, Pseudo-Voigt functions (assuming a linear background) were used to fit peaks C, G, and E, to compare the intensity contributions from TaO_5 and TaO_6 coordinations, while separating contributions from secondary scattering. Area ratios were calculated, in the form $\frac{A_5}{(A_6+A_5)}$, where A_5 is the area of peak G and A_6 is the area of peak C. The results are shown in Figure 4.6. The relative proportion of TaO_5 increases as a function of fluence, indicating an increased preference for this coordination geometry over TaO_6 as irradiation ensues. This suggests that O is preferentially lost from the amorphous material with increasing fluence. A previous study calculated these Raman-band intensity ratios for samples in which stoichiometry was directly measured using Rutherford backscattering spectroscopy (RBS) [3]. Using these relations, the stoichiometry of samples irradiated to the maximum fluence (1.0×10^{13} ions/cm^2) was estimated to be $Ta_2O_{4.2}$.
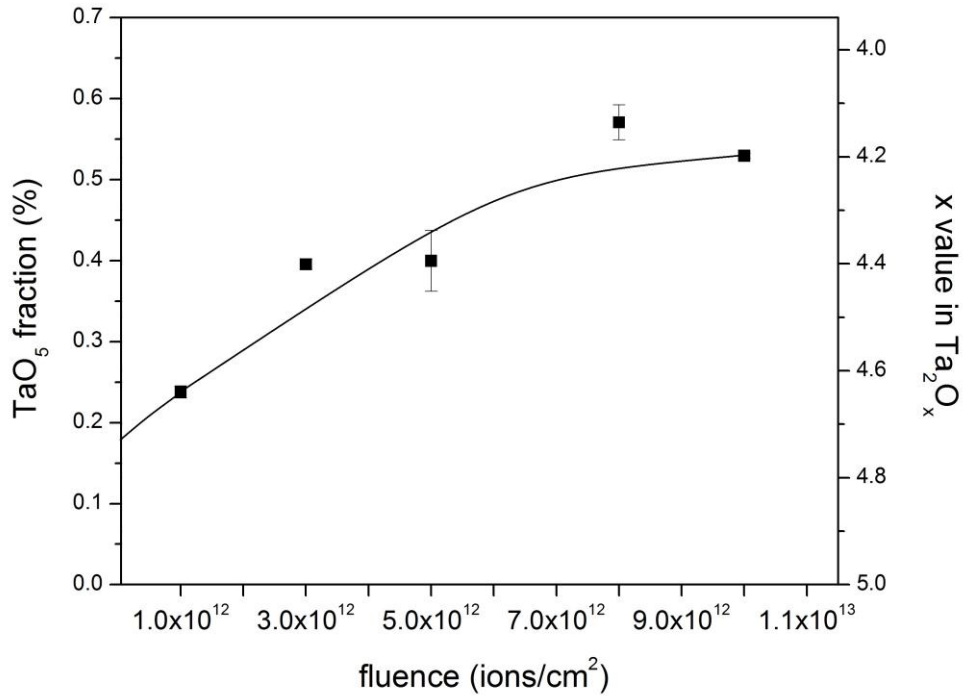
Figure 4.6. Estimates for the proportion of TaO_5 polyhedra (left axis) and stoichiometry of amorphous Ta_2O_5 samples (right axis) as a function of fluence.

4.3.3. Small-angle X-ray scattering

Samples irradiated to 5.0×10^{10} ions/cm^2 showed strong X-ray scattering. High intensity curved streaks were observed when the tracks were tilted with respect to the x-ray beam, consistent with high-aspect ratio damage structures. Thus, these data provide evidence of ion tracks [66,67]. Several models were used to fit this data, shown in Figure 4.7, including a simple cylinder model (assuming a constant density) and a core-shell cylinder model. Both models yield very similar total track diameters of 12.7 ± 0.4 nm and 12.9 ± 0.2 nm, respectively, though the core-shell model provided a better fit to the data. This model yielded a core diameter of 5.2 ± 0.2 nm, with a slightly lower density compared to the shell. The total track diameter is consistent with the direct-impact model estimate of 14.7 nm, as determined through XRD analysis.
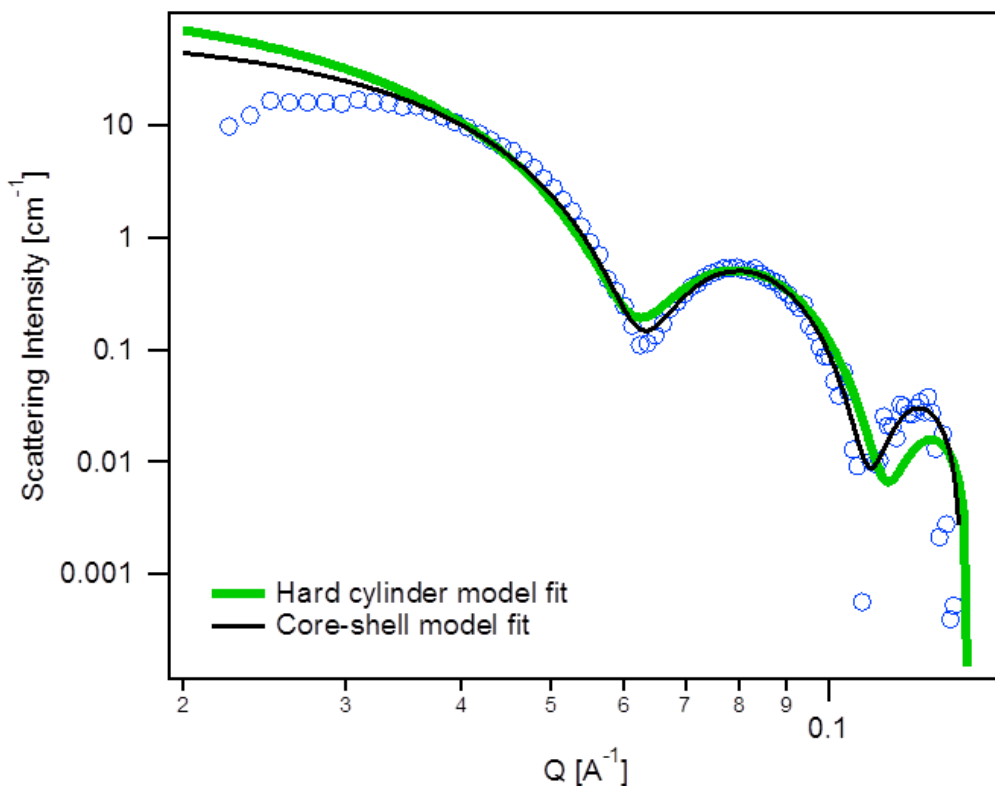
Figure 4.7. Intensity profiles for Ta_2O_5 irradiated to 5.0×10^{10} ions/cm^2, showing the quality of fit for both hard cylinder and core-shell models (green line and black line, respectively).

4.3.4. Transmission electron microscopy

TEM images were obtained from samples irradiated to 5.0×10^{10} ions/cm^2, and are shown in Figure 4.8. Bright-field image (a) shows that tracks are approximately parallel and exhibit a core-shell morphology. The lighter inner portion of each track is the track core, and the surrounding darker region is the track shell. The deviation of tracks from being parallel is due to deflection caused by nuclear collisions [74], even though the nuclear dE/dx was shown to be low. Figure 4.8b shows the track shells with higher resolution. Using these images, the average track core diameter was calculated to be 5.7 ± 0.5 nm, with an average total track diameter of 11.1 ± 0.4 nm. Because images were lacking strong contrast between the track shells and matrix, this total track diameter value is considered to be a lower bound. These measurements agree well with the SAXS analysis. Using dark-field imaging, ion tracks are observed as parallel dark lines and show similar width profiles (Figure 4.8c). A close-up of a single ion track core is

shown in Figure 4.8d, revealing its non-cylindrical, irregular, and possibly discontinuous nature. This may indicate an efficient epitaxial recrystallization process during quenching or near-threshold track formation conditions. The width of each track is greater near the particle surface, possibly indicating the loss of material to the environment before melt-quenching. However, particles were crushed before TEM analysis and the observed surface may not represent the original surface during irradiation.
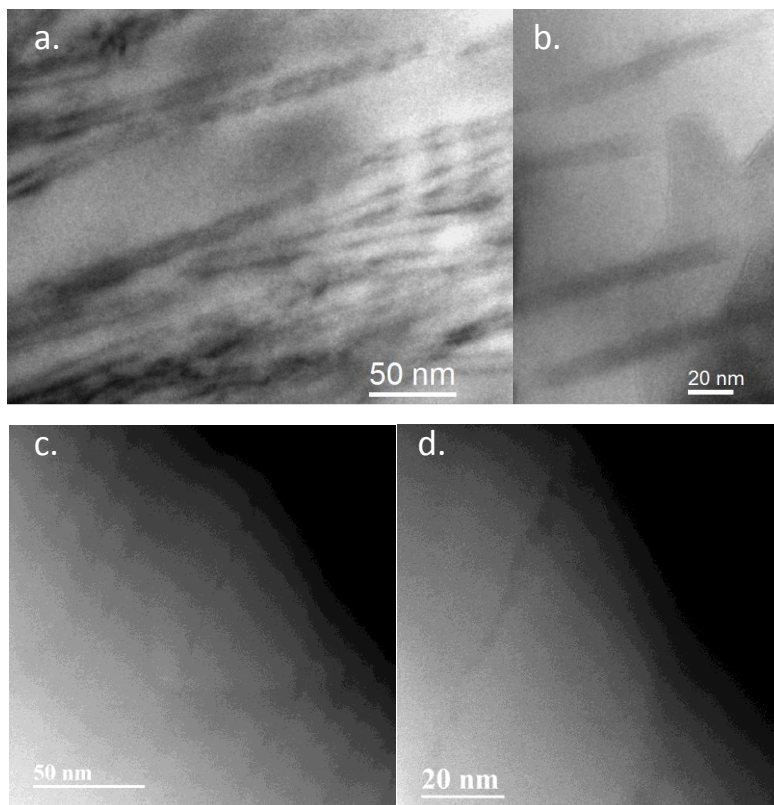
Figure 4.8. TEM images of a Ta_2O_5 particle irradiated to 5.0×10^{10} ions/cm^2. Bright-field images show core-shell morphology (a) and track shells with higher resolution (b). Dark-field images, (c) and (d), show the irregular nature of the track cores.

4.4. Discussion

Crystalline Ta_2O_5 samples begin showing diffuse amorphous diffraction maxima at a fluence of 3.0×10^{11} ions/cm^2. Within an order of magnitude increase in fluence (up to 3.0×10^{12} ions/cm^2), the material becomes completely amorphous. This fluence is quite low as compared with most oxides, as the threshold for full amorphization is typically over 1.0×10^{13} ions/cm^2 (for

example, Al_2O_3 [75], ZrO_2 [76], $La_2Ti_2O_7$ [44], $Gd_2Ti_2O_7$ [77], and various compositions of M_2TiO_5 [43]). During the amorphization process, the crystalline portion of the material undergoes anisotropic lattice strain. This is likely due to stress applied by the surrounding, lower density amorphous material, but may also reflect a reorientation of Ta-O polyhedra that relates to the amorphization process. Inter-polyhedral connections along the *b*-axis are relatively weak, consisting primarily of corner-shared polyhedra. Collapse has been shown to occur first along this axis in hydrostatic pressure-induced amorphization of crystalline Ta_2O_5 [5], reflecting the relative instability of the structure along this axis. As bonds break and polyhedra rearrange (for example, due to remnant thermal or pressure transients from nearby ion impact), they may preferentially tilt along the direction of the *a*-axis, thereby providing additional space in the *b* and *c*-directions. This would account for the observed strain, as it would lead to an expansion of the *a* axis and contraction of the *b* and *c* axes. This hypothesis may be further supported by the propensity for polyhedra to become plane-sharing in amorphous Ta_2O_5, especially in substoichiometric conditions [3].

The amorphous fractions calculated from XRD data show a smooth and continuous increase as a function of fluence. The best fit of these data was obtained using a direct-impact model, suggesting that amorphous material is formed along a single ion's trajectory, without the requirement of multiple impacts for defect accumulation. The track diameter estimated by this model is approximately 14.7 nm, which is large in comparison to most ion tracks observed in the literature [78–80]. SAXS analysis estimated a total track diameter of 12.9 nm, which is supported by the TEM measurements which estimated an average total track diameter of 11.2 nm. The core size estimated with these two models are also in good agreement, as SAXS analysis yields approximately 5.2 nm and TEM measurements approximately 5.7 nm. The direct-impact model overestimates the track diameter as calculated from SAXS and TEM data, while assuming a fully amorphous structure within the track. This suggests that the defect accumulation within the track shells, most importantly on the O sublattice, plays a significant role in the amorphization. In other words, the amorphous fraction increases at a rate comparable to the formation of large (14.7 nm) fully amorphous tracks, and because the

amorphous cores are much smaller (as calculated by SAXS and TEM), the defect-rich shells must play a role in further amorphization.

At a fluence of 3.0×10^{11} ions/cm^2, where amorphization is first evident in the XRD data, the Raman spectra have become overwhelmed by a broad PL emission band. This PL is not associated with the amorphous phase, but rather O vacancies existing within the crystalline Ta_2O_5 structure [72]. These vacancies are likely related to defect-rich track shells and/or the loss of connectivity between polyhedra resulting in dangling bonds. As point defects are not dominant in the amorphous structure [3], the PL intensity diminishes as this phase is formed at the expense of the defect-rich Ta_2O_5 structure. High levels of O deficiency are achieved in the amorphous structure by a decrease in the coordination of Ta from 6 to 5, and preferential plane-sharing of polyhedra as opposed to simple corner- and edge-sharing [3]. Therefore, the observation that the TaO_5/TaO_6 ratio increases with fluence indicates that ion irradiation is increasing the O deficiency. In other words, a preferential loss of oxygen occurs as a result of irradiation, leading to an O deficient coordination. The actual stoichiometry of irradiated samples was estimated using a previously published relation between the TaO_5/TaO_6 Raman-band intensity ratio and directly measured stoichiometry values using RBS [3]. Using these data, the stoichiometry of samples irradiated to 1.0×10^{13} ions/cm^2 is estimated to be $Ta_2O_{4.2}$. Preferential loss of O during heavy ion irradiation has been observed in several oxides [46,81–83], including the direct observation of O ejection from track cores [47,48]. This anion ejection has also been observed in fluoride materials [45,49], and remains poorly understood.

5. Conclusion

Swift [197]Au ions have induced amorphization in crystalline Ta_2O_5. During this process, the crystalline unit cell undergoes an anisotropic distortion in which the network of TaO_6 and TaO_7 polyhedra that comprise the structure lose connectivity, likely along the long b-axis. Polyhedra may then rotate to align more closely with the a-axis, leading to a contraction of b and c axes while expanding along the a axis. The amorphous phase created during irradiation is comprised of TaO_5 polyhedra in the absence of TaO_7, and the ratio of TaO_5 to TaO_6 was found to increase with fluence. Because O deficiency is balanced by a transition from corner-sharing polyhedra to

an edge- and plane-sharing configuration (causing a decrease in Ta coordination from 6 to 5), these data clearly indicate a loss of O during ion irradiation. The final stoichiometry of samples irradiated to 1.0×10^{13} ions/cm^2 is estimated to be $Ta_2O_{4.2}$. SAXS data suggest that ion tracks exhibit a core-shell morphology, in which the amorphous core is surrounded by a defect-rich shell. The average diameter of the track cores and shells (total track diameter) were estimated to be 5.2 ± 0.2 nm and 12.9 ± 0.2 nm, respectively. TEM data support this analysis, as images directly show the core-shell boundaries, and measurements estimated core and total track diameters of 5.7 ± 0.5 nm and 11.1 ± 0.4 nm, respectively. These total track diameter measurements are both lower than the direct-impact model estimate of 14.7 nm, which assumes that tracks are large and fully amorphous. This observation of a core-shell morphology, along with the interrelation of amorphization and O deficiency, suggest that defects within track shells play a significant role in the amorphization of Ta_2O_5 under irradiation.

Acknowledgements

References

[1]   W. Andreoni, C. a. Pignedoli, Ta2O5 polymorphs: Structural motifs and dielectric constant from first principles, Appl. Phys. Lett. 96 (2010) 062901. doi:10.1063/1.3308475.

[2]   J.-J. Lee, H.-J. Kim, Y.-G. Kang, Y.-H. Kim, H.-G. Park, B.-Y. Kim, et al., Vertical Liquid Crystal Orientation on Amorphous Tantalum Pentoxide Surfaces Depending on Anisotropic Dipole–Dipole Interaction via Ion Beam Irradiation, Jpn. J. Appl. Phys. 50 (2011) 031701. doi:10.1143/JJAP.50.031701.

[3]   T. Tsuchiya, H. Imai, S. Miyoshi, P.-A. Glans, J. Guo, S. Yamaguchi, X-ray absorption, photoemission spectroscopy, and Raman scattering analysis of amorphous tantalum oxide with a large extent of oxygen nonstoichiometry., Phys. Chem. Chem. Phys. 13 (2011) 17013–8. doi:10.1039/c1cp21310e.

[4]   S. Ezhilvalavan, T.-Y. Tseng, Conduction mechanisms in amorphous and crystalline Ta[sub 2]O[sub 5] thin films, J. Appl. Phys. 83 (1998) 4797. doi:10.1063/1.367272.

[5]   X. Lu, Q. Hu, W. Yang, L. Bai, H. Sheng, L. Wang, et al., Pressure-Induced Amorphization in Single-Crystal Ta2O5 Nanowires: A Kinetic Mechanism and Improved Electrical Conductivity, J. Am. Chem. Soc. (2013) 13947–13953.

[6]   P.C. Joshi, M.W. Cole, Influence of postdeposition annealing on the enhanced structural and electrical properties of amorphous and crystalline Ta2O5 thin films for dynamic random access memory applications, J. Appl. Phys. 86 (1999) 871. doi:10.1063/1.370817.

[7]   C. Joseph, P. Bourson, M.D. Fontana, Amorphous to crystalline transformation in Ta2O5 studied by Raman spectroscopy, J. Raman Spectrosc. 43 (2012) 1146–1150. doi:10.1002/jrs.3142.

[8]   Y. Zhu, F. Yu, Y. Man, Q. Tian, Y. He, N. Wu, Preparation and performances of nanosized Ta2O5 powder photocatalyst, J. Solid State Chem. 178 (2005) 224–229. doi:10.1016/j.jssc.2004.11.015.

[9]   Y. Yang, O. Sugino, Y. Kawazoe, Exceptionally long-ranged lattice relaxation in oxygen-deficient Ta2O5, Solid State Commun. 195 (2014) 16–20. doi:10.1016/j.ssc.2014.06.021.

[10]   H. Kimura, J. Mizuki, S. Kamiyama, H. Suzuki, Extended x-ray absorption fine structure analysis of the difference in local structure of tantalum oxide capacitor films produced by various annealing methods, Appl. Phys. Lett. 66 (1995) 2209. doi:10.1063/1.113169.

[11]   R. Ramprasad, First principles study of oxygen vacancy defects in tantalum pentoxide, J. Appl. Phys. 94 (2003) 5609–5612. doi:10.1063/1.1615700.

[12]   C. Chaneliere, S. Four, J.L. Autran, R.A.B. Devine, Comparison between the properties of amorphous and crystalline Ta 2 O 5 thin ® lms deposited on Si, 39 (1999) 261–268.

[13]   E. Atanassova, R. V Konakova, V.F. Mitin, J. Koprinarova, O.S. Lytvym, O.B. Okhrimenko, et al., Effect of microwave radiation on the properties of Ta 2 O 5 – Si microstructures, 45 (2004) 123–135. doi:10.1016/j.microrel.2004.04.018.

[14]   F.-C. Chiu, J.-J. Wang, J.Y. Lee, S.C. Wu, Leakage currents in amorphous Ta[sub 2]O[sub 5] thin films, J. Appl. Phys. 81 (1997) 6911. doi:10.1063/1.365252.

[15]   Q. Li, H. Zhang, B. Cheng, R. Liu, B. Liu, J. Liu, et al., Pressure-induced amorphization in orthorhombic Ta2O5: An intrinsic character of crystal, J. Appl. Phys. 115 (2014) 193512. doi:10.1063/1.4879245.

[16]   Y. Noda, B. Lee, K. Domen, J.N. Kondo, Synthesis of Crystallized Mesoporous Tantalum Oxide and Its Photocatalytic Activity for Overall Water Splitting under Ultraviolet Light Irradiation, (2008) 5361–5367.

[17]   I.E. Grey, W.G. Mumme, R.S. Roth, The crystal chemistry of L-Ta2O5 and related structures, J. Solid State Chem. 178 (2005) 3308–3314. doi:10.1016/j.jssc.2005.08.011.

[18]   L. a. Aleshina, S. V. Loginova, Rietveld analysis of X-ray diffraction pattern from β-Ta2O5 oxide, Crystallogr. Reports. 47 (2002) 415–419. doi:10.1134/1.1481927.

[19]   C. Askeljung, B.-O. Marinder, M. Sundberg, Effect of heat treatment on the structure of L-Ta2O5:, J. Solid State Chem. 176 (2003) 250–258. doi:10.1016/j.jssc.2003.07.003.

[20]   N.C. Stephenson, R.S. Roth, Structural Systematics in the Binary System Ta2O5-WO3. V. The Structure of the low-T form of Tantalum Oxide L-Ta2O5, Acta Cryst. (1971).

[21]   N.C. Stephenson, R.S. Roth, The Crystal Structure of the High Temperature Form of Ta2O5, J. Solid State Chem. 3 (1971) 145–153. doi:10.1016/0022-4596(71)90018-1.

[22]   J.L. Waring, R.S. Roth, Effect of oxide additions on polymorphism of tantalum pentoxide (system Ta2O5-TiO2), J. Res. Natl. Bur. Stand. Sect. A Phys. Chem. 72A (1968) 175. doi:10.6028/jres.072A.018.

[23]   H. Hummel, R. Fackler, P. Remmert, Tantaloxide durch Gasphasenhydrolyse, Druckhydrolyse und Transportreaktion aus 2H-TaS2: Synthesen von TT-Ta2O5 und T-Ta2O5 und Kristallstruktur von T-, Chem. Ber. (1992) 551–556. doi:10.1002/cber.19921250304.

[24]   F. Izumi, H. Kodama, A new modification of tantalum(V) oxide, J. Less-Common Met. 63 (1979) 305–307.

[25] A. Fukumoto, K. Miwa, Prediction of hexagonal Ta 2 O 5 structure by first-principles calculations, Phys. Rev. B. 55 (1997) 155–160. doi:10.1103/PhysRevB.55.11155.

[26] Z. Helali, M. Calatayud, C. Minot, Novel Delta-Ta 2 O 5 Structure Obtained from DFT Calculations, J. Phys. Chem. C. 118 (2014) 13652–13658. doi:10.1021/jp503088h.

[27] S. Lagergren, A. Magneli, On the Tantalum-Oxygen System, Acta Chem. Scand. 6 (1952) 444–446.

[28] X.Q. Liu, X.D. Han, Z. Zhang, L.F. Ji, Y.J. Jiang, The crystal structure of high temperature phase Ta2O5, Acta Mater. 55 (2007) 2385–2396. doi:10.1016/j.actamat.2006.11.031.

[29] Zaslavskii, (n.d.).

[30] Laves, Petter, (n.d.).

[31] I.P. Zibrov, V.P. Filonenko, Structures and phase transitions of B-Ta2O5 and Z-Ta2O5: two high-pressure forms of Ta2O5, Acta Crystallogr. Sect. B Struct. Sci. 56 (2000) 659–665.

[32] M. Audier, B. Chenevier, H. Roussel, L. Vincent, a. Peña, a. Lintanf Salaün, A very promising piezoelectric property of thin films. I: Monoclinic–trigonal phase transition, J. Solid State Chem. 184 (2011) 2023–2032. doi:10.1016/j.jssc.2011.06.001.

[33] Y. Zhang, W.J. Weber, D. a. Grove, J. Jensen, G. Possnert, Electronic stopping powers for heavy ions in niobium and tantalum pentoxides, Nucl. Instruments Methods Phys. Res. Sect. B Beam Interact. with Mater. Atoms. 250 (2006) 62–65. doi:10.1016/j.nimb.2006.04.148.

[34] C.L. Tracy, J. McLain Pray, M. Lang, D. Popov, C. Park, C. Trautmann, et al., Defect accumulation in ThO2 irradiated with swift heavy ions, Nucl. Instruments Methods Phys. Res. Sect. B Beam Interact. with Mater. Atoms. 326 (2014) 169–173. doi:10.1016/j.nimb.2013.08.070.

[35] T. Wiss, H. Matzke, C. Trautmann, M. Toulemonde, S. Klaumunzer, Radiation damage in UO2, by swift heavy ions, Nucl. Instruments Methods Phys. Res. Sect. B Beam Interact. with Mater. Atoms. 122 (1997) 583–588.

[36] A. Benyagoub, Mechanism of the monoclinic-to-tetragonal phase transition induced in zirconia and hafnia by swift heavy ions, Phys. Rev. B. 72 (2005) 094114. doi:10.1103/PhysRevB.72.094114.

[37] M. Lang, F. Zhang, J. Zhang, C. Tracy, A. Cusick, J. von Ehr, et al., Swift Heavy Ion-Induced Phase Transformation in Gd2O3, Nucl. Instruments Methods Phys. Res. Sect. B Beam Interact. with Mater. Atoms. 326 (2014) 121–125.

[38] S. Hemon, V. Chailley, E. Doorhyee, C. Dufour, F. Gourbilleau, F. Levesque, et al., Phase transformation of polycrystalline Y2O3 under irradiation with swift heavy ions, Nucl. Instruments Methods Phys. Res. Sect. B Beam Interact. with Mater. Atoms. 122 (1997) 563–565.

[39] B. Schuster, F. Fujara, B. Merk, R. Neumann, T. Seidl, C. Trautmann, Response behavior of ZrO2 under swift heavy ion irradiation with and without external pressure, Nucl. Instruments Methods Phys. Res. Sect. B Beam Interact. with Mater. Atoms. 277 (2012) 45–52. doi:10.1016/j.nimb.2011.12.060.

[40] W. Weber, Models and mechanisms of irradiation-induced amorphization in ceramics, Nucl. Instruments Methods Phys. Res. Sect. B Beam Interact. with Mater. Atoms. 166-167 (2000) 98–106. doi:10.1016/S0168-583X(99)00643-6.

[41] V. Kumar, D. Pratap, A. Jain, D.C. Agarwal, I. Sulania, A. Tripathi, et al., Crystalline to amorphous phase transition of tin oxide nanocrystals induced by SHI at low temperature, AIP Conf. Proc. 715 (2012) 715–716. doi:10.1063/1.4710203.

[42] A. Benyagoub, Investigations by X-ray diffraction of swift heavy ion induced effects in inorganic materials, Nucl. Instruments Methods Phys. Res. Sect. B Beam Interact. with Mater. Atoms. 225 (2004) 88–96. doi:10.1016/j.nimb.2004.03.083.

[43] C.L. Tracy, M. Lang, J. Zhang, F. Zhang, Z. Wang, R.C. Ewing, Structural response of A2TiO5 (A=La, Nd, Sm, Gd) to swift heavy ion irradiation, Acta Mater. 60 (2012) 4477–4486. doi:10.1016/j.actamat.2012.05.005.

[44] S. Park, M. Lang, C.L. Tracy, J. Zhang, F. Zhang, C. Trautmann, et al., Swift heavy ion irradiation-induced amorphization of La2Ti2O7, Nucl. Inst. Methods Phys. Res. B. 326 (2014) 145–149. doi:10.1016/j.nimb.2013.10.035.

[45] K. Schwartz, G. Wirth, C. Trautmann, T. Steckenreiter, Ion-induced formation of colloids in LiF at 15 K, Phys. Rev. B. 56 (1997) 10711–10714. doi:10.1103/PhysRevB.56.10711.

[46] A.B. Cusick, M. Lang, F. Zhang, J. Zhang, C. Trautmann, R.C. Ewing, Phase transformation and chemical decomposition of nanocrystalline SnO2 under heavy ion irradiation, 2015.

[47] V. Saikiran, N. Srinivasa Rao, G. Devaraju, G.S. Chang, a. P. Pathak, Formation of Ge nanocrystals from ion-irradiated GeO2 nanocrystals by swift Ni ion beam, Nucl. Instruments Methods Phys. Res. Sect. B Beam Interact. with Mater. Atoms. 312 (2013) 1–6. doi:10.1016/j.nimb.2013.07.005.

[48] S. Takaki, K. Yasuda, T. Yamamoto, S. Matsumura, N. Ishikawa, Atomic structure of ion tracks in Ceria, Nucl. Instruments Methods Phys. Res. Sect. B Beam Interact. with Mater. Atoms. 326 (2014) 140–144. doi:10.1016/j.nimb.2013.10.077.

[49]   J. Jensen, a Dunlop, S. Della-Negra, Microscopic observations of metallic inclusions generated along the path of MeV clusters in CaF2, Nucl. Instruments Methods Phys. Res. Sect. B Beam Interact. with Mater. Atoms. 146 (1998) 399–404. doi:10.1016/S0168-583X(98)00515-1.

[50]   M. Toulemonde, C. Dufour, A. Meftah, E. Paumier, Transient thermal processes in heavy ion irradiation of crystalline inorganic insulators, Nucl. Instruments Methods Phys. Res. Sect. B Beam Interact. with Mater. Atoms. 166-167 (2000) 903–912. doi:10.1016/S0168-583X(99)00799-5.

[51]   M. Toulemonde, J.M. Costantini, C. Dufour, A. Meftah, E. Paumier, F. Studer, Track creation in SiO2 and BaFe12O19 by swift heavy ions: a thermal spike description, Nucl. Instruments Methods Phys. Res. Sect. B Beam Interact. with Mater. Atoms. 116 (1996) 37–42.

[52]   G. Szenes, Thermal spike model of amorphous track formation in insulators irradiated by swift heavy ions, Nucl. Instruments Methods Phys. Res. Sect. B Beam Interact. with Mater. Atoms. 2 (1996) 1–4.

[53]   S. Klaumunzer, Thermal-Spike Models for Ion Track Physics: A Critical Examination, in: Med. Phys., 2008: pp. 293–323. doi:10.1118/1.2823217.

[54]   G. Szenes, Coulomb explosion at low and high ion velocities, Nucl. Instruments Methods Phys. Res. Sect. B Beam Interact. with Mater. Atoms. 298 (2013) 76–80. doi:10.1016/j.nimb.2013.01.033.

[55]   W. Li, M.D. Rodriguez, P. Kluth, M. Lang, N. Medvedev, M. Sorokin, et al., Effect of doping on the radiation response of conductive Nb–SrTiO3, Nucl. Instruments Methods Phys. Res. Sect. B Beam Interact. with Mater. Atoms. 302 (2013) 40–47. doi:10.1016/j.nimb.2013.03.010.

[56]   R.L. Fleischer, P.B. Price, R.M. Walker, Nuclear Tracks in Solids, University of California Press, 1975.

[57]   N. Itoh, D.M. Duffy, S. Khakshouri, a M. Stoneham, Making tracks: electronic excitation roles in forming swift heavy ion tracks., J. Phys. Condens. Matter. 21 (2009) 474205. doi:10.1088/0953-8984/21/47/474205.

[58]   P. Audebert, P. Daguzan, A. Dos Santos, J.C. Gauthier, J.P. Geindre, S. Guizard, et al., Space-Time Observation of an Electron Gas in SiO2, Phys. Rev. Lett. 73 (1994) 1990–1993.

[59]   K.H. Bennemann, Ultrafast dynamics in solids, J. Phys. Condens. Matter. 16 (2004) R995–R1056. doi:10.1088/0953-8984/16/30/R01.

[60] G. Sciaini, M. Harb, S.G. Kruglik, T. Payer, C.T. Hebeisen, F.-J.M. zu Heringdorf, et al., Electronic acceleration of atomic motions and disordering in bismuth., Nature. 458 (2009) 56–9. doi:10.1038/nature07788.

[61] M. Lang, C.L. Tracy, R.I. Palomares, F. Zhang, D. Severin, M. Bender, et al., Characterization of Ion-Induced Radiation Effects in Nuclear Materials using Synchrotron X-ray Techniques, 2014.

[62] J.F. Ziegler, M.D. Ziegler, J.P. Biersack, SRIM – The stopping and range of ions in matter (2010), Nucl. Instruments Methods Phys. Res. Sect. B Beam Interact. with Mater. Atoms. 268 (2010) 1818–1823. doi:10.1016/j.nimb.2010.02.091.

[63] A.P. Hammersley, S.O. Svensson, M. Hanfland, A.N. Fitch, D. Häusermann, FIT2D, (2005).

[64] J. Rodriguez-Carvajal, FULLPROF Suite, (2011).

[65] T.J.B. Holland, S.A.T. Redfern, Unit cell refinement from powder diffraction data : the use of regression diagnostics, 61 (1997).

[66] B. Afra, M.D. Rodriguez, C. Trautmann, O.H. Pakarinen, F. Djurabekova, K. Nordlund, et al., SAXS investigations of the morphology of swift heavy ion tracks in α-quartz., J. Phys. Condens. Matter. 25 (2013) 045006. doi:10.1088/0953-8984/25/4/045006.

[67] B. Afra, M. Lang, M.D. Rodriguez, J. Zhang, R. Giulian, N. Kirby, et al., Annealing kinetics of latent particle tracks in Durango apatite, Phys. Rev. B - Condens. Matter Mater. Phys. 83 (2011) 1–5. doi:10.1103/PhysRevB.83.064116.

[68] J.C. Sarker, R. Vasan, Y.F. Makableh, S. Lee, a. I. Nusir, M.O. Manasreh, Enhanced performance of surface modified InAs quantum dots solar cell by a sol-gel grown tantalum pentoxide antireflection coating, Sol. Energy Mater. Sol. Cells. 127 (2014) 58–62. doi:10.1016/j.solmat.2014.03.055.

[69] U. Balachandran, N.G. Eror, A study of the crystal structure of B-Ta205 by vibrational spectroscopy and X- ray diffraction, J. Mater. Sci. Lett. 1 (1982) 219–222.

[70] P.S. Dobal, R.S. Katiyar, Y. Jiang, R. Guo, a S. Bhalla, Raman scattering study of a phase transition in tantalum pentoxide, J Raman Spectrosc. 31 (2000) 1061.

[71] R.R. Krishnan, K.M. Nissamudeen, K.G. Gopchandran, V.P.M. Pillai, V. Ganesan, Effect of doping and substrate temperature on the structural and optical properties of reactive pulsed laser ablated tin oxide doped tantalum oxide thin films, Vacuum. 84 (2010) 1204–1211. doi:10.1016/j.vacuum.2009.10.026.

[72]   M. Zhu, Z. Zhang, W. Miao, Intense photoluminescence from amorphous tantalum oxide films, Appl. Phys. Lett. 89 (2006) 10–13. doi:10.1063/1.2219991.

[73]   W. Miao, M.M. Zhu, Z.C. Li, Z.J. Zhang, Optical and Electric Properties of Aligned-Growing Ta2O5 Nanorods, Mater. Trans. 49 (2008) 2288–2291. doi:10.2320/matertrans.MRA2008137.

[74]   W. Li, M. Lang, A.J.W. Gleadow, M. V. Zdorovets, R.C. Ewing, Thermal annealing of unetched fission tracks in apatite, Earth Planet. Sci. Lett. 321-322 (2012) 121–127. doi:10.1016/j.epsl.2012.01.008.

[75]   A. Kabir, A. Meftah, J.P. Stoquert, M. Toulemonde, I. Monnet, Amorphization of sapphire induced by swift heavy ions: A two step process, Nucl. Instruments Methods Phys. Res. Sect. B Beam Interact. with Mater. Atoms. 266 (2008) 2976–2980. doi:10.1016/j.nimb.2008.03.151.

[76]   F. Lu, J. Wang, M. Lang, M. Toulemonde, F. Namavar, C. Trautmann, et al., Amorphization of nanocrystalline monoclinic ZrO2 by swift heavy ion irradiation, Phys. Chem. Chem. Phys. 14 (2012) 12295–12300. doi:10.1039/c2cp41553d.

[77]   M. Lang, F.X. Zhang, R.C. Ewing, J. Lian, C. Trautmann, Z. Wang, Structural modifications of Gd2Zr2- xTi xO7 pyrochlore induced by swift heavy ions: Disordering and amorphization, J. Mater. Res. 24 (2009) 1322–1334. doi:10.1557/jmr.2009.0151.

[78]   M. Lang, J. Lian, J. Zhang, F. Zhang, W.J. Weber, C. Trautmann, et al., Single-ion tracks in Gd2 Zr2-x Tix O7 pyrochlores irradiated with swift heavy ions, Phys. Rev. B - Condens. Matter Mater. Phys. 79 (2009) 1–9. doi:10.1103/PhysRevB.79.224105.

[79]   J. Wang, M. Lang, R.C. Ewing, U. Becker, Multi-scale simulation of structural heterogeneity of swift-heavy ion tracks in complex oxides., J. Phys. Condens. Matter. 25 (2013) 135001. doi:10.1088/0953-8984/25/13/135001.

[80]   P. Kluth, C.S. Schnohr, O.H. Pakarinen, F. Djurabekova, D.J. Sprouster, R. Giulian, et al., Fine structure in swift heavy ion tracks in amorphous SiO2, Phys. Rev. Lett. 101 (2008) 1–4. doi:10.1103/PhysRevLett.101.175503.

[81]   A. Kabir, A. Meftah, J.P. Stoquert, M. Toulemonde, I. Monnet, M. Izerrouken, Structural disorder in sapphire induced by 90.3 MeV xenon ions, Nucl. Instruments Methods Phys. Res. Sect. B Beam Interact. with Mater. Atoms. 268 (2010) 3195–3198. doi:10.1016/j.nimb.2010.05.087.

[82]   A. Iwase, H. Ohno, N. Ishikawa, Y. Baba, N. Hirao, T. Sonoda, et al., Study on the behavior of oxygen atoms in swift heavy ion irradiated CeO2 by means of synchrotron radiation X-

ray photoelectron spectroscopy, Nucl. Instruments Methods Phys. Res. Sect. B Beam Interact. with Mater. Atoms. 267 (2009) 969–972. doi:10.1016/j.nimb.2009.02.035.

[83] H. Ohno, a. Iwase, D. Matsumura, Y. Nishihata, J. Mizuki, N. Ishikawa, et al., Study on effects of swift heavy ion irradiation in cerium dioxide using synchrotron radiation X-ray absorption spectroscopy, Nucl. Instruments Methods Phys. Res. Sect. B Beam Interact. with Mater. Atoms. 266 (2008) 3013–3017. doi:10.1016/j.nimb.2008.03.155.

Chapter 5

Comparison of the Radiation Responses of Group 14 Oxides and Ta$_2$O$_5$ under High Energy Heavy Ion Irradiation

The response to SHI irradiation has been investigated in SnO$_2$ and PbO$_2$ to complete the body of data for the Group 14 oxide system. For comparative purposes, we have investigated Ta$_2$O$_5$, which exhibits very different properties and a large, complicated crystal structure. In this chapter, we will review the radiation responses of these materials, as well as the other Group 14 oxides (SiO$_2$ and GeO$_2$). The radiation responses will then be compared to each other on the basis of their materials properties (for example, bond ionicity, enthalpy of formation, and electrical resistivity), which will allow us to determine the correlations between specific materials properties and their effect on the material's response to swift heavy ion irradiation. For additional review of literature on these materials, please refer to Chapter 1.4.5.

5.1 Summary of the radiation responses of Group 14 oxides

Irradiation of SiO$_2$ (quartz) by SHIs results in the formation of continuous amorphous tracks along the ion trajectories [1,2] with a core-shell morphology [3]. Amorphous regions in the shell (surrounding the amorphous core) are denser than the matrix by approximately 2% as determined by SAXS [3]. The atomic morphology of amorphous SiO$_2$ is considered to be the same as samples amorphized through neutron and low energy ion irradiation [2]. This suggests that the mechanism of amorphization similarly involves a critical O vacancy concentration, above which crystallinity will be lost as the structure relaxes from the defective crystalline state into the amorphous form. Femtosecond laser irradiation has also led to amorphization in quartz [4].

The irradiation of hexagonal GeO$_2$ resulted in the separation of O atoms and the reduction of Ge^{4+} to Ge^0 [5]. This led to the formation of Ge nanocrystals surrounded by O-rich GeO$_2$ [5]. No other structural effects were reported in this study. Based on GIXRD results, however, it is

evident that the material also became amorphous during irradiation. The formation of Ge nanocrystals was also evidenced in GeO_2 glass subjected to an electron beam during TEM analysis [6]. The loss of oxygen from these samples was confirmed by a decrease in the O K-edge energy using EELS. In addition, this decomposition process was induced by femtosecond laser pulses above 0.4 µJ [7], and low energy ion irradiation [8]. The ion irradiation study compared the radiation response of two GeO_2 structures, showing the rutile-type structure to be more resistant to amorphization than the hexagonal structure, with an amorphization dose of $\sim 10^{15}$ ions/cm^2 compared with $\sim 10^{13}$ ions/cm^2 for the hexagonal structure [8].

Irradiation of nano-SnO_2 (presented in this study) led to the formation of crystalline SnO within the samples, providing indirect evidence of Sn reduction and O loss. Trace quantities of metallic Sn were also observed. The transformation was attributed to the accumulation of O vacancies during irradiation, leading to the collapse of the SnO_2 structure into SnO, potentially the result of defect ordering. Similarly, PbO_2 was shown to decompose into multiple crystalline intermediate oxides in this study (Pb_2O_3, multiple Pb_3O_4 structures), with PbO becoming the phase with highest diffraction intensity at high fluences. Trace quantities of metallic Pb were also observed. At the initial onset of the intermediate oxide diffraction maxima, an amorphous phase was also observed. The relative intensity of this phase in respect to the crystalline structures decreased as the PbO phase intensity became dominant at high fluences.

The irradiation of Ta_2O_5 in this study was shown to induce complete amorphization, which was explained by the loss of connectivity of polyhedral units (or the manner in which they connect). Ion tracks were determined to have a core-shell morphology, similar to those of SiO_2. A change in the Ta-O coordination polyhedra from corner- and edge-sharing TaO_6 to primarily plane-sharing TaO_5 polyhedra was evidenced. This was the result of oxygen loss during irradiation, resulting in an estimated final stoichiometry of $Ta_2O_{4.2}$. The loss of oxygen during irradiation is consistent with the SHI irradiation effects on SnO_2, PbO_2, and GeO_2, though in the case of Ta_2O_5, cation reduction was determined to be unlikely.

5.2. The role of materials properties in the radiation response of Group 14 oxides

SiO_2 is susceptible to amorphization, but remains chemically stable under SHI irradiation. This is, in part, due to the absence of multiple valence states in Si. The lowest energy chemical bonds are obtained with sp^3 hybrid orbitals, rendering the Si^{2+} state unstable. In comparison with the other Group 14 oxides (refer to Table 5.1), SiO_2 has the smallest bond lengths and the highest cation electronegativity, cohesive energy, enthalpy of formation, and bond dissociation energy. These properties are associated with the strong Si-O chemical bonds, forming tightly bound corner-sharing SiO_4 coordination polyhedra. Therefore, amorphization is likely associated with the loss of connectivity between these units [4] (or a change in their relative orientation) and has been proposed to occur as O vacancy concentrations reach a critical level, above which crystallinity is lost.

Ge, like Si, forms hybrid sp^3 orbitals that make Ge^{4+}-O bonds strong and the Ge^{2+} state unstable in the solid phase [9]. GeO_2 has slightly greater bond lengths and lower electronegativity, bond dissociation energy, enthalpy of formation, and cohesive energy compared with SiO_2. The difference in bond dissociation energy (~17%) may explain why Ge^{4+} was shown to reduce to its elemental state during irradiation, whereas Si^{4+} was not. The sp^3 bonds in both materials, although strong, do not prevent ion-induced cation reduction. The change in stoichiometry of GeO_2 in O deficient regions after irradiation was approximately 4% (on the surface). This is significantly less modified as compared with the loss observed in irradiated SnO_2 and PbO_2. This could be explained by the fact that Ge-O bond strengths are closer to those in SiO_2 (higher than SnO_2 and PbO_2), making the loss of O more difficult in GeO_2. However, this could also be explained by the lower energy ions used in the GeO_2 irradiation, with dE/dx ~10.62 keV/nm compared with ~44 keV/nm in the irradiation of SnO_2 and PbO_2. The amorphization process that occurred in GeO_2 is likely similar to that of SiO_2. This could be distinct from the process in PbO_2, which may be attributed to the severe chemical and structural modifications that occur during irradiation. High levels of O vacancies, valence state variation, and high free energy induce structural instability in the irradiated material. This, along with many high energy interfaces between regions of different crystalline phases, may promote the amorphization of crystalline material.

Previous studies have shown that both quartz (SiO_2) and hexagonal GeO_2 (β quartz-type) are more susceptible to amorphization than rutile-type GeO_2 under 1.5 MeV Xe irradiation (with nuclear stopping approximately equal to electronic stopping) [8]. This is likely due to the lower coordination and connectivity of corner-sharing GeO_4 polyhedra in comparison with the cross linked chains of GeO_6 polyhedra in rutile. The hexagonal structure of GeO_2 may therefore play a role in its increased sensitivity to amorphization under irradiation, over rutile-structured SnO_2 which does not amorphize.

The most chemically unstable materials in this system of study are SnO_2 and PbO_2, as significant portions of the samples were shown to undergo transformations to lower stoichiometric phases. Materials property values in Table 5.1 show that these two materials have the lowest electronegativities, enthalpies of formation, and bond dissociation energies. Unlike SiO_2 and GeO_2, their valence electron orbitals have energies very close to each other and do not form sp^3 hybrid orbitals. Their bonds are more ionic in nature (ionicity increases down the periodic chart [10]), with fractional ionicities of 0.559 and 0.563 for Sn and Pb, respectively. These materials also have the largest ionic/covalent radii and the longest bond lengths, which are associated with low electrostatic binding forces. These properties may facilitate preferential disorder on the O sublattice as these atoms are relatively weakly bound to the cations. Ionic conductivity is also high in these materials; SnO_2 is used as an oxidation catalyst [11] and PbO_2 an oxidizing agent [12] for this reason. Energy gained by the irradiation and high ionic conductivity facilitate the outward diffusion of oxygen and its eventual loss from the sample volume. This process leaves O deficient regions behind (leading to high O vacancy concentrations) and possibly cations in a reduced state. Track regions deficient in oxygen have been previously observed in irradiated CeO_2 [13]. Inherently high O vacancy concentrations (observed in both SnO_2 and PbO_2) are associated with low electrical resistivities, which are on the order of 10^{19} to 10^{22} Ω-cm lower than SiO_2 and GeO_2. This is because O vacancies are the origin of electron carriers in those materials [14]. All of the aforementioned properties of SnO_2 and PbO_2 likely play a role in their relatively high susceptibility to chemical effects under highly ionizing radiation.

Table 5.1. Materials Properties of Group 14 Dioxides and Ta_2O_5.

Property	Units	Ta2O5	SiO2	GeO2	SnO2	PbO2	
cation atomic mass	amu	181.0	28.1	72.6	118.7	207.2	
melting temperature (Tm)	K	2173	1999	1389	1902	563	[r]
heat capacity (Cp)	kJ/mol-K	135.1	69.8	82.6	52.6	73.4	[r]
electrical resistivity (ρ)	ohm-cm	10^8	5×10^{18}	10^{15}	5×10^{-4}	10^{-4} [c]	[L]
ionic radius (4+ state)	Å	0.68 [k]	0.40	0.53	0.69	0.78	[t]
covalent radius (4+ state)	Å	1.34 [k]	1.18	1.22	1.41	1.46	[t]
bond length	Å	1.99 [u]	1.61 [v]	1.88 [w]	2.05 [x]	2.16 [u]	
band gap (Eg)	eV	4.74 [e]	9.0 [a]	6.1 [a]	3.5 [d]	0.23 [b], 1.6 [c]	
cohesive energy	eV/atom	7.41 [p]	7.45 [m]	6.6 [n]	4.91 [g]	not available	
crystal dissociation E	eV/atom	5.03	6.12	6.22	4.01	3.35	[r]
ΔH: MO2 (4+ state)	eV/atom	4.23 (5+)	3.15	2.00	1.99	0.96 [q]	[k]
ΔH: MO (2+ state)	eV/atom	N/A	N/A	N/A	1.45	1.13	[k]
ΔH: MxOy (mixed state)	eV/atom	N/A	N/A	N/A	N/A	1.04, 1.09 [q]	
bond dissociation E	ev/atom	1.67	2.76	2.29	1.89	1.31	[i]
cation electronegativity	unitless	1.98	1.91	1.76	1.63	1.62	[s]
fractional ionicity (M-O)	unitless	0.413	0.443	0.506	0.559	0.563	[y]

References (shown to the right of each row unless otherwise noted): a [15], b [16], c [17], d [18], e [19], f [20], g [21], h [1], i [22], j [23], k [24], L [25], n [26], q [27], r [28], s [29], t [12], u [30], v [2], w [31], x [32], y [33]

Along with ion-induced O deficiency, the formation SnO in irradiated SnO_2 is likely due to its large cohesive energy (only 11.2% lower than the initial SnO_2 structure). A material's cohesive energy is defined as the energy necessary to separate the solid into single neutral atoms in the gas state at an infinite separation. Sn^{2+} is not significantly less stable than Sn^{4+}, and SnO forms readily at ambient conditions. As argued in Chapter 2, high O vacancy concentrations may lead to defect ordering, leading to the collapse of the SnO_2 structure into SnO. This is facilitated by the fact that both structures being tetragonal with a unit cell volume reduction of only 3.1%. The intermediate phase, Sn_2O_3, is extremely rare with a very low binding energy [34], and therefore is not energetically favored to form. At high O vacancy concentrations, the SnO structure is energetically favored; this may explain why the irradiation of SnO_2 resulted in the formation of the SnO phase as opposed to becoming amorphous.

Similar to SnO_2, cation reduction is favored in PbO_2 during SHI irradiation, but in this case, the Pb^{2+} valence state is more stable than the Pb^{4+} state. This is due to the inert-pair effect, in which high Coulomb screening and orbital overlap make bonding with only two of the four valence electrons energetically favorable; bonds made with the *p* electrons have a higher

binding energy than bonds with both *p* and *s* electrons, as is the case with Sn. Therefore, the severity of chemical effects in irradiated PbO_2, as compared with SnO_2, is at least partially due to the material seeking higher stability. The enthalpy of formation of PbO is 0.17 eV/atom higher than that of PbO_2 (0.96 eV/atom) and is therefore an exothermic transformation (refer to Table 5.1). Transition to the most stable lead oxide, PbO, is complicated by the stability (or metastability) of the intermediate oxides that combine ions in both valence states (such as Pb_2O_3 and Pb_3O_4). Therefore, multiple intermediate phases are created, with PbO becoming dominant only at high fluences. Six distinct crystalline phases form during irradiation, likely creating high energy interfaces and stresses between grains of differing structures. The high levels of disorder during irradiation (high O vacancy concentrations, cation valence state variation, and multiple phase transformations occurring simultaneously) may promote the formation of the amorphous phase. This is supported by the decrease in proportion of the amorphous phase in high fluences, as order is gained as the PbO phase becomes dominant.

Ta_2O_5 is highly susceptible to amorphization under SHI irradiation, and exhibits a core-shell ion track morphology similar to SiO_2. This efficient damage process is likely due to its complex crystal structure and tightly bound coordination polyhedra (mostly TaO_6). The unit cell contains approximately 77 atoms (refer to Chapter 4), and the long range periodicity is more easily disrupted when the repeat distances along the axes are longer. The cohesive energy is essentially equal to that of SiO_2, with a higher cation electronegativity and enthalpy of formation. Pentavalent Ta ions in Ta_2O_5 arrange themselves with the greatest separation possible, which induces an asymmetrical charge distribution favoring polarization and covalency effects [35]. Based on this and the high electronegativity of Ta, these bonds are likely more covalent in nature than SiO_2 and contribute to strong polyhedral units. However, the bond dissociation energy is quite low in comparison (falling between values for SnO_2 and PbO_2) which may explain the evidence for a significant removal of oxygen during irradiation (Chapter 4), estimated to be 16%. Ta reduction was unlikely, however, as the oxidation state has been shown to saturate at 5+ during oxidation above a stoichiometry of $TaO_{2.17}$ [36]. Thus, reduction is not necessary for significant O loss. Similar to SiO_2, there may be a threshold for O vacancy concentration, above which amorphization occurs. Although the loss of oxygen has not been

suggested in previous SHI irradiations of SiO_2, it is possible that it does occur, and may therefore be consistent with the radiation responses the other Group 14 oxides and Ta_2O_5. Tracks for ions in the dE/dx range of those used in this study should create tracks of approximately 8 nm in diameter in SiO_2 [3]. In Ta_2O_5 the track diameter was estimated to be between 11 and 15 nm, indicating that amorphization and/or defect production is more efficient than in SiO_2.

The damage production model that best describes the radiation effects observed in this study is evidently the thermal-spike model (described in detail in Section 1.3.1). This model has been particularly successful describing the formation of amorphous tracks in materials irradiation by SHIs, such as those seen in SiO_2 and Ta_2O_5. Simulations have shown that ions with threshold dE/dx values induce melting in the cylindrical volume along an ion's trajectory, leading to fast quenching and the formation of amorphous tracks [37]. This model may also explain the change in stoichiometry of GeO_2, SnO_2, and PbO_2 under irradiation, as each of these materials also undergo thermal decomposition. Thus, the thermal transient that induces amorphous tracks in some materials may result in the formation of suboxide phases in others. This thermal mechanism would suggest a single-impact transformation process, where the transformed phase forms after a single ion impact (multiple impacts are not necessary for transformation). However, as discussed in Chapter 2, there is evidence that the transformation process in SnO_2 is not driven by a single-impact, but multiple-impact mechanism. This is due to the absence of ion tracks in low fluence samples, determined using TEM, and the slow increase of the SnO phase fraction as a function of fluence. Therefore, although is it plausible that the thermal transient plays a role in all radiation effects observed in the Group 14 and tantalum oxide system, it does not likely control the radiation response in those materials that undergo cation reduction and oxygen loss during irradiation. In other words, the thermal mechanism described by the thermal-spike model may drive the amorphization of SiO_2 and Ta_2O_5, but another mechanism is likely responsible for the chemical effects observed in others SnO_2 and PbO_2.

5.3. The effects of materials properties on the radiation response of Group 14 oxides

Forming relations between materials properties and structural responses to swift heavy ion irradiation has been one of the main goals of the community for over 40 years, yet little progress has been made. Several correlations have been assigned, for example, the increase of amorphous ion track size with an increase in electrical resistivity was evidenced, it was also noted that the band gap energy is a "relevant parameter" in scaling the sensitivity of oxides to amorphization [38]. Naguib and Kelly [39] developed a bond-type criterion in terms of ionicity in 1975, introducing thresholds for amorphization of non-metallic solids under ion irradiation. They proposed that materials with ionicities $\leq$ 0.47 should amorphize under irradiation, whereas materials with ionicities $\geq$ 0.60 should remain or become crystalline under irradiation. Another set of "rules" was given based on the thermal properties of materials. Using the ratio of crystallization temperature values (T_c) to melting temperatures (T_m), it was proposed that materials with T_c/T_m < 0.23 should remain or become crystalline during irradiation, and those > 0.23 should amorphize. This thermal criterion was supported by the observed radiation effects on many materials (including the Group 14 dioxides and Ta_2O_5). However, some values used in their analysis were clearly incorrect (T_m values), others were approximated (T_c values), and some were even unqualified for use in these comparisons (using T_c values measured from films on crystalline substrates, and therefore inconsistent with other values measured from bulk materials). The bond-type criterion was also supported by experimental results on many materials (including SiO_2 and GeO_2), but was not sufficient to describe the effects on others, including both SnO_2 and Ta_2O_5. Despite these issues, both of the proposed criteria utilize specific materials properties that clearly show trends with radiation response, showing that there are strong relationships between them. Using results from the systematic study of the Group 14 oxide system, we may extract specific associations between the varying materials properties and radiation responses observed.

In summary of the results presented in the current study, the following direct observations may be made:

- Increasing susceptibility to amorphization during SHI irradiation is associated with increasing enthalpy of formation, bandgap, electrical resistivity, and cation electronegativity, as well as decreasing bond ionicity and bond length.
- Increasing susceptibility to cation reduction during SHI irradiation is associated with increasing bond ionicity and decreasing enthalpy of formation, melting temperature, electrical resistivity, and cation electronegativity.
- Increasing susceptibility to oxygen loss during SHI irradiation is associated with increasing bond length and decreasing bond dissociation energy, bandgap, and electrical resistivity.

The following thresholds are observed for the Group 14 and tantalum oxide system, where ΔH is the material's enthalpy of formation, E_g is the bandgap, ρ is the electrical resistivity, χ is the electronegativity, and T_m is the melting temperature:

- Amorphization occurs under the following conditions:

$$ionicity \leq 0.506$$
$$\Delta H \geq 2.00 \; eV/atom$$
$$E_g \geq 4.74 \; eV$$
$$bond \; length \leq 1.99 \; \text{Å}$$
$$\rho \geq 10^8 \; \Omega \cdot cm$$
$$cation \; \chi \geq 1.76$$

- Cation reduction occurs under the following conditions:

$$ionicity \geq 0.506$$
$$\Delta H \leq 2.00 \; eV$$
$$T_m \leq 1902 \; K$$
$$\rho \leq 10^{15} \; \Omega \cdot cm$$
$$cation \; \chi \leq 1.76$$

- Oxygen loss occurs under the following conditions:

$$Bond\ dissociation\ E\ \leq\ 2.29\ eV/atom$$
$$E_g\ \leq\ 6.1\ eV$$
$$Bond\ length\ \geq\ 1.88\ \text{Å}$$
$$\rho\ \leq\ 10^{15}\ \Omega \cdot cm$$

The aforementioned associations and threshold property values should not be regarded as definitive correlations, but potential connections between the trends in materials properties and trends in radiation responses. It should be noted that several of these properties are related to each other. For example, bond ionicity is directly related to the difference in electronegativities between oxygen and the cation [33]. T_m and ΔH are both directly related to the shape and depth of interatomic potential wells (and therefore each other). Although an increase in ΔH may suggest a higher T_m (in ionic crystals especially [40]), this is not always the case. Bond length and bond dissociation energy are related by the magnitude of Coulombic forces between atoms, though direct relationships between them are difficult to define as a decrease in bond length is not always associated with higher bond dissociation energy. A direct relation exists between band gap and electrical resistivity, as an increase in band gap is usually associated with an increase in resistivity (though this is not always the case as it depends on the energy of the fermi level in relation to the center of the band gap).

The important consideration is that there are relations between many of these materials properties, yet they are not straightforward to define explicitly. Therefore, it is important to seek relations between radiation responses and many chemical and structural properties, to determine what characteristics may control a specific radiation effect. Beyond the aforementioned materials property relations, other considerations are evident:

- Susceptibility to amorphization increases with complexity of structure; the symmetry is relatively lower in trigonal SiO_2, hexagonal GeO_2, and Ta_2O_5, in comparison to rutile structured SnO_2 and PbO_2. This increase in susceptibility to amorphization is likely due to difficulty recrystallizing after being damaged. High-symmetry materials (for example, those with cubic structures) have been found to

be most unstable under anisotropic stresses, like those induced by irradiation [39], in comparison with more complex low-symmetry structures. This is supported by the fact that hexagonal GeO_2 was shown to be more susceptible to amorphization than the simpler rutile-structured GeO_2 [8].

- The association of decreasing bond ionicity (increasing covalent character) with increasing susceptibility to amorphization may be related to the low stability of substitutional defects in highly ionic materials. Because these defects result in like-atoms in close proximity, materials with highly ionic bonds cannot accommodate even low levels of substitutional disorder as they induce relatively high lattice strains. In contrast, covalent materials readily accept these defects due to the relatively short-range and directional nature of covalent bonds [39], which may lead to amorphization once a critical concentration is reached. Highly covalent Si-O bonds are regarded as the weakest-link in the amorphization of complex silicates, and susceptibility to amorphization has been shown to scale with increased proportion of Si-O bonds in these materials [41].

- High structural stability does not prevent amorphization; SiO_2, GeO_2, and Ta_2O_5 all exhibit a high enthalpy of formation, cohesive energy, and bond dissociation energy, but readily amorphize.

- Ion-induced defect accumulation is preferential on the anion sublattice, as stoichiometries consistently change to lower O content. This may be related to an ejection of O from ion tracks, as observed in CeO_2 [13] and the alkali-halides [42].

- The existence of stable lower oxides may support crystallization of those phases (over amorphization) in materials susceptible to oxygen loss under SHI irradiation, as this may be more energetically favorable. For example, the high cohesive energy and enthalpy of formation of SnO likely promotes its crystallization. The amorphous fraction in irradiated PbO_2 decreases as lower oxide crystalline structures become dominant (PbO and the intermediate oxides have higher enthalpy of formation than PbO_2).

- Oxygen loss in Ta_2O_5 may be facilitated by a recovery mechanism: coordination changes from 6 to 5, where polyhedra become plane-sharing over corner- and edge-sharing; this O-loss likely occurs in the absence of Ta reduction.

- Strong bonds with sp^3 orbitals and non-multivalency do not prevent cation reduction (though they may offer resistance), as GeO_2 has been shown to reduce to its elemental state.

- Fast anion diffusion (associated with nonstoichiometry) and low bond dissociation energy promote O loss, increased oxygen vacancy concentrations, and probably cation reduction. These result in an increased susceptibility to chemical effects under SHI irradiation (possibly leading to lower oxide formation or metallic inclusions).

- Higher electrical resistivity has been suggested to lead to an increase in amorphous track size [38]. However, the overall track diameter of Ta is larger than SiO_2 [3] while having 10 orders of magnitude lower resistivity (although track shells in Ta_2O_5 may not be amorphous, and in that case, this proposition may still hold).

- Self-trapping of excitons (Chapter 1.3.3) occurs in most oxides that have been observed to undergo anion loss and cation reduction under SHI irradiation [43–51]. Exciton decay has previously been associated with a change in cation charge state [52]. For these reasons, it is expected that this mechanism may be important in the radiation response of those materials.

5.4. Future Work

Amorphization of materials during swift heavy ion irradiation has been widely studied in the literature; the thermal-spike model has been developed to describe these effects and has done so adequately in most cases (the shortcomings of this model were discussed in Section 1.3.1). The current pressing issue in this field of work is describing the radiation effects in materials that are not accurately modeled using thermal consideration only. In particular, the mechanism related to preferential disorder on an oxide's oxygen sublattice (production of O vacancies over cation vacancies, leading in some cases to O loss), appears to control the radiation response in

many materials. This preferential disorder is also related to the reduction of the cation species during irradiation, and is responsible for the observed changes in stoichiometry in some materials. Obtaining a thorough understanding of this mechanism will allow the development of a more complete theoretical model that may describe radiation effects in a wide range of materials. This is the main goal in this field of study, which may be obtained with further investigation of the materials susceptible to these effects to determine specific materials properties relations. These investigations should include neutron scattering and diffraction techniques in addition to further TEM work. Because of the sensitivity of these neutron techniques to the oxygen sublattice in oxides, the combination of these data with further TEM imaging could facilitate a more complete characterization of this preferential disorder. The extent of oxygen deficiency in different materials due to ion impact may be determined on the nano-scale, as well as track morphology, including the distance of O-lattice modifications from an ion's trajectory. If ion tracks are not evident in a particular material, these techniques may be used to determine any inhomogeneity in oxygen content, indicating potential controlling mechanisms such as the role of grain boundaries in the loss of oxygen.

Determining the effects of specific materials properties on the radiation response of binary oxides requires a systematic approach, for example, the systematic study of the Group 14 oxides presented in this dissertation. However, this study lacks absolute consistency, as SiO_2 and GeO_2 were irradiated in somewhat different conditions compared with the materials presented here. Future work will require the investigation of material systems using identical experimental conditions (for example, temperature, grain size, dE/dx, fluence regime, and storage environment before and after irradiation). With these parameters held constant, a subsequent study of the Group 14 oxide system would allow a more quantitative comparison of the extent of oxygen loss and amorphization as a function of fluence in each material. In addition, other material systems must be investigated to allow different materials properties to vary as experimental conditions remain constant. Investigation of the Group 13 oxides (B_2O_3, Al_2O_3, Ga_2O_3, In_2O_3, Tl_2O_3) would add significantly to the systematic study of Group 14 oxides, not only for comparative purposes between groups, but also because of the different multivalency of cations and the rich variety of phases exhibited by these oxides (for example,

Ga$_2$O$_3$ has five readily formed phase modifications). Another system that must be investigated under identical conditions is the oxide series of Period 4 elements (most importantly the transition metals Sc, Ti, V, Cr, Mn, Fe, Co, Ni, Cu, Zn, and p-block elements Ga, Ge, As, Se). In this system, the 4s, 3d, and 4p shells gradually fill down the period (most often in that order). In addition to the aforementioned groups, it may also be necessary to study a series of oxides containing only non-multivalent cations, for which only one oxidation state is stable (for example, Group 1 and Group 2 metals), or a series of transition metal sesquioxides which contain cations that exhibit both the 3+ and 2+ state with approximately equal stabilities (and are therefore easily reducible). These systematic studies have the potential to elucidate the underlying relationships between materials properties and radiation response; they may allow the determination of what properties control the susceptibility of chemical effects under SHI irradiation, and what properties affect susceptibility to amorphization (and whether these may be competing effects).

References

[1]   A. Meftah, F. Brisard, J.M. Costantini, E. Dooryhee, M. Hage-Ali, M. Hervieu, et al., Track formation in SiO2 quartz and the thermal-spike mechanism, Phys. Rev. B. 49 (1994) 12457–12463. doi:10.1103/PhysRevB.49.12457.

[2]   L. Douillard, J.P. Duraud, Swift heavy ion amorphization of quartz — a comparative study of the particle amorphization mechanism of quartz, Nucl. Instruments Methods Phys. Res. Sect. B Beam Interact. with Mater. Atoms. 107 (1996) 212–217. doi:10.1016/0168-583X(95)01044-0.

[3]   B. Afra, M.D. Rodriguez, C. Trautmann, O.H. Pakarinen, F. Djurabekova, K. Nordlund, et al., SAXS investigations of the morphology of swift heavy ion tracks in α-quartz., J. Phys. Condens. Matter. 25 (2013) 045006. doi:10.1088/0953-8984/25/4/045006.

[4]   J. Hernandez-Rueda, D. Puerto, J. Siegel, M. Galvan-Sosa, J. Solis, Plasma dynamics and structural modifications induced by femtosecond laser pulses in quartz, Appl. Surf. Sci. 258 (2012) 9389–9393. doi:10.1016/j.apsusc.2011.12.020.

[5]   V. Saikiran, N. Srinivasa Rao, G. Devaraju, G.S. Chang, a. P. Pathak, Formation of Ge nanocrystals from ion-irradiated GeO2 nanocrystals by swift Ni ion beam, Nucl. Instruments Methods Phys. Res. Sect. B Beam Interact. with Mater. Atoms. 312 (2013) 1–6. doi:10.1016/j.nimb.2013.07.005.

[6]   N. Jiang, J. Qiu, J.C.H. Spence, Precipitation of Ge nanoparticles from GeO2 glasses in transmission electron microscope, Appl. Phys. Lett. 86 (2005) 1–3. doi:10.1063/1.1898423.

[7]   T. Asai, Y. Shimotsuma, T. Kurita, A. Murata, S. Kubota, M. Sakakura, et al., Systematic Control of Structural Changes in GeO $_2$ Glass Induced by Femtosecond Laser Direct Writing, J. Am. Ceram. Soc. 98 (2015) 1471–1477. doi:10.1111/jace.13482.

[8]   S.X. Wang, L.M. Wang, R.C. Ewing, Ion irradiation-induced amorphization of two GeO2 polymorphs, Nucl. Instruments Methods Phys. Res. B. 175-177 (2001) 615–619. http://www.sciencedirect.com/science/article/pii/S0168583X00006078.

[9]   K.N. Astankova, E.B. Gorokhov, V.A. Volodin, A. V Latyshev, M. Vergnat, U.H. Poincare, The Decomposition Mechanism of Metastable Solid GeO Film, in: 2009 Int. Student Sch. Semin. Mod. Probl. Micro- Nanoelectron., 2009: pp. 69–73.

[10]   J. Mimaki, T. Tsuchiya, T. Yamanaka, The bond character of rutile type SiO2 , GeO2 and SnO2 investigated by molecular orbital calculation, Energy. 215 (2000) 419–423.

[11]   M. Batzill, U. Diebold, The surface and materials science of tin oxide, Prog. Surf. Sci. 79 (2005) 47–154. doi:10.1016/j.progsurf.2005.09.002.

[12]   N.N. Greenwood, A. Earnshaw, Chemistry of the Elements pt.2, in: Chem. Elem., 1997: pp. 374–388.

[13]   S. Takaki, K. Yasuda, T. Yamamoto, S. Matsumura, N. Ishikawa, Atomic structure of ion tracks in Ceria, Nucl. Instruments Methods Phys. Res. Sect. B Beam Interact. with Mater. Atoms. 326 (2014) 140–144. doi:10.1016/j.nimb.2013.10.077.

[14]   D.J. Payne, R.G. Egdell, D.S.L. Law, P. a Glans, T. Learmonth, K.E. Smith, et al., Experimental and theoretical study of the electronic structures of alpha-PbO and beta-PbO2, (2007) 267–277. doi:10.1039/b612323f.

[15]   J. Lin, K. Xiong, J. Robertson, Atomic structure, electronic structure, and band offsets at Ge:GeO:GeO2 interfaces, Appl. Phys. Lett. 97 (2010) 3. doi:10.1063/1.3525371.

[16]   D.O. Scanlon, A.B. Kehoe, G.W. Watson, M.O. Jones, W.I.F. David, D.J. Payne, et al., Nature of the Band Gap and Origin of the Conductivity of PbO2 Revealed by Theory and Experiment, Phys. Rev. Lett. 107 (2011) 246402. doi:10.1103/PhysRevLett.107.246402.

[17]   J.. Jacquemin, G. Bordure, Electronic energy band calculation in β-PbO2 comparison with SnO2 and GeO2 energy band structures, Solid State Commun. 11 (1972) 1563–1567. doi:10.1016/0038-1098(72)90520-0.

[18]   S. Rani, N.K. Puri, S.C. Roy, M.C. Bhatnagar, D. Kanjilal, Effect of swift heavy ion irradiation on structure, optical, and gas sensing properties of SnO2 thin films, Nucl. Instruments Methods Phys. Res. Sect. B Beam Interact. with Mater. Atoms. 266 (2008) 1987–1992. doi:10.1016/j.nimb.2008.02.062.

[19]   R.R. Krishnan, K.M. Nissamudeen, K.G. Gopchandran, V.P.M. Pillai, V. Ganesan, Effect of doping and substrate temperature on the structural and optical properties of reactive pulsed laser ablated tin oxide doped tantalum oxide thin films, Vacuum. 84 (2010) 1204–1211. doi:10.1016/j.vacuum.2009.10.026.

[20]   A. Berthelot, F. Gourbilleau, C. Dufour, B. Domenges, E. Paumier, Irradiation of a tin oxide nanometric powder with swift heavy ions, Nucl. Instruments Methods Phys. Res. Sect. B Beam Interact. with Mater. Atoms. 167-167 (2000) 927–932.

[21]   A.M. Mazzone, V. Morandi, Defects in nanocrystalline SnO2 studied by Tight Binding, Eur. Phys. J. B. 42 (2004) 435–440. doi:10.1140/epjb/e2004-00401-9.

[22]   T.L. Cottrell, The Strengths of Chemical Bonds, 2nd Ed., Butterworth, London, 1966.

[23]   A.A. Bolzan, C. Fong, B.J. Kennedy, C.J. Howard, Structural Studies of Rutile-Type Metal Dioxides, Acta Crystallogr. Sect. B Struct. Sci. 53 (1997) 373–380. doi:10.1107/S0108768197001468.

[24]   D.R. Lide, CRC Handbook of Chemistry & Physics (18th Ed.), (2004).

[25]   R. Magruder, D. Kinser, R. Weeks, Effect of Gamma Radiation on the Direct-Current Resistivity of GeO2, Commun. Am. Ceram. Soc. (1983) 1–2.

[26]   D.M. Christie, J.R. Chelikowsky, Electronic and structural properties of germania polymorphs, Phys. Rev. B - Condens. Matter Mater. Phys. 62 (2000) 14703–14711. doi:10.1103/PhysRevB.62.14703.

[27]   D. Risold, J.-I. Nagata, R.O. Suzuki, Thermodynamic description of the Pb-O system, J. Phase Equilibria. 19 (1998) 213–233. doi:10.1361/105497198770342238.

[28]   N. Boubata, A. Roula, I. Moussaoui, Thermodynamic and relative approach to compute glass-forming ability of oxides, Bull. Mater. Sci. 36 (2013) 457–460. doi:10.1007/s12034-013-0494-8.

[29]   M. Lenglet, Iono-Covalent Character of the Metal–Oxygen Bonds in Oxides: A Comparison of Experimental and Theoretical Data, Act. Passiv. Electron. Components. 27 (2004) 1–60. doi:10.1080/0882751031000116142.

[30]   I.E. Grey, W.G. Mumme, R.S. Roth, The crystal chemistry of L-Ta2O5 and related structures, J. Solid State Chem. 178 (2005) 3308–3314. doi:10.1016/j.jssc.2005.08.011.

[31]   J. Robertson, Electronic structure of SnO2, GeO2, PbO2, TeO2 and MgF2, J. Phys. C Solid State Phys. 12 (1979) 4767 – 4776. doi:10.1088/0022-3719/12/22/018.

[32]   S. Cahen, N. David, J.M. Fiorani, a. Maître, M. Vilasi, Thermodynamic modelling of the O–Sn system, Thermochim. Acta. 403 (2003) 275–285. doi:10.1016/S0040-6031(03)00059-5.

[33]   C. Catlow, A. Stoneham, Ionicity in Solids, Solid State Phys. (1983) 4321–4338. doi:10.1088/0022-3719/16/22/010.

[34]   M. a Mäki-Jaskari, T.T. Rantala, Possible structures of nonstoichiometric tin oxide: the composition Sn2O3, Model. Simul. Mater. Sci. Eng. 12 (2004) 33–41. doi:10.1088/0965-0393/12/1/004.

[35]   G. Blasse, Qualitative approach to the structural differences between some mixed metal oxides containing Sb5+, Nb5+ and Ta5+, J. Inorg. Nucl. Chem. 26 (1964) 1191–1199. doi:10.1016/0022-1902(64)80199-8.

[36]   T. Tsuchiya, H. Imai, S. Miyoshi, P.-A. Glans, J. Guo, S. Yamaguchi, X-ray absorption, photoemission spectroscopy, and Raman scattering analysis of amorphous tantalum oxide with a large extent of oxygen nonstoichiometry., Phys. Chem. Chem. Phys. 13 (2011) 17013–8. doi:10.1039/c1cp21310e.

[37]   a. Benyagoub, Phase transformations in oxides induced by swift heavy ions, Nucl. Instruments Methods Phys. Res. Sect. B Beam Interact. with Mater. Atoms. 245 (2006) 225–230. doi:10.1016/j.nimb.2005.11.106.

[38]   M. Toulemonde, F. Studer, Nanometric Amorphization of Oxide Materials under Dense Electronic Excitation: Swift Heavy Ion Irradiations, Key Eng. Mater. 155-156 (1998) 267–300. doi:10.4028/www.scientific.net/KEM.155-156.267.

[39]   H.M. Naguib, R. Kelly, A BOND-TYPE CRITERION TO PREDICT BOMBARDMENT-INDUCED, Radiat. Eff. (1975) 321–336.

[40]   Y. Murti, G. Popson, A. Laskar, Correlation of Melting Temperature and Formation Enthalpy of Schottky Defects in Ionic Solids, Phys. Stat. Sol. 133 (1990) 133–138.

[41]   R.K. Eby, R.C. Ewing, R.C. Birtcher, The amorphization of complex silicates by ion-beam irradiation, J. Mater. Res. 7 (1992) 3080–3102. doi:10.1557/JMR.1992.3080.

[42]   K. Schwartz, C. Trautmann, R. Neumann, Electronic excitations and heavy-ion-induced processes in ionic crystals, Nucl. Instruments Methods Phys. Res. Sect. B Beam Interact. with Mater. Atoms. 209 (2003) 73–84. doi:10.1016/S0168-583X(02)02013-X.

[43]   J.B. Varley, a. Janotti, C. Franchini, C.G. Van De Walle, Role of self-trapping in luminescence and p-type conductivity of wide-band-gap oxides, Phys. Rev. B - Condens. Matter Mater. Phys. 85 (2012) 2–5. doi:10.1103/PhysRevB.85.081109.

[44]   R. Liu, Y. Chen, F. Wang, L. Cao, A. Pan, G. Yang, et al., Stimulated emission from trapped excitons in SnO2 nanowires, Phys. E Low-Dimensional Syst. Nanostructures. 39 (2007) 223–229. doi:10.1016/j.physe.2007.04.009.

[45]   A.N. Trukhin, LUMINESCENCE OF A SELF-TRAPPED EXCITON IN GeO2 CRYSTAL, Solid State Commun. 85 (1993) 723–728.

[46]   S. Mochizuki, F. Fujishiro, The photoluminescence properties and reversible photoinduced spectral change of CeO2 bulk, film and nanocrystals, Phys. Status Solidi Basic Res. 246 (2009) 2320–2328. doi:10.1002/pssb.200844419.

[47]   B.R. Namozov, M.E. Fominich, R.I. Zakharchenya, Structure of the self-trapped exciton luminescence in a-Al2O3, Phys. Solid State. 40 (1998) 8–9.

[48]   M. Kirm, J. Aarik, M. Jürgens, I. Sildos, Thin films of HfO 2 and ZrO 2 as potential scintillators, Nucl. Instruments Methods Phys. Res. Sect. A Accel. Spectrometers, Detect. Assoc. Equip. 537 (2005) 251–255. doi:10.1016/j.nima.2004.08.020.

[49]   M. Watanabe, T. Hayashi, Time-resolved study of self-trapped exciton luminescence in anatase TiO2 under two-photon excitation, J. Lumin. 112 (2005) 88–91. doi:10.1016/j.jlumin.2004.09.001.

[50]   K. Schwartz, G. Wirth, C. Trautmann, T. Steckenreiter, Ion-induced formation of colloids in LiF at 15 K, Phys. Rev. B. 56 (1997) 10711–10714. doi:10.1103/PhysRevB.56.10711.

[51]   J. Jensen, a Dunlop, S. Della-Negra, Microscopic observations of metallic inclusions generated along the path of MeV clusters in CaF2, Nucl. Instruments Methods Phys. Res. Sect. B Beam Interact. with Mater. Atoms. 146 (1998) 399–404. doi:10.1016/S0168-583X(98)00515-1.

[52]   N. Itoh, D.M. Duffy, S. Khakshouri, a M. Stoneham, Making tracks: electronic excitation roles in forming swift heavy ion tracks., J. Phys. Condens. Matter. 21 (2009) 474205. doi:10.1088/0953-8984/21/47/474205.

Chapter 6

Conclusions

The effects of high energy heavy ion irradiation on SnO_2 and PbO_2 were investigated experimentally in order to complete the body of data for the Group 14 dioxide system, and to conduct a systematic study of the radiation responses of these materials for the first time. A material with significantly different crystalline structure and properties, Ta_2O_5, was also investigated for comparative purposes. All materials were subjected to the same irradiation conditions. Cation reduction and evidence for the loss of oxygen were observed in both SnO_2 and PbO_2. Tetragonal SnO formed in irradiated SnO_2, up to a concentration of approximately 23% of the sample volume at a fluence of 2.4×10^{13} ions/cm^2. Six distinct crystalline structures formed in irradiated PbO_2: Pb_2O_3 (monoclinic), Pb_3O_4 (orthorhombic), Pb_3O_4 (tetragonal), PbO (tetragonal), PbO (orthorhombic), Pb (cubic), as well as an amorphous phase of unknown composition. PbO (tetragonal) became the dominant phase at high fluences. Ta_2O_5 became fully amorphous under irradiation to a fluence of 3.0×10^{12} ions/cm^2. A loss of oxygen was evidenced during further irradiation of the amorphous material, leading to an estimated final stoichiometry of $Ta_2O_{4.2}$ at a fluence of 1.0×10^{13} ions/cm^2. In all materials investigated, evidence was given for the loss of oxygen during irradiation, as well as cation reduction in SnO_2 and PbO_2.

This study of the Group 14 dioxides has led to the following observations of the relation between materials properties and their effect on radiation response to swift heavy ion irradiation. Increased susceptibility to amorphization has been attributed to high enthalpy of formation, bandgap, electrical resistivity, and cation electronegativity (relative to those resistant to amorphization), as well as relatively low bond ionicity and bond lengths. The susceptibility of these materials to amorphization may also be related to their relatively high complexity of crystal structure, and their propensity to accommodate substitutional disorder, relative to highly ionic materials. The quantity of oxygen loss and cation reduction in the Group

123

14 dioxides appears to gradually increase down the column of the periodic table (being apparently nonexistent in SiO_2, and highest in PbO_2). Increased susceptibility to oxygen loss during irradiation has been attributed to relatively low bond dissociation energy, bandgap, and electrical resistivity, as well as relatively large bond lengths. Increased susceptibility to cation reduction also tends to increase down the column, and has been attributed to relatively high bond ionicity as well as low enthalpy of formation, melting temperature, resistivity, and cation electronegativity. The order of susceptibility to chemical effects (O-loss and cation reduction) under irradiation is, in increasing order: SiO_2, Ta_2O_5, GeO_2, SnO_2, and PbO_2. SnO_2 and PbO_2 are inherently substoichiometric and have relatively high anion conductivities. All of the aforementioned properties are related to relatively weak M-O bonds which promote the loss of oxygen during irradiation. The existence of stable lower oxides likely supports the crystallization of these phases over amorphization in SnO_2 and PbO_2.

An ion-induced damage mechanism has become evident, which leads to preferential disorder on the oxygen sublattice during SHI irradiation (namely O vacancies), and is particularly significant in the radiation response of SnO_2 and PbO_2. This same (or similar) mechanism has been observed in other oxides (CeO_2 [1–4], Al_2O_3 [5], ZrO_2 [6], UO_3 [4]) and likely controls the radiation response of these materials. A process of anion ejection from track cores have been suggested to occur in the alkali halides [7,8], and is likely related to the O loss and cation reduction presented here. Obtaining an understanding of this mechanism will allow the development of a more complete theoretical model that may succeed in describing radiation effects in a wide range of materials. This may be obtained with further investigation of the materials susceptible to these effects to determine specific materials properties relations. Future work will investigate the disordered oxygen sublattice using the combination of neutron diffraction and TEM, as well as other oxide systems to systematically determine the controlling materials properties for particular radiation responses. This is critical to the use of ion irradiation for nano-scale modification of materials and can guide the strategy for selecting materials for specific technological applications in the future.

References

[1]   H. Ohno, a. Iwase, D. Matsumura, Y. Nishihata, J. Mizuki, N. Ishikawa, et al., Study on effects of swift heavy ion irradiation in cerium dioxide using synchrotron radiation X-ray absorption spectroscopy, Nucl. Instruments Methods Phys. Res. Sect. B Beam Interact. with Mater. Atoms. 266 (2008) 3013–3017. doi:10.1016/j.nimb.2008.03.155.

[2]   A. Iwase, H. Ohno, N. Ishikawa, Y. Baba, N. Hirao, T. Sonoda, et al., Study on the behavior of oxygen atoms in swift heavy ion irradiated CeO2 by means of synchrotron radiation X-ray photoelectron spectroscopy, Nucl. Instruments Methods Phys. Res. Sect. B Beam Interact. with Mater. Atoms. 267 (2009) 969–972. doi:10.1016/j.nimb.2009.02.035.

[3]   S. Takaki, K. Yasuda, T. Yamamoto, S. Matsumura, N. Ishikawa, Atomic structure of ion tracks in Ceria, Nucl. Instruments Methods Phys. Res. Sect. B Beam Interact. with Mater. Atoms. 326 (2014) 140–144. doi:10.1016/j.nimb.2013.10.077.

[4]   C.L. Tracy, M. Lang, J.M. Pray, F. Zhang, D. Popov, C. Park, et al., Redox response of actinide materials to highly ionizing radiation, Nat. Commun. 6 (2015) 6133. doi:10.1038/ncomms7133.

[5]   A. Kabir, A. Meftah, J.P. Stoquert, M. Toulemonde, I. Monnet, M. Izerrouken, Structural disorder in sapphire induced by 90.3 MeV xenon ions, Nucl. Instruments Methods Phys. Res. Sect. B Beam Interact. with Mater. Atoms. 268 (2010) 3195–3198. doi:10.1016/j.nimb.2010.05.087.

[6]   J.-M. Costantini, F. Beuneu, D. Gourier, C. Trautmann, G. Calas, M. Toulemonde, Colour centre production in yttria-stabilized zirconia by swift charged particle irradiations, J. Phys. Condens. Matter. 16 (2004) 3957–3971. doi:10.1088/0953-8984/16/23/014.

[7]   J. Jensen, a Dunlop, S. Della-Negra, Microscopic observations of metallic inclusions generated along the path of MeV clusters in CaF2, Nucl. Instruments Methods Phys. Res. Sect. B Beam Interact. with Mater. Atoms. 146 (1998) 399–404. doi:10.1016/S0168-583X(98)00515-1.

[8]   K. Schwartz, G. Wirth, C. Trautmann, T. Steckenreiter, Ion-induced formation of colloids in LiF at 15 K, Phys. Rev. B. 56 (1997) 10711–10714. doi:10.1103/PhysRevB.56.10711.